HIGH FREQUENCY GROUND MOTION IN CENTRAL MÉXICO: SITE, EXCITATION AND ATTENUATION

Roberto Ortega, B. S., M. S.

**A Digest Submitted to the Faculty of the Graduate School
of Saint Louis University in Partial Fulfillment of
the Requirements for the Degree of
Doctor of Philosophy**

2000

Digest

A regional study of ground motion scaling parameters is presented for the region surrounding the Valley of México. Of particular importance to the seismic hazard in this region are intermediate-depth earthquakes, not only because of some highly energetic events, but also because of the proximity to the cities and villages in the Mexican Altiplano. We examined 227 regional earthquakes and mining events ranging in depth from the surface to 100 km and in magnitude from 3 to 7. We also studied several intermediate-depth (100-300 km) events, including the major event of June 15, 1999. From these observations we estimated empirical attenuation relations and an average Q for frequencies between 0.7 and 7 Hz. A simple regression model to separate the source, site, and propagation terms is applied using: $Y = log(A\,(R, f)) = Src\,(f) + Site\,(f) + D\,(R, f)$. Our primary objective is to estimate the propagation term $D(R,f)$ which includes the effects of anelastic and scattering attenuation as well as geometrical spreading. An analysis is done in both the frequency and time domains.

Our data were generated by small earthquakes, mining explosions and volcanic activity especially from the Popocatépetl volcano. The estimated excitation shape for the mining events clearly show different populations that distinguish earthquakes from volcanic and mining activity. We parameterized the observations to be able to use random vibration theory to predict peak motion.

A coda normalization technique used for an initial estimate of the propagation term, did not fit the regression results well. I measured the average

attenuation of S and Lg waves and found that a $Q(f) = 220\,f^{0.66}$ described the attenuation and a geometrical spreading as r^{-1} for $r \leq 180\ km$ and as $r^{-0.5}$ for $r \geq 180\ km$. The results indicate that this region is characterized by a rapid decay of amplitude with distance similar to those in other tectonically active regions.

HIGH FREQUENCY GROUND MOTION IN CENTRAL MÉXICO: SITE, EXCITATION AND ATTENUATION

Roberto Ortega, B. S., M. S.

**A Dissertation Submitted to the Faculty of the Graduate School
of Saint Louis University in Partial Fulfillment of
the Requirements for the Degree of
Doctor of Philosophy**

2000

Acknowledgments

I dedicate this thesis to the Indian community of central México, especially to the Nahuas in San Mateo Ozolco Puebla, they had to struggle through the devastating earthquake on June 15th, 1999.

Thanks to my parents, they are an example to follow in life.

Dr. Robert B. Herrmann has been an excellent guide all the time, he has taught me the importance of a high quality work. His advice, friendship and help is really appreciated. Dr. Charles J. Ammon deserves special recognition, he has been an exceptional guide during my stay in Saint Louis University, because of his invaluable friendship and his inspirational example for scientific discovery. Dr. Brian Mitchell thoroughly reviewed the thesis and provided inciteful comments.

Dr. Luis Quintanar has been a constant help with the Red Sísmica del Valle de México (RSVM) network, and Dr. Javier Pacheco provided the Broad Band (BB) data. Jesus Perez Santana maintained the BB database and Jose Luis Cruz answered all the questions about the instrument calibration of the RSVM.

Thanks to my friend Dr. Luca Malagnini for his outstanding support.

My friends in St. Louis University. And my dear friends of the technical staff, Melanie Whittington and Sean Thomas Morrisey.

Finally thanks to my brothers, for encouraging me.

Table of Contents

List of Tables

List of Figures

1. Introduction

1.1 Objective

Knowledge of high frequency earthquake ground motion is essential for the assessment of seismic hazard. The objective of this study is the quantitative description of regional attenuation of potentially damaging seismic waves in central México. This region of the world is strongly affected by earthquakes. The most common and threatening earthquakes to central México are located along the west coast of México, and are related to the eastward subduction of the Rivera and Cocos plates. However local and regional earthquakes may also cause severe damage to the cities and villages in the Mexican Altiplano. The focus of this work is the study of ground motions caused by these local and regional inland earthquakes.

An expression or algorithm used to estimate the expected ground motion parameters as a function of distance and magnitude is called a predictive relationship. The general problem can be stated as follows: What is the expected peak acceleration at any location given an earthquake at a specific location and magnitude? Predictive relationships are usually developed by regression of strong motion records (eg. Atkinson and Boore, 1995; Boore and Joyner, 1991). In low-seismicity regions such as the central United States, strong ground motion data are sparse and the regional and local seismic networks recordings are used to augment the data set (Sameizadé-Yazd et al., 1997). This is important because many intraplate regions in the world have a much lower rate of earthquake activity compared to those at the plate boundaries, and thus there are insufficient num-

bers of strong motion recordings to define ground motion scaling relations.

Many functional forms of the predictive relationships have been developed, which reflect variations of earth structure and earthquakes. The actual parameterization of the ground motion is a model that reflects the physical properties of the source, propagation and site response. Perhaps the simplest model, and the one used in this work, is a model where the maximum amplitude observed at a certain frequency can be described by separate source, site and propagation terms.

Once a predictive relationship is estimated, the accuracy of the results is examined. This is clearly a very important part of this research since the immediate application is for seismic hazard assessment. The non-uniqueness of the functional form to describe the attenuation of the seismic waves requires special attention. For example, different numerical values for the quality factor and geometrical spreading may express similar propagation effects. For this reason caution is required when the results from different regions are interpreted.

I begin in Chapter 1, with an outline of the geological and tectonic setting. The geology of this region is fascinating because of the dramatic tectonic changes during the last 50 million years. The quantification of the regional ground motion parameters is described in Chapter 2, especially the methodology for estimating the regional attenuation of the earthquake induced ground motions. Chapter 3 contains illustrations of the data analysis procedures, including the general data regression and the forward modeling. The next chapter is dedicated to interpretation of the excitation term in terms of spectral scaling relations, event type discrimination,

and source models. I conclude with a comparison of results for several regions, including the central United States, Italy and Germany, a general discussion and recommendations for future research.

1.2 Central México Tectonic Setting and Seismicity

Central México is a tectonically active region in which the main tectonic feature is the TransMexican Volcanic Belt (TMVB), a 20-70 km broad structure which extends from Jalisco on the Pacific coast to Veracruz on the Gulf of México. In addition to the low-magnitude but nearly continuous seismicity related to the TMVB, intermediate-depth earthquakes with normal fault motion on or within the subducted Cocos plate are important sources of damaging shaking that affect the cities and villages in central México (Singh et al. 1999). The TMVB has geological characteristics that are associated with a highly attenuating region, e.g., a highly fractured zone, high volcanic activity, and high heat flow (Ziagos et al., 1985). The orientation of the volcanic arc is oblique to the Middle American Trench, which is apparently due to the shallow dip of the Rivera and Cocos plates subducting beneath the North American plate (Pardo and Suarez, 1995).

The seismic activity in the TMVB is usually low, but large events do occur. Local earthquakes originate on faults aligned parallel to the TMVB (Lermo et al., 1997). The largest earthquake in the TMVB occurred on November 12, 1912 (Ms=6.9) and was located 100 km northwest of México City in the Acambay Graben (Fig. 1.1). The 1912 earthquake originated on the south bounding fault of the Acambay Graben called the Acambay-Tixnadejé fault. This fault has been studied by several authors (Urbina

and Camacho, 1913; Astiz, 1980; Castro et al., 1983; Yamamoto and Mota, 1991). The 1912 event caused vertical displacements up to 50 cm along the faults flanking the Acambay graben, where a maximum magnitude of M $\geq$ 7.5 is expected (Suter et al. 1992). The central part of the TMVB is characterized by pronounced W-E striking fault scarps (Johnson and Harrison, 1989). But little is known about the detailed structural geometry of these faults. A more recent event occurred on February 22, 1979 (mb=5.3) on the Venta de Bravo Fault (Astiz, 1980). The focal mechanism of the main shock, determined by Astiz (1980), includes a normal fault oriented W-E with a dip of 60^oN at a depth of 8.5 km. The directions and relative magnitudes of the principal stresses of the present-day have been estimated from volcanic alignments, focal mechanisms and inversion of slip vectors from striations on the main faults. The maximum horizontal stress directions inferred are generally west-east (Suter et al. 1992).

An interesting feature of the seismicity in central México is the presence of seismic swarms. Some examples are the swarm of February 1984 consisting of 39 events with depths less than 17 km (Rodríguez et al., 1984) in the state of México, the swarm in the Toluca Valley on August 1980 consisting of 29 recorded events (Yamamoto and Mota, 1988) with depths between 3 and 25 km, and 23 earthquakes that occurred during June 1988 in the basin of Apan in the Hidalgo state with a maximum depth of 8 km (Campos et al. 1994). All these earthquakes had magnitudes less than 3.5.

Most earthquake swarms occur in volcanic regions (Klein et al., 1987) and their occurrence has often been related to the movement of magma. Some examples of earthquake swarms around the world are those beneath the Kilawea caldera on the island of Hawaii, where earthquakes occur at
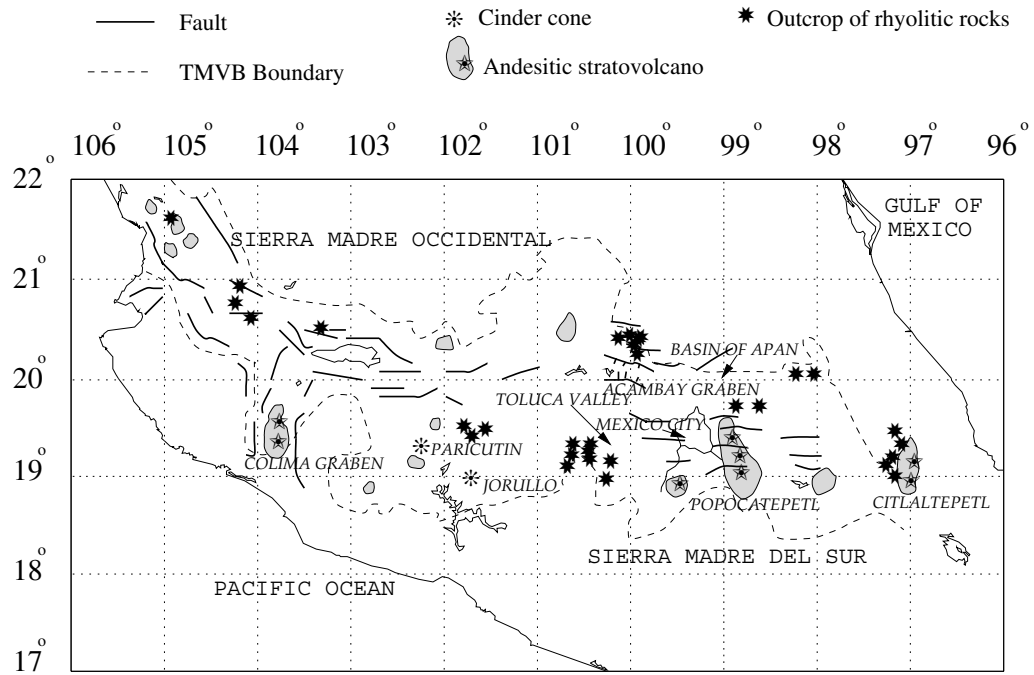
Figure 1.1: Main geological features of the TMVB. The main andesitic and silicic volcanic centers are indicated.

a relatively constant rate between 40 and 12 km (e.g. Lay and Wallace, 1995). A more atypical two-year swarm occurred in the Gilbert Islands in the southwest Pacific, with predominantly thrust focal mechanisms (Lay and Okal, 1983).

The basin surrounding México City was formed during the Middle Tertiary. Two Pliocene fluvial systems were closed by extensive Quaternary volcanism, and the lacustrine basin of México was formed. México City is located within this lacustrine basin usually called "the Valley of México".

Since 1994, the "Red sísmica del valle de México" (RSVM, seismic network of the Valley of México) has detected earthquakes originating within and around the Valley of México. These small earthquakes usually do not trigger the national seismic network. Figure 1.2 shows the epicenters of the local events that occurred during the period of January 1996 to November
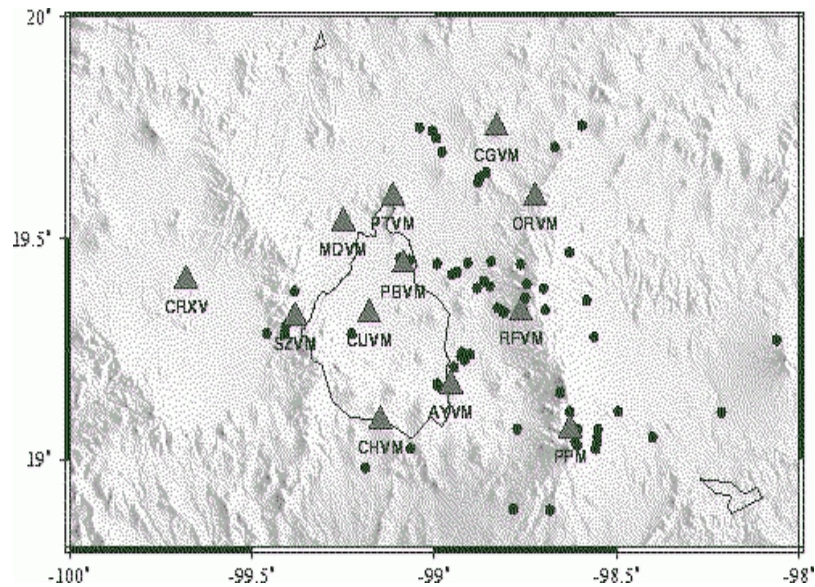
Figure 1.2: Local events recorded by the RSVM during the period of January 1996 to November 1997, the main activity is located in the eastern part of the México Valley. Triangles represent the seismic stations. The México City boundary (solid line) is indicated over the background topography.

1997. The seismic activity is located mainly on a band oriented N-S in the eastern part of the Valley. There is also some activity in the "las Cruces" Sierra in the eastern part of México City (near stations RFVM and PPM). All the seismic activity within and around the Valley of México is related to a fault system connected to a major system on the TMVB.

1.3 Geological Setting of the Basin of México

The Valley of México is located in the central portion of the TMVB. The site has a long history, the ancient city of Tenochtitlán (now México City) was founded by the Aztecs in 1325 on an island in a lake confined by Sierras (see Figure 1.1). Today the region is home to 21 million people, much of the population of México.

The oldest rocks in the region are anhydrites and limestones of lower Cretaceous age and these are overlain by a sequence of limestones, marls and sandstones of upper Cretaceous age (Vazques and Jaimes, 1989). Outcrops in the south between the cities of Cuernavaca and Cuautla at 1500 m above sea level consist of limestones and sandstones (Mooser, 1961). Cretaceous strata are folded and have a maximum thickness of 1700 m and are unconformably covered by Eocene to Oligocene red continental clastic deposits interbedded with basaltic flows and rhyolitic breccias. These red beds have a thickness of about 600 m (Suter et al. 1992). Overlying this sedimentary base are volcanic rocks of the Sierra Madre Occidental cordilleran province (Oligocene to Miocene in age).

The Oligocene volcanics include lava flows, pyroclastics, and breccias of andesitic to dacitic nature with a thickness ranging between 100 and 4000 m. Above these the Miocene volcanic rocks consist of rhyolites, dacites, andecites and basalts which are overlain by the basal sequence of the TMVB (Plio-Quaternary). At the base of the Pliocene sequence there are andesitic to dacitic lava flows, volcanic breccias and pyroclastics. Above those are pyroclastic and clastic alluvial sequences deposited in structural depressions. The Pliocene and Quaternary strata can attain a thickness of about 700 m.

Most of the Quaternary volcanism is of a monogenetic nature and includes numerous cinder cones, domes and associated lava flows (Ferrari et al. 1994). The Popocatépetl and Iztaccihuátl volcanoes belong to this andesitic - dacitic volcanic phase. The southward basin drainage was interrupted during the Quaternary by the volcanic products of the Sierra Chichinautzin, generating the lake systems within the México Valley, lo-

cally interbedded with contemporaneous volcanic products (see Figure 1.1).

1.4   Ground Motion Parameters

A regional study of earthquake ground motion scaling relationships is essential for the design of requirements for the construction of earthquake-resistant structures and facilities. The estimation of expected ground motion parameters like peak amplitudes and signal duration as function of source-receiver distance and event magnitude is the main objective of this dissertation. The ground motion is modeled as the separable effects of source, site and propagation. Before quantitatively exploring the mathematical model in the next chapter, I would like to conclude this introduction with a qualitative review of the factors affecting the observed ground motion spectrum. The logarithm of the ground motion spectrum can be represented as a sum of excitation, propagation and site terms

$$Ground\ motion = Excitation + Propagtion + Site$$

Strictly speaking, the site term is also a propagation effect, but is traditionally separated from the regional propagation factor.

The source term is better parameterized at a reference distance to avoid problems of extrapolation from zero distance where there are generally few if any observations. Traditionally a common constraint on the propagation term is that it is referenced to a distance of $r = 1$ kilometer which implies that the source term is always extrapolated from the observations.

The site term includes the propagation through the uppermost hundred meters of rock and soil and the effect of the surface topography near

the recording site. In central México a common amplification for all the stations is expected within the Basin of México, which consist of thick sedimentary deposit near the surface. Thus a complete separation of terms may not be possible, for example, the excitation term may include a common site factor. The effect of shallow geology on ground motion has been understood as amplifications due to the presence of unconsolidated sediments (Idriss and Seed, 1968; Seed and Idriss, 1969; Borcherdt, 1970; Trifunac and Brady, 1976; Johnson and Silva, 1981; Bard and Bouchon, 1985; Moczo and Bard, 1993). The total effect of shallow geology on seismic waves is the combined effect of amplification through low-velocity layers, and the exponential attenuation at high frequency due to the anelastic behavior of the shallow materials. Severe dissipation of the elastic energy due to the presence of a deep unconsolidated sediments can substantially reduce the expected ground shaking, especially at low frequencies. Along the Basin of México, especially in the Valley of México, there is a considerable amplification of the seismic waves recorded in the lake-bed with respect to the hill zone (Rosenbleuth, 1988). Perhaps there is no truly hard rock site in the Valley of México (Singh et al. 1995). However in order to use stochastic models for simulating ground motions or maximum amplitudes, site amplification factors are needed for specific locations.

The propagation factor (or attenuation relationship) is the combination of geometrical spreading, anelastic attenuation and scattering of elastic waves by lateral variations along the wave's path through the Earth. Some attenuation relationships have been proposed for western and eastern North America during the past decades (Campbell, 1981; Joyner and Boore, 1981; Boore, 1983; Boore and Joyner, 1991; Atkinson and Boore,

1995; Atkinson and Silva, 1997; Campbell, 1997; Raoof et al., 1999) and some in México (Ordaz and Singh, 1992; Anderson and Lei, 1994; Ordaz and Reyes, 1999)

Earthquake damage is strongly related to ground motion duration. Short duration motions with high acceleration may not produce enough load reversal to damage buildings but those with long duration may (Kramer, 1996). Signal duration is also important because it is required to estimate the peak motions using stochastic models in the theory described by Boore (1983).

Several authors have investigated the influence of tectonic structures on duration, Q_o and propagation effects in central México. Yamamoto et al. (1997) characterized the attenuation of the Lg wave by studying its coda for different tectono-stratigraphic terranes in southern México. He found that the spatial distribution of Lg coda Q values indicates that events from Jalisco, Michoacan, and Oaxaca yield higher values of Q_o than those from Guerrero. He found a very high Lg coda Q for the TMVB as compared to other regions of southern México, concluding that the high $Q(f)$ value ($325\,f^{0.9}$) does not entirely reflect the attenuation characteristics of the TMVB but it is probably contaminated by a wave guide effect, which may also increase the duration of Lg wavetrains. Canas (1986) used the Lg coda of several earthquakes located on the TMVB to estimate Q_o, defining $Q(f) = Q_0 f^{\eta}$. He obtained a value of $Q_o = 322$ for the central part and a $Q_o = 129$ for the eastern region. Ordaz and Singh (1992) used regression of strong ground-motion data along a 300 km long path to estimate the spectral attenuation as a part of a study characterizing the amplification of seismic waves in the hill zone of the Valley of México. They

found a value of $Q(f) = 273\,f^{0.76}$. They did not find significant differences in attenuation characteristics along coastal and inland paths, and attributed the observed increase in the amplitude of seismic waves at hills sites to a relatively shallow (≤ 1 km) clay deposit. In order to characterize the attenuation laws at different frequencies, Ordaz and Reyes (1999) described predictive relationships for estimating the acceleration response spectrum of a linear single degree of freedom oscillator, at the station CU, which is located at a hill site in the Universidad Nacional Autónoma de México, Ciudad Universitaria campus. Recently Singh et. al (1999) studied an intermediate-depth earthquake on June 15, 1999 ($M_w = 7.0$) and reported on characteristics of the source and propagation. The earthquake was particularly destructive to historical monuments, but produced lower accelerations than similar earthquakes in the same region.

In order to estimate the predictive relations I process the data set in both the Fourier velocity spectra and time domain peak filtered velocity domains. I use both domains to check consistency in the data. I characterize ground motions in a manner consistent with random vibration theory RVT, a tool used to predict the peak amplitudes when the time series are not required, using signal duration and amplitude spectra at the site (Boore, 1983).

2. Method

2.1 Introduction

In this chapter I discuss the methodology to quantify the regional attenuation of the earthquake ground motion.

Ground motions depend on the mechanical properties of the earth materials and the heterogeneities found along their path. In general the logarithm of the maximum amplitude can be separated as the effect of source, site, and propagation path (e.g. Raoof et al., 1999; Malagnini et al., 2000a,b)

$$Y = log\,(Amp) = Src\,(f) + Site\,(f) + D\,(R, f) \tag{2.1}$$

where f represents frequency and R hypocentral distance. Defining the maximum amplitude as the ground motion parameter modeled and emphasizing the fact that the observed motions are referred to the level at a specific reference distance rather than the source, we can rewrite equation 2.1 as

$$Y = log\,(Amp) = E\,(f) + Site\,(f) + D\,(R, f) \tag{2.2}$$

where $E(f)$ is the excitation term at a reference distance. The excitation term is equal to the source term when the reference distance is equal to zero.

The propagation (or distance) term $D(R,f)$ contains the contributions from the geometrical spreading and anelastic and scattering attenuation

$$D\,(R, f) = log\left[g(r)\,exp\left(-\frac{\pi f R}{Q(f)\beta}\right)\right] \tag{2.3}$$

where $g(r)$ is the geometrical spreading function, R is the hypocentral distance, $Q(f)$ is the attenuation function and β the shear wave velocity. In-

12

stead of working directly with this expression in the regression, *D(R,f)* is initially parameterized as a piecewise linear function (Anderson and Lei, 1994; Harmsen, 1997) defined at a frequency f_c as:

$$D\left(R, f_c\right) = \sum_{i=0}^{n} L_i\left(R\right) D_i \tag{2.4}$$

where $L_i\left(R\right)$ is a linear interpolation function and D_i are node values such that $D(r_i) = D_i$. This definition of the propagation term allows us to model our observations without any *a priori* assumption of the propagation parameters, especially the functional form of $g(r)$. The number of nodes, *n*, is chosen by examining the distribution of observations with distance.

2.2 Data Preprocessing

The first step in any study is the collection of seismograms. My data were obtained from two different seismic networks. The original waveforms were corrected for instrument response to yield ground velocity in m/s (See the Appendix, for the instrument calibration of the RSVM). For high-frequency studies it is convenient to preprocess the data, estimating the most important ground motion parameters and storing that information in tables. In this study preprocessing the data consisted of filtering waveforms, using filters with different center frequencies and saving the following information:

- event location and depth; the station name and a unique integer identifier of the event and the station.

- the maximum velocity of a single degree oscillator velocity spectra for 5% damping

- the maximum amplitude of the filtered velocity with corner frequencies of 0.707 f_c and 1.414 f_c

- the duration following the S arrival (5 % - 75% of the integral of filtered velocity squared)

- the Fourier velocity spectra RMS averaged over the selected frequency band 0.707 f_c and 1.414 f_c

- maximum filtered amplitude in P window

- the RVT (peak value estimated using the Random Vibration Theory) predicted peaks from 5% - 75% for the filtered displacement and the pseudo velocity spectra of a single degree oscillator for a 5% damping obtained from observed filtered spectra and duration

- the RMS average of the absolute value of the time series for a moving window using 512 points with 50% overlap of the time filtered velocity to define the coda

I only used high signal-to-noise ratio observations. A high signal-to-noise ratio is defined as the situation when the maximum amplitude is at least three times greater than the RMS value prior to the P arrival. A typical table entry looks like the Figure 2.1.

Band-pass filters are used to focus on a narrow frequency band centered on f_c. For each frequency f_c an 8 pole high-pass followed by an 8 pole low-pass Butterworth filter is applied, with corner frequencies of $\frac{1}{\sqrt{2}} f_c$ and $\sqrt{2} f_c$ where f_c equals 0.7, 0.9, 1.2, 1.7, 2.0, 3.0, 4.0, 5.0, 6.0 and 7.0 Hz. The total filter gain is adjusted to be 1.0 at the center frequency f_c. The amplitude response of the filters is shown in Figure 2.2.

```
***EVENT  AND STATION  INFORMATION  ***
9 ORVM 7
98 8 18 18 52 49.20 110
19.19 -98.99 9.00 52.60 328.51 0.00 6 3.00
***TIME DOMAIN PROCESS****
15.67 0.246E-05 0.405E+01 0.336E+01 0.219E-05 0.379E+01 0.280E-05 0.170E-05
0.584E-06
***FOURIER DOMAIN PROCESS****
15.50 0.118E-04 0.500E+01 0.339E+01 0.112E-04 0.380E+01 0.141E-04 0.882E-05
0.182E-05
0.67572893E-06  0.33731332E-11  0.83286886E-13  0.54164769E-13  -0.10000000E+01
****RMS VELOCITY  AND PSEUDO-ACCELERATI ON, PHASE PICKING****
-17.40 0.421E-07 0.156E-06 0
-14.18 0.443E-07 0.179E-06 0
-10.95 0.401E-07 0.163E-06 0
-7.73 0.359E-07 0.175E-06 0
-4.50 0.362E-07 0.172E-06 0
-1.28 0.497E-07 0.205E-06 0
1.95 0.491E-07 0.200E-06 0
5.17 0.437E-07 0.190E-06 0
8.40 0.118E-06 0.538E-06 1
11.62 0.147E-06 0.653E-06 1
14.85 0.599E-06 0.316E-05 2
18.07 0.692E-06 0.374E-05 2
21.30 0.400E-06 0.238E-05 2
24.52 0.206E-06 0.140E-05 2
27.75 0.116E-06 0.750E-06 3
30.97 0.787E-07 0.370E-06 3
34.20 0.828E-07 0.380E-06 3
37.42 0.736E-07 0.312E-06 3
40.65 0.616E-07 0.247E-06 3
43.87 0.675E-07 0.249E-06 3
47.10 0.659E-07 0.332E-06 3
50.32 0.501E-07 0.297E-06 3
53.55 0.462E-07 0.220E-06 3
```

Figure 2.1: Information stored in the preprocessing stage. Event and station information: (First row) Station identifier, station name, filter number. (Second row) Event date and event ID. (Third row) Event latitude and longitude, depth, hypocentral distance, azimuth, magnitude, filt id, and frequency fc. Time domain process: (Fourth row) Time of max. filtered amp, max amplitude, duration, velocity for max amplitude, RVT peak for filt. vel, frequency of zero crossing of filtered data, estimated 95 upper and lower bound of filtered data, max. amplitude in P window. Fourier Process: (Fifth row) Time of max PSRV, pseudo-velocity spectra, duration of oscillator displacement squared, vel. for max PSRV, RVT peak for PSRV, freq of zero crossing for PSRV, estimated 95 upper and lower bound of PSRV, max PSRV in P window. Fourier amplitude spectra: (Sixth row) RMS average, energy in time band1, energy band2, energy band3, energy band4. (Following rows) RMS Velocity for a time window 256 samples: Time reference, RMS velocity, PSVA, Phase picking: 0 before P, 1 between P and S, 2 after S, 3 after 2 S.

Butterworth Bandpass Filters
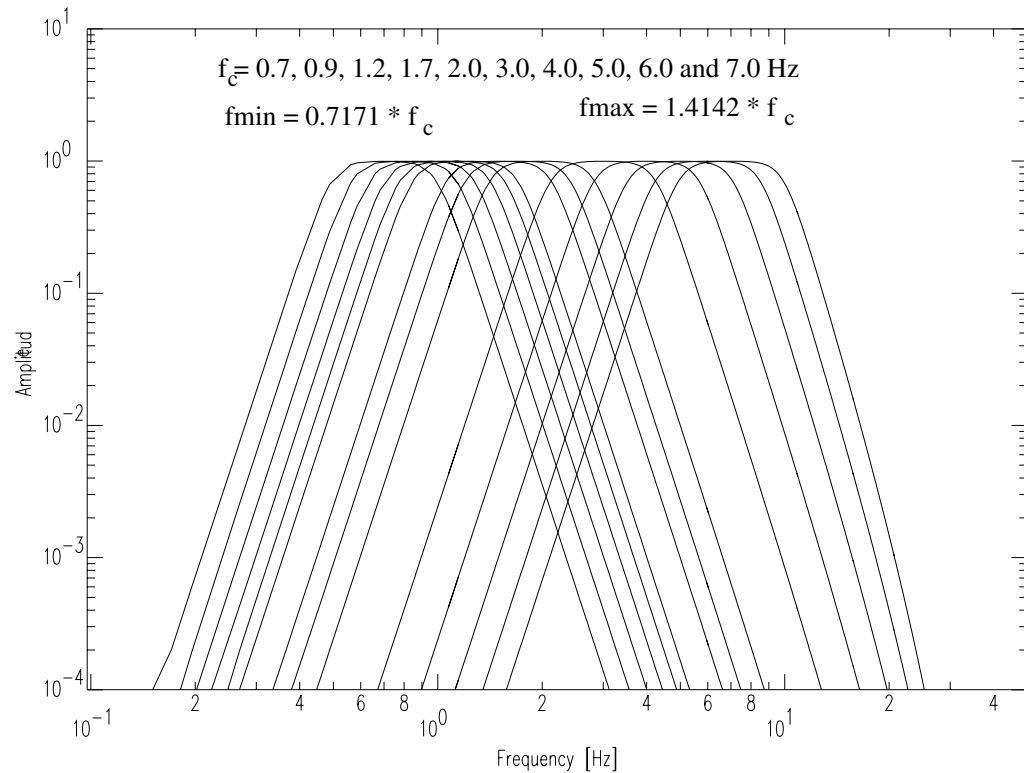
Figure 2.2: Amplitude Spectrum for the band-pass filters. For each frequency *fc* an 8 pole high-pass followed by an 8 pole low-pass Butterworth filter is applied with corner frequencies of 0.707 fc and 1.414 fc. Note that these filters are actually quite broad.

After each waveform is band-pass filtered the duration is estimated. Figure 2.3 illustrates the process used to compute the duration. Starting from the S arrival the filtered velocity is squared and integrated. The integrated energy is normalized to a unit maximum value and the time window that contains between 5% and 75% of the integrated energy is estimated. This time duration will be used later to predict the peak values of the time series from the RMS average using random vibration theory. The average Fourier amplitude spectrum is computed between $f_c/\sqrt{2}$ and $\sqrt{2}f_c$ in the 5% - 75% energy window and the two values (maximum filtered time series amplitude and the Fourier amplitude spectra RMS average over the frequency band) are stored for further analysis in each domain.

For each frequency f_c the logarithm of the maximum amplitude (time series or Fourier amplitude spectrum) is related to the excitation, site and attenuation parameters by combining equations 2.2 and 2.4

$$Y = E + Site + \sum_{i=0}^{n} L_i(R)D_i \tag{2.5}$$

where n is the number of nodes in the distance function and $D(R)$ is the distance of their measurement for each distance.

All measurements for a particular frequency are combined into a single matrix equation relating the observations with the excitation, site and distance attenuation function. These equations can be solved in a least-square sense used a damped regression. To further stabilize the solution, three additional constraints are applied

1) $D(r)$ is forced to be zero at a reference distance

$$D(R = r_{ref}) = 0, \tag{2.6}$$
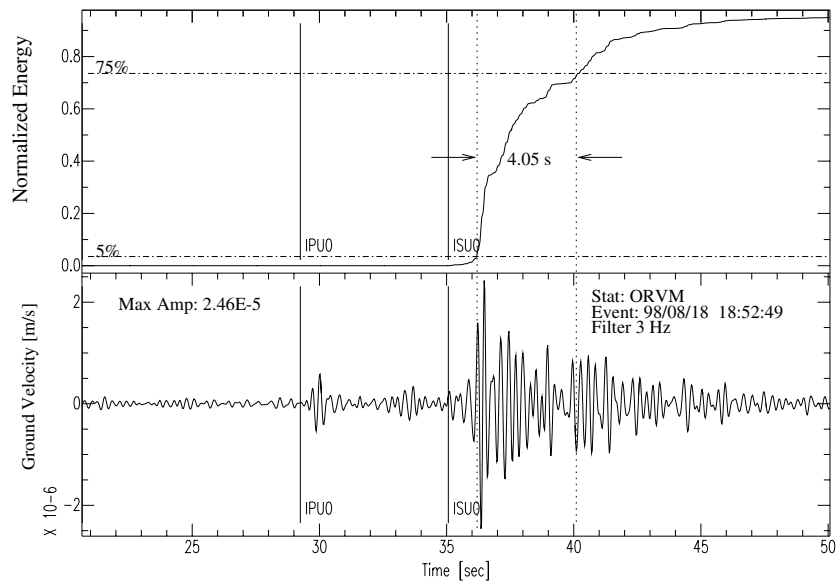
Figure 2.3: Procedure for estimating duration. The example shown in this plot was recorded on August 8, 1998. The waveform is at the central frequency of 3 Hz (See text for details). The squared velocity after the S arrival is integrated and normalized to the unit value. The times for the 5% and 75% are computed and this time window (4.05 s) is defined as the duration at the frequency of 3 Hz. The P and S arrivals are picked manually.

2a) The summation of all site terms at a particular frequency is equal to zero

$$\sum_{i=0}^{nsites} Site_i(f) = 0, \tag{2.7}$$

2b) The site term at a reference site is equal to zero

$$Site_{reference}(f) = 0 \tag{2.8}$$

3) The roughness of the attenuation function is minimized

$$Roughness = \sum_{i=1}^{n} D_{i-1} - 2D_i + D_{i+1}. \tag{2.9}$$

2.3   Coda Normalization

An initial estimate of the propagation term *D(r)* is computed using a coda normalization (Aki, 1980; Frankel et al., 1990; Fehler et al., 1986; Mayeda et al., 1992). Coda is the term used to describe the part of the seismogram between identifiable waves. In this study the coda is the part of the seismograms that follows the S or Lg waves and is composed of waves scattered in the crust and upper mantle. This part of the record has been used to infer source, path and site effects (Aki, 1969; Aki and Chouet, 1975). Some characteristics of the coda are:

- the coda level is a function of the source and local geology for each site

- the coda originate from a backscattering process, caused mainly by heterogeneities distributed in a broad region connecting the source and receiver

- the power spectra of the coda waves decays as a function of time independent of the path

These properties can be expressed in terms of the power spectrum of the coda. The time domain RMS amplitudes of narrow bandpass filtered waveforms in windows centered on a time τ and running along the seismic coda, can be represented as:

$$\log[a_c\,(f,\tau)] = SOURCE_{Coda}(f) + C(f,\tau) + SITE_{Coda}(f) \qquad (2.10)$$

where $a_c\,(f,\tau)$ is the RMS value computed in a window centered at time τ, for a filtered time history centered at a frequency f. The $SOURCE_{Coda}(f)$ and $SITE_{Coda}(f)$ terms are source and site terms related specifically to the coda, but generally are proportional to the source and site terms of the maximum amplitude. The function $C(f,\tau)$ reflects a level of excitation of the coda. The coda reduced peak amplitude at a lapse time τ_{ref} is defined as:

$$a_{reduced}(r,f) = a_s(r,f)/a_c(f,\tau_{ref}) \qquad (2.11)$$

where $a_s(r,f)$ is the peak amplitude for the filtered time history.

If source and site terms for the coda are linearly proportional to the ones for the S-waves then the ratio eliminates the source and site terms:

$$log\,[a_{reduced}(r,f)] = D(r,f) - C(f,\tau_{ref}) \qquad (2.12)$$

The choice for τ_{ref} is arbitrary. By forcing $D(r_{ref},f) = 0$ we fix the amplitude offset caused by $C(f,\tau_{ref})$. The reference distance r_{ref} is selected to be within the range of observed distances so that we interpolate within the data set rather than extrapolate beyond. The value should be far enough

from the source so that errors in source depth do not significantly affect hypocentral distance, and yet not so far that expected super-critically reflected crustal arrivals complicate the motion, thus preventing inter-regional comparisons. For these reasons we use a reference distance of $r_{ref} = 40$ km for our studies.

The coda normalization technique uses the ratio of the S or Lg wave amplitude to that of the coda wave envelope to remove the effects of source and site. Combining equation 2.4 and 2.12 the logarithm of each reduced amplitude $Y_i(r)$ at a particular frequency can be written as

$$log\left[a_{reduced}(r, f_c)\right] = L_j(r)D_j + L_{j+1}D_{j+1} - C(f_c, \tau_{ref}) \tag{2.13}$$

The contribution to two adjacent nodes is computed by linear interpolation and fixed at the desired distance nodes. Defining p as

$$p = \frac{R - ND_{j-1}}{ND_j - ND_{j-1}} \tag{2.14}$$

where R is the hypocentral distance and ND_j and ND_{j-1} are the predefined distance nodes in the interval $ND_{j-1} < R < ND_j$.

From equation 2.13 and defining $Z_i(r) = log\left[a_{reduced}(r, f_c)\right]$ we have

$$Z_{ik}(r) = pD_j + (1 - p)D_{j+1} - C_k(f, \tau_{ref}) \tag{2.15}$$

For each frequency, f_c, we obtain a linear system for the n observations, $m + 1$ constraints and m distances.

$$\mathbf{Z}_{\{n+m+1\}\times 1} = \mathbf{X}_{\{n+m+1\}\times m}\mathbf{D}_{m\times 1}$$

We add the constraint (2.6) by appending additional rows to the linear equations and these rows are weighted heavily. Effectively, this constraint

eliminates the term $C(f, \tau_{ref})$ from equation 2.15. This matrix equation is solved in the least square sense using a Singular Value Decomposition (SVD).

The resulting matrix equation is:

$$
\begin{pmatrix} Z_1 \\ Z_2 \\ \vdots \\ \vdots \\ Z_n \\ \cdots \\ 0 \\ \vdots \\ \vdots \\ \vdots \\ 0 \\ \cdots \\ 0 \end{pmatrix}
=
\left(
\begin{array}{cccccc}
0 & p & 1-p & 0 & \cdots & 0 \\
p & 1-p & 0 & 0 & \cdots & 0 \\
\vdots & \vdots & \vdots & & & \vdots \\
\vdots & \vdots & \vdots & & & \vdots \\
0 & 0 & p & 1-p & \cdots & 0 \\
\hline
-2w & w & 0 & 0 & \cdots & 0 \\
w & -2w & w & 0 & \cdots & 0 \\
\vdots & & \ddots & & & \vdots \\
\vdots & & & \ddots & & \vdots \\
\vdots & & & & \ddots & \vdots \\
0 & 0 & 0 & \cdots & w & -2w \\
\hline
0 & 0 & v & 0 & \cdots & 0
\end{array}
\right)
\times
\begin{pmatrix} D_1 \\ D_2 \\ D_3 \\ \vdots \\ \vdots \\ D_m \\ C_1 \\ C_2 \\ C_3 \\ \vdots \\ C_k \end{pmatrix}
$$

The first n rows are the linear system for observations, the smoothness constraint follow. Strictly speaking the smoothness constraint in 2.9 is only a perfect second derivative if the r_i distances are evenly spaced. Since we use an unequally spaced distance term this condition is thus a constraint in a mapped distance space for unevenly spaced distance. The last row applies the constraint 2.6, the unit amplitude (zero log) at r_{ref}.

2.4 Peak Motion Regression

The regression for Fourier velocity or peak filtered motion is set up in a similar way to that for coda normalization. The linear equation used to describe the logarithm of the observed amplitude recorded at a distance

between nodes p and *(1-p)* is:

$$Y_k(f) = E_i(f) + Site_l(f) + pD_j(f) + (1 - p)D_{j+1}(f) \qquad (2.16)$$

the subindices represent:

$k = 1, 2, ..., n$ observations

$i = 1, 2, ..., ne$ earthquakes

$j = 1, 2, ..., m$ distance terms

$l = 1, 2, ..., ns$ sites

The linear system has the form

$$\mathbf{Y}_{\{n+m+1\}\times 1} = \mathbf{X}_{\{n+m+1\}\times\{m+ne+ns\}}\mathbf{D}_{\{m+ne+ns\}\times 1}$$

Y_m is the set of maximum amplitude observed in the Fourier or filtered time domain. The matrix equation represent the source, distance and site terms in a set of vertical columns. The rows added at the end represent the different constraints starting with the constraint on the site terms, following by the smoothing constraint, and the last line forces the distance attenuation functional to be zero at the reference distance.

24

$$
\begin{pmatrix} A_1 \\ A_2 \\ \vdots \\ \vdots \\ A_n \\ \cdots \\ 0 \\ \cdots \\ 0 \\ \vdots \\ \vdots \\ \vdots \\ 0 \\ \cdots \\ 0 \end{pmatrix}
=
\left(\begin{array}{cccc|ccccc|cccc}
1 & 0 & \cdots & 0 & 0 & p & 1-p & \cdots & 0 & 1 & 0 & \cdots & 0 \\
0 & 0 & \cdots & 0 & p & 1-p & 0 & \cdots & 0 & 0 & 0 & \cdots & 1 \\
\vdots & \vdots & & \vdots & \vdots & \vdots & & & \vdots & \vdots & \vdots & & \vdots \\
\vdots & \vdots & & \vdots & \vdots & \vdots & & & \vdots & \vdots & \vdots & & \vdots \\
0 & 0 & \cdots & 1 & 0 & 0 & p & \cdots & 0 & 0 & 1 & \cdots & 0 \\
\hline
0 & 0 & \cdots & 0 & 0 & 0 & 0 & \cdots & 0 & u & u & \cdots & u \\
\hline
0 & 0 & \cdots & 0 & -2w & w & 0 & \cdots & 0 & 0 & 0 & \cdots & 0 \\
\vdots & \vdots & & \vdots & w & -2w & w & \cdots & 0 & \vdots & \vdots & & \vdots \\
\vdots & \vdots & & \vdots & \vdots & \vdots & \ddots & & \vdots & \vdots & \vdots & & \vdots \\
\vdots & \vdots & & \vdots & \vdots & \vdots & & \ddots & \vdots & \vdots & \vdots & & \vdots \\
0 & 0 & \cdots & 0 & 0 & 0 & \cdots & w & -2w & 0 & 0 & \cdots & 0 \\
\hline
0 & 0 & \cdots & 0 & 0 & v & 0 & \cdots & 0 & 0 & 0 & \cdots & 0
\end{array} \right)
\times
$$

$$
\times
\begin{pmatrix}
SRC_1 \\ SRC_2 \\ SRC_3 \\ \vdots \\ SRC_{ne} \\ \cdots \\ D_1 \\ D_2 \\ D_3 \\ \vdots \\ \vdots \\ D_m \\ \cdots \\ SITE_1 \\ SITE_2 \\ SITE_3 \\ \vdots \\ SITE_{ns}
\end{pmatrix}
$$

Source Terms   Distance Terms   Site Terms

The matrix **X** is inverted in a least square sense using a Singular Value decomposition algorithm. Although the problem is linear, an iterative solution is used to adjust the constraint weights. The iterative regression stops when the perturbation for adjusting the weights is smaller than a predetermined threshold or when it reaches a certain number of iterations.

2.5 Random Vibration Theory

Once the regression is done, we model the empirical scaling relation using random vibration theory (RVT) that predicts the peak amplitude from the *rms* value. To estimate the maximum amplitude we only need to know the spectral shape and the duration T (Boore, 1983; Cartwright and Longuet-Higgins, 1956).

The first step estimates the zeroth, second and fourth moments of the energy density spectrum of the predicted signal spectra (see Chapter 4). The k_{th} moment is defined as

$$m_k = \frac{1}{\pi} \int_0^\infty \omega^k \left| A(\omega) \right|^2 d\omega \qquad (2.17)$$

Where $A(\omega)$ is the amplitude spectrum of the source term (see section 4.5 for more details). The predominant frequency f_c of the peaks, and the number N, of maxima to be exceeded is estimated as follow

$$f_c = \frac{1}{2\pi} \left(m_4 / m_2 \right)^{\frac{1}{2}} \qquad (2.18)$$

and

$$N = 2 f_c T \qquad (2.19)$$

where T is the duration defined in Figure 2.3.

Cartwright and Longuet-Higgins (CLH) (1956) described the statistical distribution of the maxima of a random function. They gave an expression for the ratio of peak to rms

$$\overline{\eta}_{max} = \frac{a_{peak}}{a_{rms}} \tag{2.20}$$

The integral (equation 6.3 of CLH) that describes $\overline{\eta}_{max}$ is

$$\overline{\eta}_{max} = \int_{-\infty}^{+\infty} \eta \frac{d}{d\eta} \left[1 - q(\eta)\right]^N \tag{2.21}$$

where η is the variable that describe the heights of a maxima (velocity or acceleration) and $q(\eta)$ is the cumulative probability of exceeding η. This expression is solved by separating the integral into two terms, from $-\infty$ to 0 and from 0 to ∞ and integrating by parts (CLH equation 6.4)

$$\overline{\eta}_{max} = \int_{-\infty}^{0} \left[1 - q(\eta)\right]^N d\eta + \int_{0}^{\infty} \left\{1 - \left[1 - q(\eta)\right]^N\right\} d\eta \tag{2.22}$$

CLH also showed that $q(\eta)$ only depends on the spectral density moments (see Appendix for details). This integral is solved numerically and the peak amplitude a_{peak} is estimated from equation (2.20).

The equations above show that after choosing the duration T, the relation between maximum amplitudes and rms amplitudes depends only on moments of the ground motion spectrum. As shown, RVT is used not only for estimating a peak amplitude of the expected ground motion velocity or acceleration, but also includes a very important parameter for engineering purposes: the duration. Thus, the duration helps to model the propagation and excitation terms of time domain observations more accurately.

3. Ground Motion Scaling in Central Mexico

3.1   Previous Work

Ordaz and Singh (1992), studied the source spectra and the spectral attenuation of seismic waves from Mexican earthquakes. They used eight earthquakes recorded on strong motion accelerographs from the Guerrero network (Anderson et al., 1994) with epicenters near the coast. The functional form used in their regression was

$$log(A_i(f,r)) - log(g(r)) - logC = logS_i(f) - 1.36fR/\beta Q(f) \qquad (3.1)$$

where $A(f,r)$ is the maximum acceleration observed in a narrow-filtered time series, $g(r)$ is the geometrical spreading function, C is a constant that combines radiation pattern and decomposition of horizontal and vertical components, $S(f)$ is the source term, R the hypocentral distance, β is the average shear wave velocity and $Q(f)$ the anelastic attenuation function.

The geometrical spreading $g(r)$ was assumed to be

$$g(r) \begin{cases} r^{-1} & r \leq 100 \, km \\ r^{-0.5} & r \geq 100 \, km \end{cases} \qquad (3.2)$$

and the frequency dependent attenuation function they found was

$$Q(f) = 273 \, f^{0.66} \qquad (3.3)$$

In their work, Ordaz and Singh also studied major earthquakes to compare the amplification of the seismic waves observed in the Hill Zone sites of México City with the coastal sites. The cross over distance of 100 km was fixed. The attenuation relation covered distances up to 400 km, but represents different paths than those presented in this dissertation. Ordaz and Singh (1992) also studied the source spectra and fit the observed

variations with an ω^2 model. The stress parameter $\Delta\sigma$ needed to fit the high frequencies of large events was between 50 to 300 bars; smaller earthquakes required higher values $\Delta\sigma$ (200 to 800 bars). Castro et. al. (1990) studied the same region as Ordaz and Singh, using observations recorded at smaller distances, $r \leq 320$ km, resulting in few differences with the Ordaz and Singh (1982) results at lower frequencies (< 1Hz). The low frequency difference reflect differences in the data set and the details of the analysis technique. For these frequencies Q_o in Castro et al.'s (1990) study became negative.

All previous work relied on data from frequent large coastal events. To the author's knowledge, this is the first time that a predictive relationship has been constructed using the inland local and regional earthquakes. The different propagation paths and source characteristics may lead to apparent differences from the results of earlier studies.

3.2 Data Set

Data from two seismic networks were used in this analysis. The first is the short-period México Valley Network (RSVM), which consists of 12 short period stations located along the Valley of México. The second network is the national broadband seismic network of the Servicio Sismológico Nacional (SSN) at the Instituto de Geofísica UNAM (see Table 3.1). A typical RSVM station consists of an L-4 1-Hz vertical short-period seismometer digitized at 40 sps or a Mark-4 1-Hz three-component seismometer sampled at 30 sps (Table 3.2). Continuous data are transmitted digitally and saved in near real-time.

Site description

Network	Name	ID	Lithology	Lat	Long
RSVM	Ayaqueme	AYVM	Quaternary Tuff	$19°10.07'$	$98°57.25'$
RSVM	Cerro Gordo	CGVM	Quaternary Tuff	$19°45.00'$	$98°49.76'$
RSVM	Cilcuayo	CIVM	Upper Tertiary Breccia	$19°06.18'$	$98°58.80'$
BB	Ciudad Universitaria	CUIG	Miocene Breccia	$19°19.74'$	$99°10.68'$
RSVM	Chichinautzin	CHVM	Quaternary Breccia	$19°05.24'$	$99°08.84'$
RSVM	El Pino	PNVM	Upper Tertiary Andesite	$19°20.82'$	$98°55.08'$
BB	Iguala	PLIG	Cretaceous Limestone	$18°23.54'$	$99°30.14'$
RSVM	Madin	MDVM	Miocene Andesite	$19°32.19'$	$99°14.94'$
BB	Morelia	MOIG	Cretaceous Limestone	$19°40.68'$	$101°11.34'$
RSVM	Loma del Muerto	LMVM	Quaternary Breccia	$19°06.00'$	$98°42.90'$
RSVM	Organos	ORVM	Quaternary Breccia	$19°35.49'$	$98°43.35'$
RSVM	Peñón de los Baños	PBVM	Upper Tertiary Basalt	$19°26.47'$	$99°05.06'$
RSVM	Pico Tres Padres	PTVM	Upper Tertiary Andesite	$19°35.58'$	$99°06.78'$
BB	Popocatépetl	PPIG	Upper Tertiary Breccia	$19°04.00'$	$98°37.60'$
RSVM	Rio Frio	RFVM	Soil Quaternary sediments	$19°19.99'$	$98°45.70'$
RSVM	Salazar	SZVM	Upper Tertiary Andesite	$19°19.38'$	$99°22.86'$
BB	Yautepec	YAIG	Cretaceous Limestone	$18°51.72'$	$99°04.02'$

Table 3.1: Information concerning the stations of the RSVM and BB networks.

The data set consists of a total of 226 earthquakes with 52 of those recorded by both networks. A total of 780 waveforms recorded between 1994 and 1999 were used for the analysis. The data were carefully reviewed for event mislocations, noisy stations and multiple events. For each waveform the first arrivals of P and S waves were picked using hypocentral distance as a guide. Others studies that have applied the same technique (Malagnini 2000a,b) have used several thousand waveforms, I obtained robust results using the quality data of this data set.

Figure 3.1 shows the short-period RSVM (diamonds) and broad-band, BB (triangles), stations and earthquake locations used in this study. In general, the RSVM network triggers on shallow low-magnitude events, and the BB stations record regional events at larger distance ranges. Solid circles represent the earthquakes that triggered the RSVM network and open circles are those that triggered the BB recording. A depth-distance profile

Sensor history						
Station	Component	Init. Time	End Time	Filter	Sensor	Comments
AYVM	EHZ	8/17/97	6/01/98	5 Hz	L-4	Stolen
AYVM	EHZ	12/01/94	8/16/97	10 Hz	L-4	Changed
SZVM	EHZ	11/13/97	-	5 Hz	L-4	In Operation
SZVM	EHZ	9/01/93	11/13/97	10 Hz	L-4	Changed
PTVM	EHZ	7/09/97	-	5 Hz	L-4	In Operation
PTVM	EHZ	2/01/95	7/08/97	10 Hz	L-4	Changed
ORVM	EHZ	10/01/96	-	5 Hz	L-4	In Operation
MDVM	EHZ	8/01/96	-	10Hz	L-4	In Operation
CGVM	EHZ	9/11/97	-	5 Hz	Lennartz	In Operation
CGVM	EHN	9/11/97	-	5 Hz	Lennartz	In Operation
CGVM	EHE	9/11/97	-	5 Hz	Lennartz	In Operation
CGVM	EHZ	6/01/93	9/10/97	5 Hz	Lennartz	Changed
CGVM	EHN	6/01/93	9/10/97	5 Hz	Lennartz	Changed
CGVM	EHE	6/01/93	9/10/97	5 Hz	Lennartz	Changed
CIVM	EHZ	6/10/99	-	5 Hz	Lennartz	In Operation
CIVM	EHN	6/10/99	-	5 Hz	Lennartz	In Operation
CIVM	EHE	6/10/99	-	5 Hz	Lennartz	In Operation
PNVM	EHZ	1/10/93	8/10/96	10 Hz	L-4	Station removed
CHVM	EHZ	8/08/97	-	5 Hz	L-4	In Operation
CHVM	EHZ	3/01/94	8/09/97	10 Hz	L-4	Changed
LMVM	EHZ	1/01/93	-	10 Hz	L-4	In Operation
RFVM	EHZ	5/29/97	-	5 Hz	L-4	In Operation
CIVM	EHZ	5/01/99	-	5 Hz	Lennartz	In Operation
CIVM	EHN	5/01/99	-	5 Hz	Lennartz	In Operation
CIVM	EHE	5/01/99	-	5 Hz	Lennartz	In Operation
PBVM	EHZ	5/01/93	-	10 Hz	L-4	In Operation

Table 3.2: RSVM Network operation

(Figure 3.1) shows two different source-regions in the zone. The first region is a shallow zone related to the TMVB (faults systems and volcanic activity) that provides the short distance data. The second region includes the deeper earthquakes (> 40 km) which have caused severe damage to the inland towns (Singh et al., 1999). Figure 3.2 shows the event depth distribution, the shallow events are in the range from 0 to 20 km, and the deeper earthquakes from 40 to 100 km. The problems caused by deep earthquakes in the data set will be discussed later in Chapter 4.

Before continuing I describe some tradeoffs between the excitation, site and distance terms in the regression model. Two extreme scenarios illustrate the problem. If observations from one event dominate a distance range, then there will be a tradeoff between the excitation for that event and the corresponding distance terms, especially in the case where the azimuthal coverage is poor and the radiation pattern differs from our initial assumptions. In another extreme example, if only one station appears at a narrow range of distances and if it has anomalous site response, then the *D(r)* could be distorted by this station and a bias could be introduced in all other site terms.

In practice, plotting the observation distances by event and by station provides a good diagnostic for discarding events, defining the distance nodes, and estimating the quality of our distance coverage. Figures 3.3 and 3.4 show the distance coverage for the RSVM and BB stations.
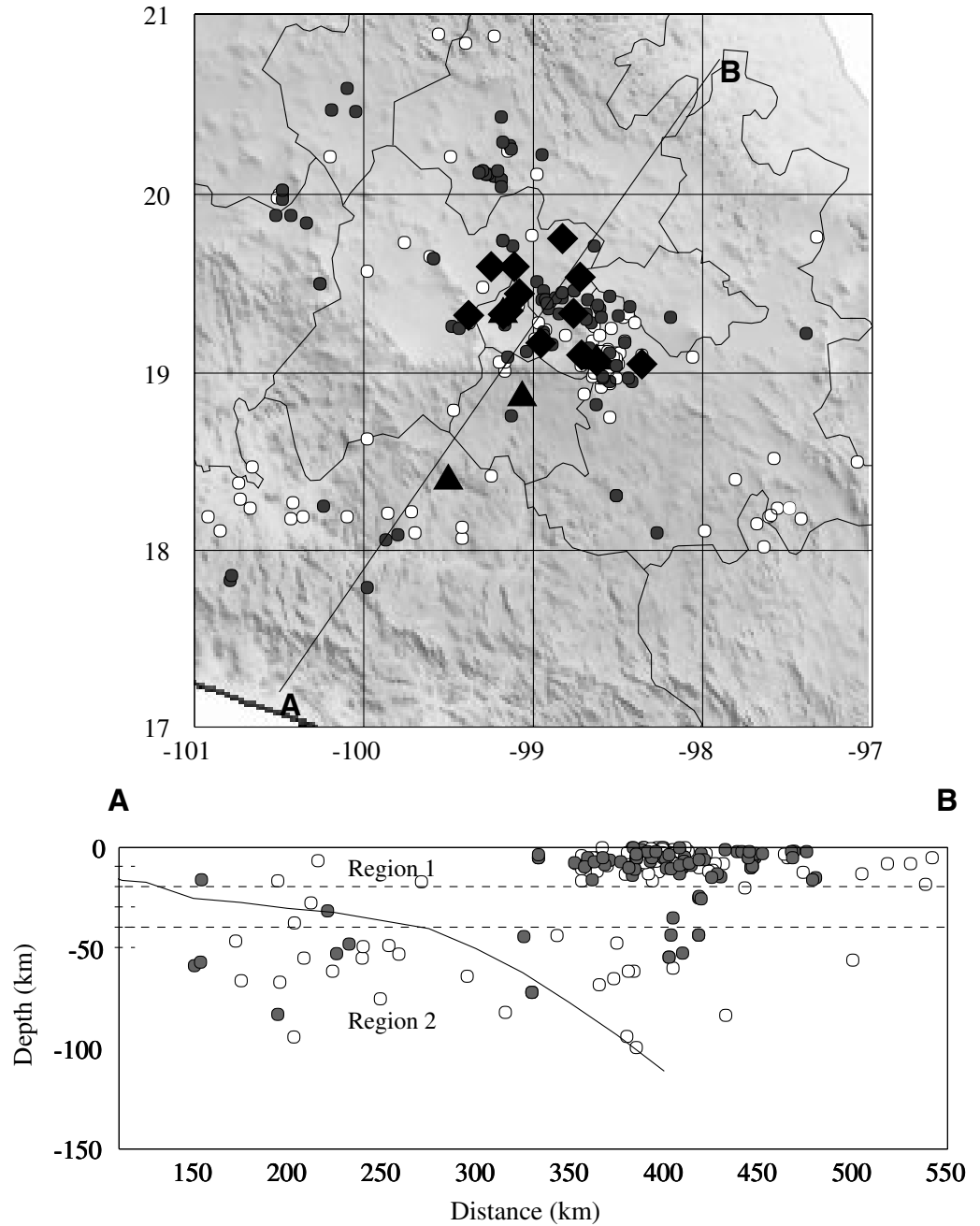
Figure 3.1: Locations of SP (diamonds) and BB (triangles) stations and earthquakes (open circles triggered by the BB network, solid circles by the RSVM). The profile is perpendicular to the trench. The subducting slab proposed by Pardo and Suarez (1995) is shown by the solid line dipping northeast.
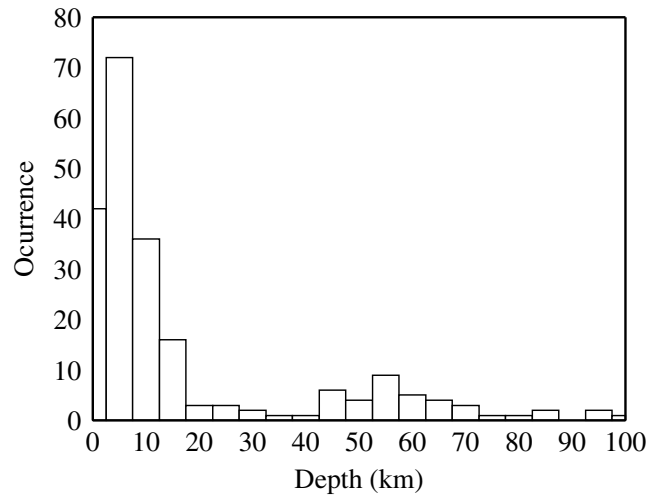
Figure 3.2: Histogram showing the depth distribution. The data set consist mainly of shallow events (less than 20 km) and deeper earthquakes from 40 to 100 km.
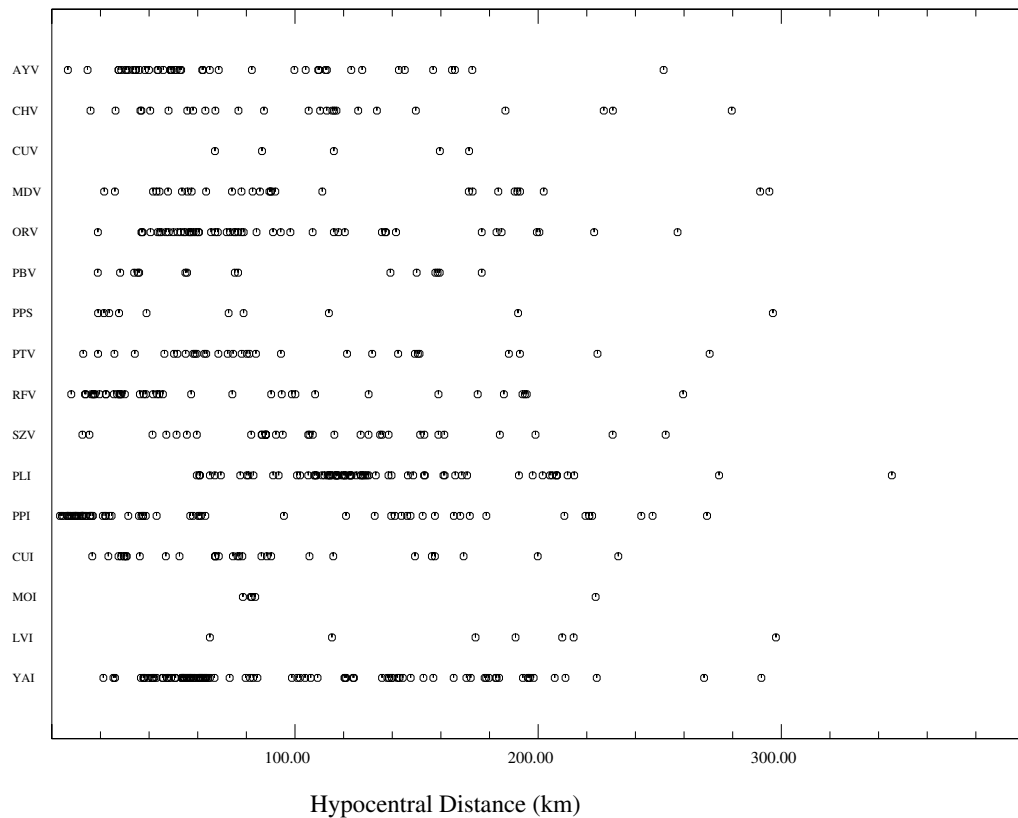
Figure 3.3: Distance coverage for RSVM and BB stations. The observation distances for each station should cover a wide range overlaps and with other stations to avoid a tradeoff between the excitation and distance term.
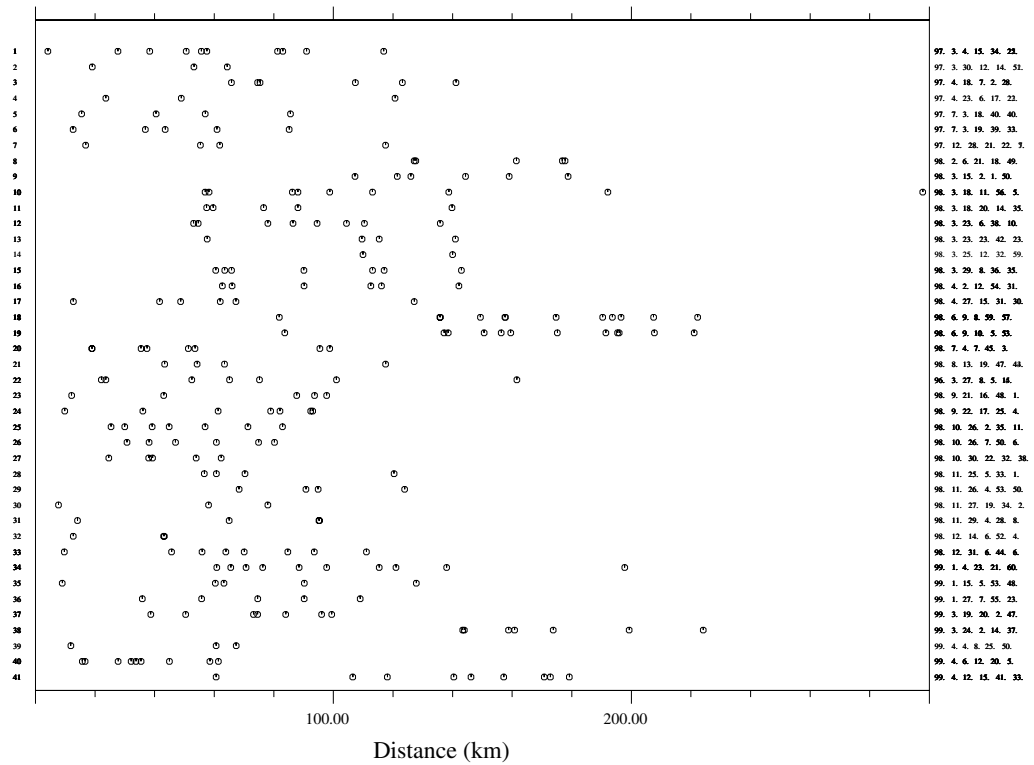
Figure 3.4: Distance coverage by event for RSVM and BB stations for a subset of events.

3.3   Coda Shape

Figures 3.5 to 3.9, show the decay shape of the normalized coda with time. The RMS average over a 256 point running window is computed for each time series and plotted as a function of time. The black lines are the initial part before the P-wave arrival, this portion is used as the background noise of the seismic record. The gray lines refer to the seismic signal between P and S-wave arrivals, the light gray refer to the RMS average between the S-wave arrival and the stable coda, and finally the dark segment of the curves start at $2t_s$ and describe the RMS of the coda as a function of time. Each peak is normalized to the value of the coda at a reference level. This display graphically illustrates the coda normalization technique and provides a visual check on the coda shape function. The figures show the average coda shape. From a visual inspection of each plot we can see that the distribution of the normalized amplitudes includes the presence of large outliers for all frequencies. Although most observations cluster tightly, some outliers may influence the results (e.g. near 125 s on the $f = 4$ Hz plot, Figure 3.8). The coda shape is well defined in the segment of the stable coda after the $2t_s$.

Comparing the propagation term estimated using the general regression (described in the next section) with the coda normalization estimate, I found that the coda normalization does not fit the regression results well (Figures 3.10, 3.11, 3.12). As frequency increases (from 0.7 to 2 Hz) there is a slightly better agreement. However, from 2 to 7 Hz, there is again an increasing discrepancy with increasing frequency. The difference is profound at short distances. The coda normalization works when the peak
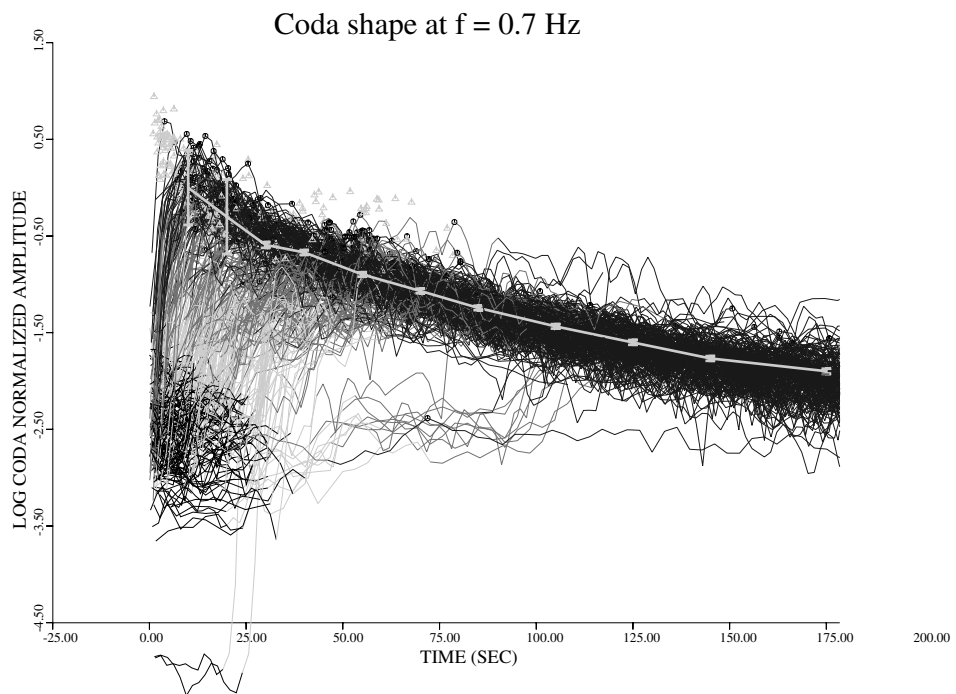
Figure 3.5: Shape of the 0.7 Hz seismic coda as a function of time. The black lines are the initial part before the P-wave arrival, gray lines refer to the seismic signal between P and S-wave arrivals, light gray refer to the RMS average between the S-wave arrival and the stable coda, and finally the dark segment of the curves start at 2 *ts*. Gray triangles indicate the peak values.
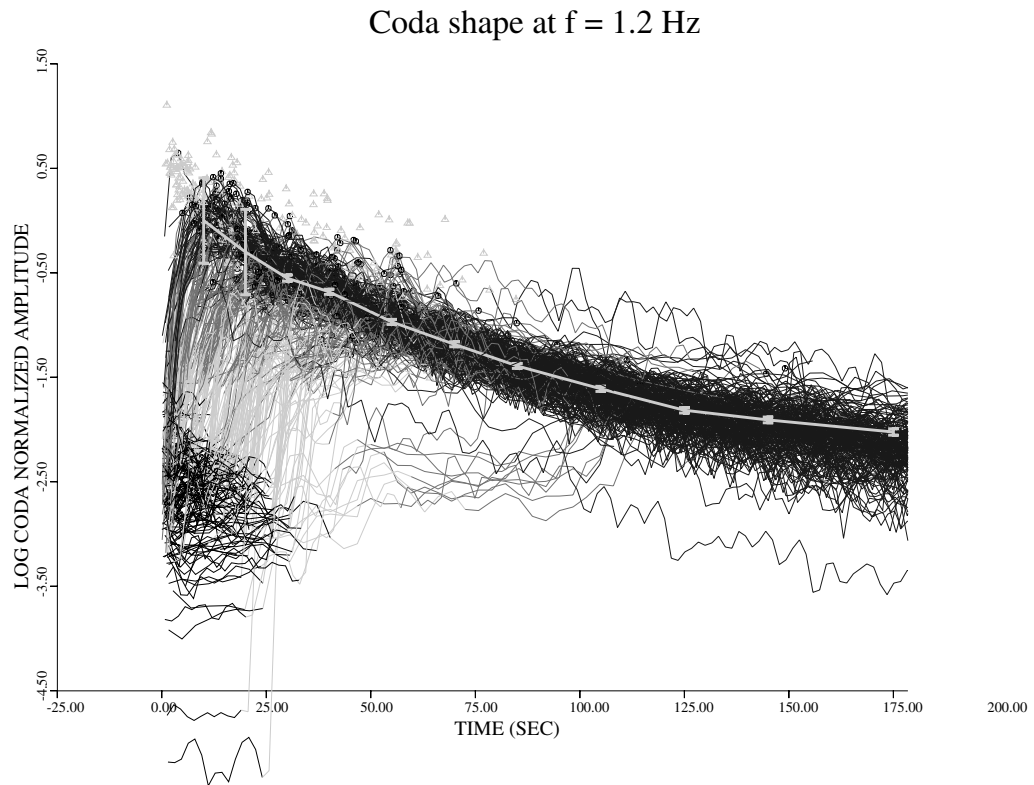
Figure 3.6: Shape of the 1.2 Hz seismic coda as a function of time. The black lines are the initial part before the P-wave arrival, gray lines refer to the seismic signal between P and S-wave arrivals, light gray refer to the RMS average between the S-wave arrival and the stable coda, and finally the dark segment of the curves start at 2 *ts*. Gray triangles indicate the peak values.
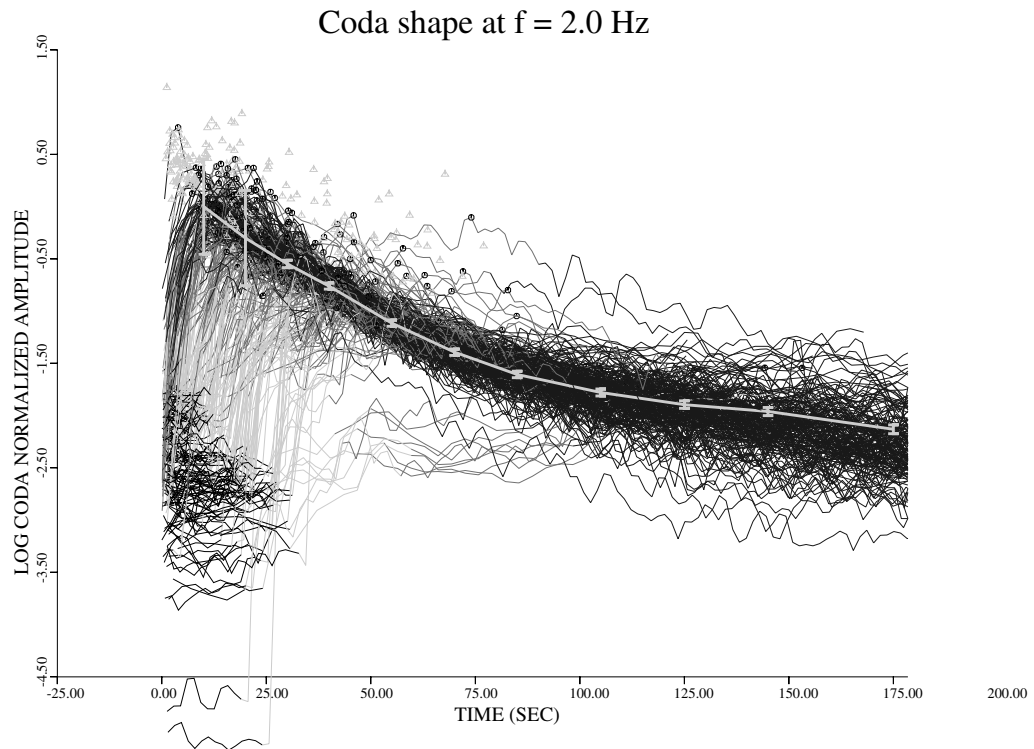
Figure 3.7: Shape of the 2.0 Hz seismic coda as a function of time. The black lines are the initial part before the P-wave arrival, gray lines refer to the seismic signal between P and S-wave arrivals, light gray refer to the RMS average between the S-wave arrival and the stable coda, and finally the dark segment of the curves start at 2 *ts*. Gray triangles indicate the peak values.
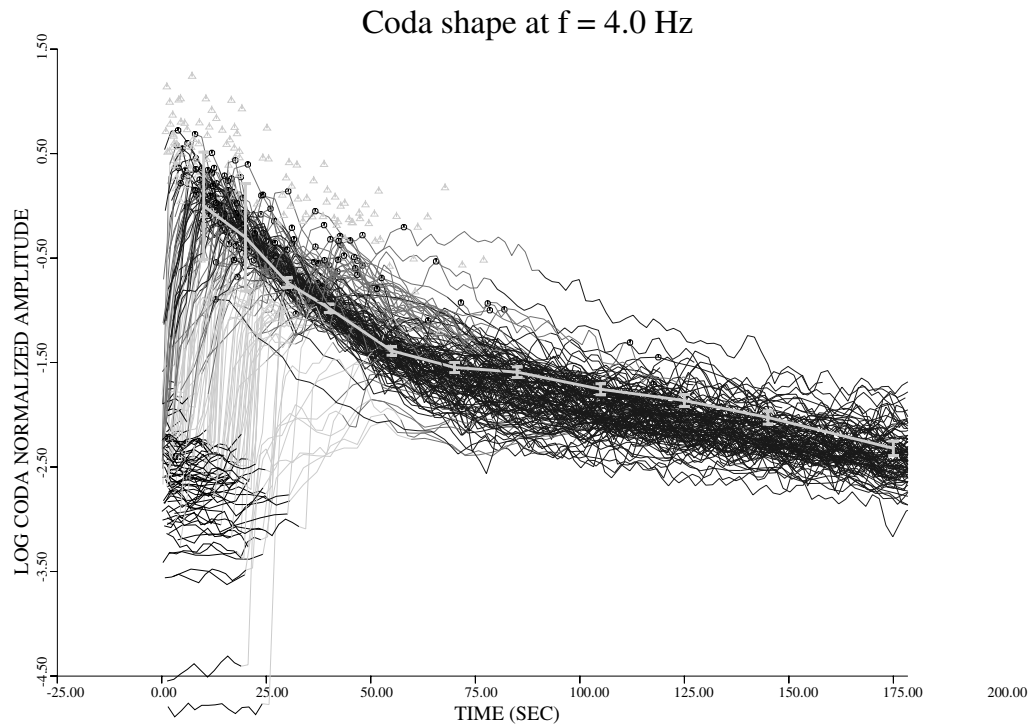
Figure 3.8: Shape of the 4.0 Hz seismic coda as a function of time. The black lines are the initial part before the P-wave arrival, gray lines refer to the seismic signal between P and S-wave arrivals, light gray refer to the RMS average between the S-wave arrival and the stable coda, and finally the dark segment of the curves start at 2 *ts*. Gray triangles indicate the peak values.

Coda shape at f = 6.0 Hz
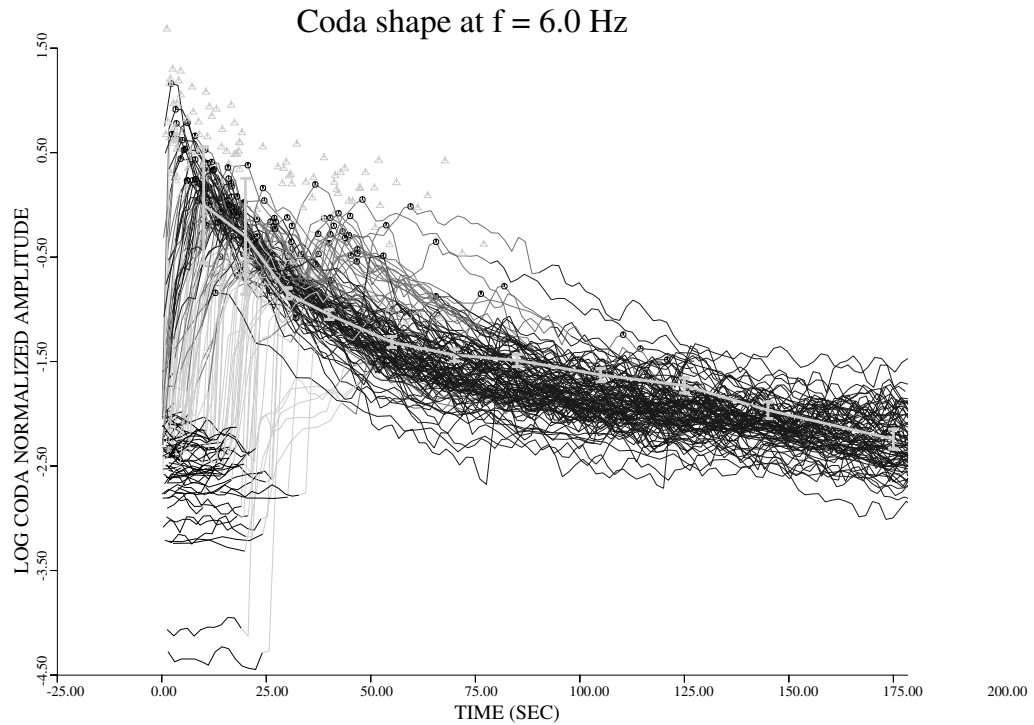
Figure 3.9: Shape of the 6.0 Hz seismic coda as a function of time. The black lines are the initial part before the P-wave arrival, gray lines refer to the seismic signal between P and S-wave arrivals, light gray refer to the RMS average between the S-wave arrival and the stable coda, and finally the dark segment of the curves start at 2 *ts*. Gray triangles indicate the peak values.
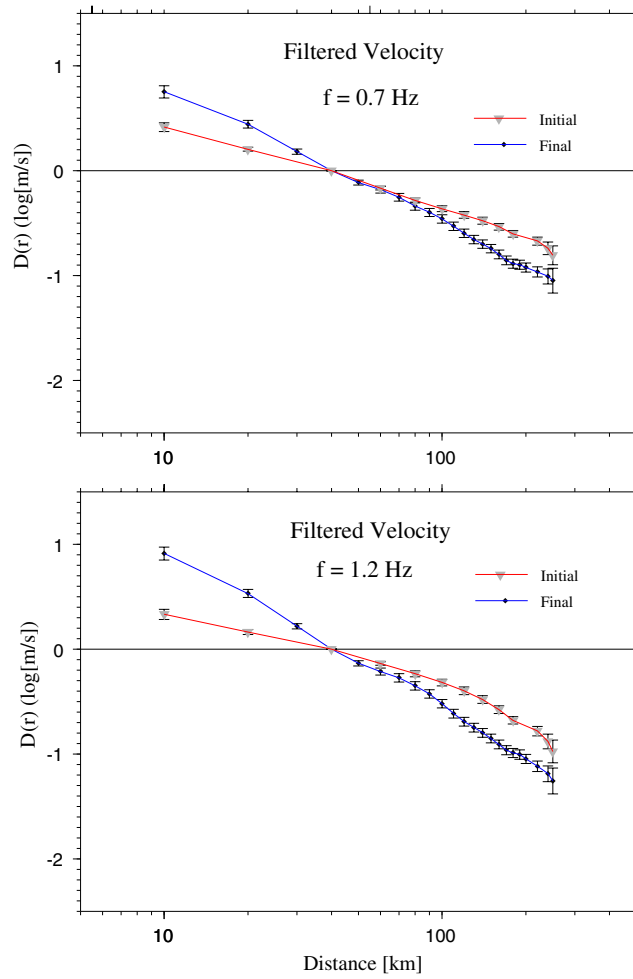
Figure 3.10: Comparison between the attenuation functional from the general regression (black or blue) and its estimate computed using the coda normalization (gray or red) at 0.7 and 1.2 Hz.
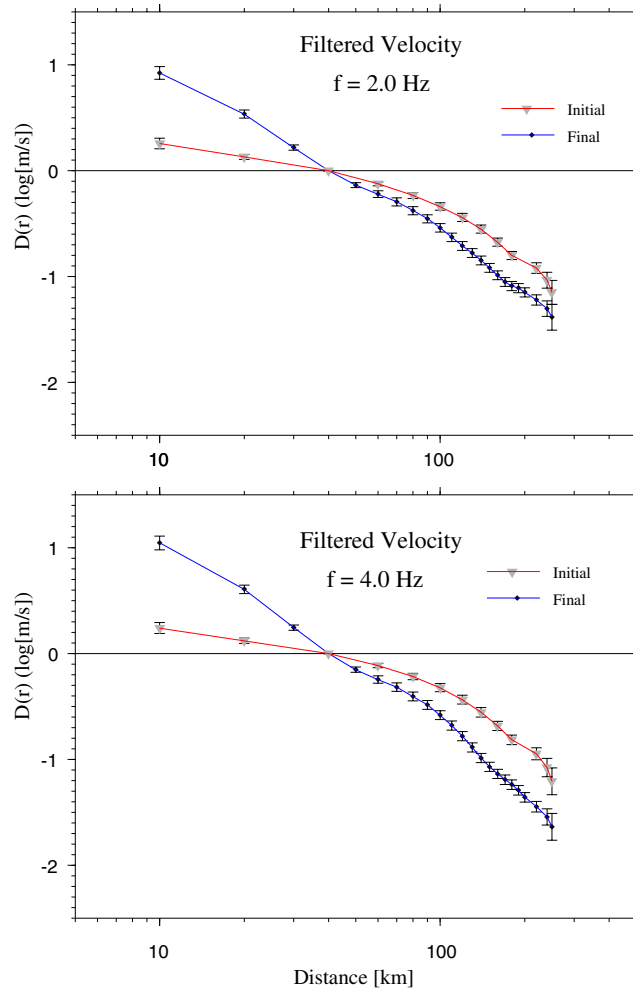
Figure 3.11: Comparison between the attenuation functional from the general regression (black or blue) and its estimate computed using the coda normalization (gray or red) at 2.0 and 4.0 Hz.
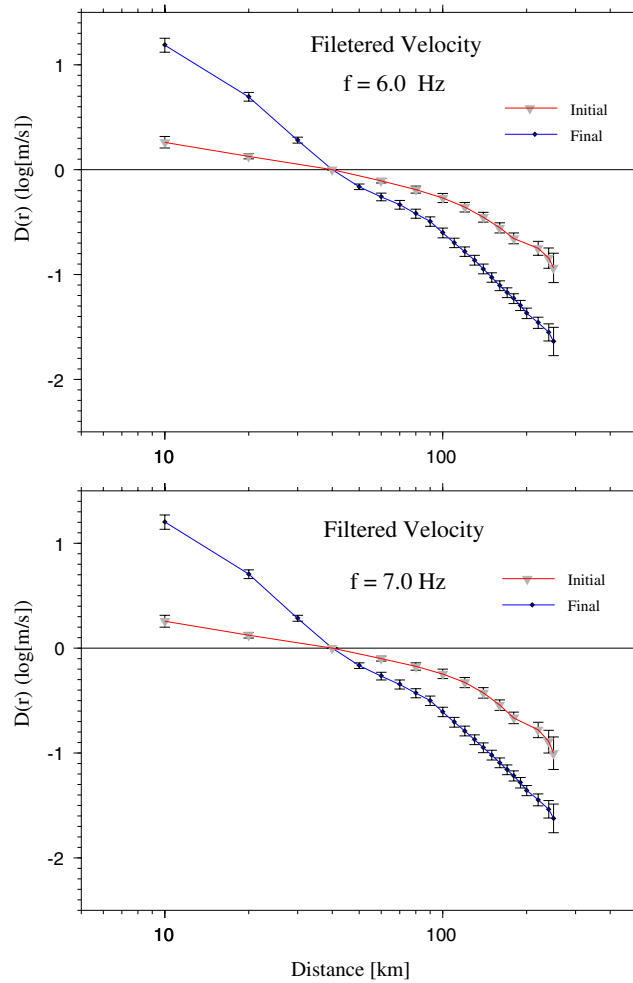
Figure 3.12: Comparison between the attenuation functional from the general regression (black or blue) and its estimate computed using the coda normalization (gray or red) at 6.0 and 7.0 Hz.

motion part of the seismogram consists of many rays as expected at distances much greater than the source depth and if both coda and peak motion sample similar paths of the focal sphere. Both assumptions are most likely to be valid in shallow events. However for deeper earthquakes the focal sphere might not be adequately sampled, since we are looking more at direct body waves than waves trapped in the crust. This discrepancy on the coda normalization and $D(r)$ may be related to the depth coverage and will be discussed later on this chapter. Still, the coda normalization technique provides a first estimate of $D(r)$, even when it does not fit well for some frequencies. On other regions studied using this technique, the coda normalization works well, such as California (Raoof et al., 1999) and Italy (Malagnini et al., 2000a, 2000b).

3.4   General Data Regression

A regression was carried out for 10 frequencies in the interval of 0.7 to 7 Hz using a reference distance $r_{ref} = 40$ km. Figures 3.13, 3.14 and 3.15 illustrate typical examples of the regression analysis results for the filtered velocity, presenting 1.2, 3.0 and 6.0 Hz results respectively. It also shows the initial propagation term estimated using the coda normalization technique. Figures 3.16, 3.17 and 3.18 present a similar display for the Fourier velocity spectra. I note that the coda normalization is less robust for the Fourier amplitude than the filtered velocity, but in both cases the regression converges to similar results. In general the *D(r)* is characterized by the presence of large outliers at all frequencies in both domains.

To perform the regression the site term at hard-rock station PLIG was

constrained to be zero (Constraint 2b in section 2.2). Figure 3.19 is a comparison of the distance scaling $D(r)$ at the ten different frequencies for the regression on the Fourier velocity spectra and band-pass filtered time-domain peak motion. In the illustration, the $D(r)$ are corrected for an r^{-1} trend to emphasize departure from r^{-1} spreading. The estimated $D(r)$ is similar using observations from both domains. This is a good test of the consistency in the duration on the time-domain observations, since effects in geometrical spreading on the spectra and frequency dependent Q must be the same, any difference in the results must be the effect of a duration, which ties the two domains together.

Our distance scaling term $D(r)$ expresses the combined effect of the geometrical spreading and anelastic and scattering attenuation, but other propagation effects may also be present, e.g. the existence of geological structures that permit an efficient transmission of the seismic energy on a regional scale. These other effects are averaged over in a model in which motion depends only upon hypocentral distances. Figures 3.20, 3.21, 3.22 and 3.23 show the final residuals at the different frequencies. The histogram at the right show the number of occurrence for different residual levels. In general more than 90% of the residuals fit within the interval of ± 0.5 log 10 units. Tables 3.3 to 3.8 contain the final propagation terms from the general regression. These are the key results of this work.

The filtered peak velocity and Fourier velocity attenuation functional tables show important information about the data set. The number of observation is greater at distances between 40 and 80 km, where the uncertainty is low. The distance nodes used were evenly spaced each 20 km except for the first and the last nodes. At low frequencies the uncertainties
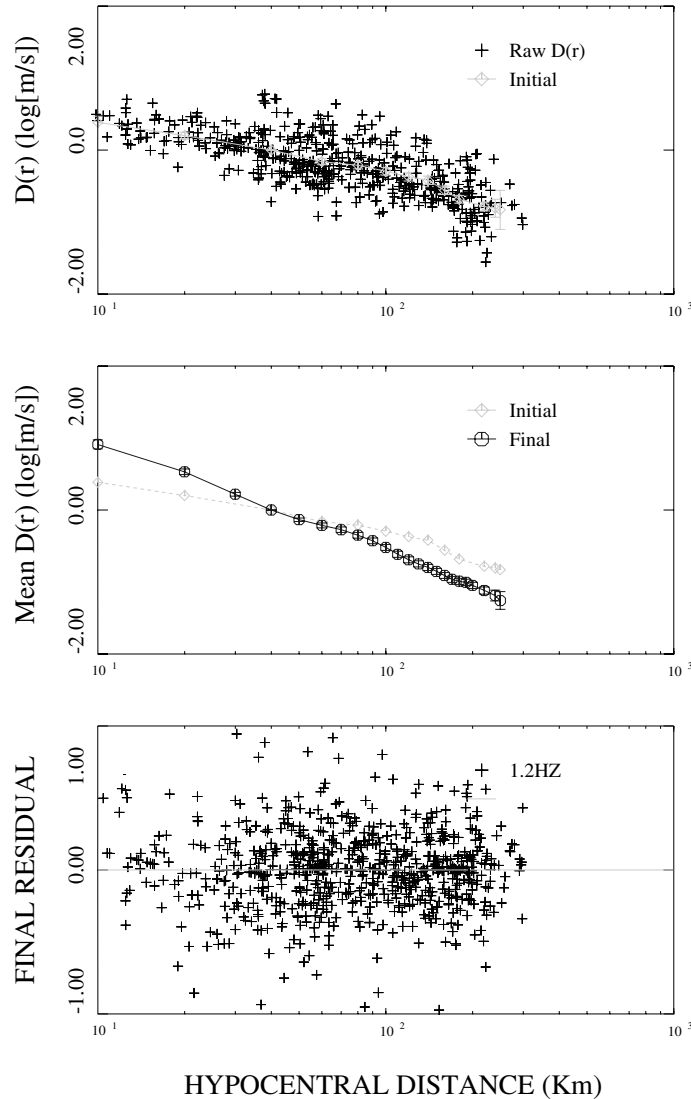
Figure 3.13: Time domain regression analysis for 1.2 Hz. Top, initial estimate of D(r) using the coda normalization technique. Shown on top of observations used in the general regression. Middle, initial and final propagation functionals. Bottom, final residuals of the regression analysis.

Regression Analysis for f = 3.0 Hz

Filtered Velocity
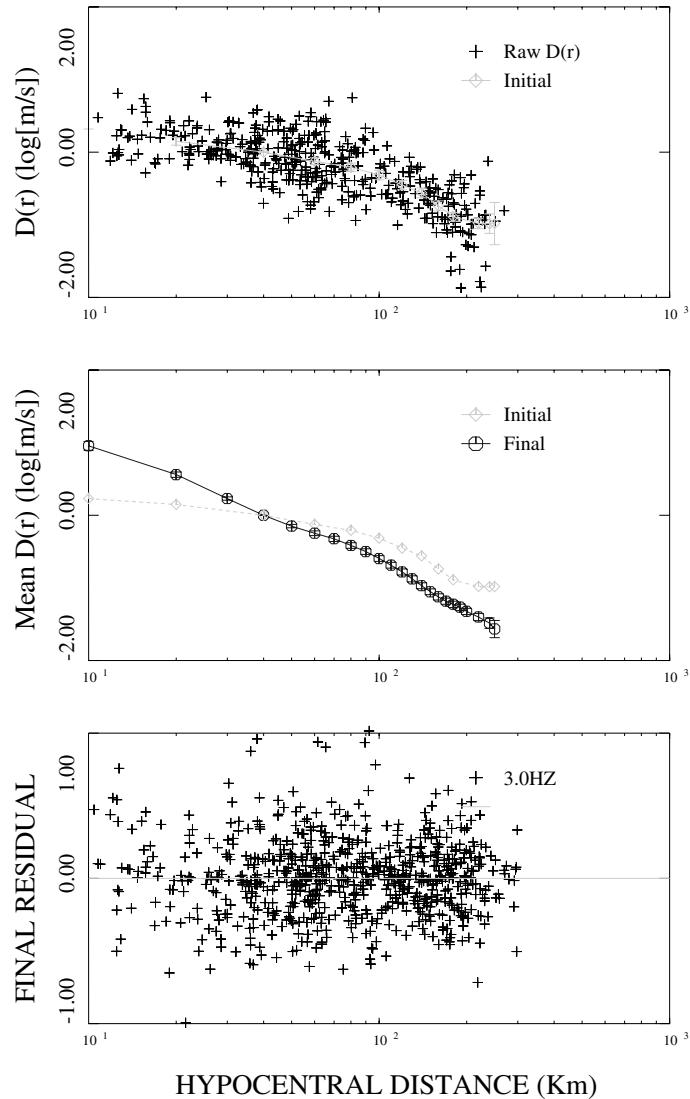
Figure 3.14: Time domain regression analysis for 3.0 Hz. Top, initial estimate of D(r) using the coda normalization technique. Shown on top of observations used in the general regression. Middle, initial and final propagation functionals. Bottom. final residuals of the regression analysis.

Regression Analysis for f = 6.0 Hz

Filtered Velocity
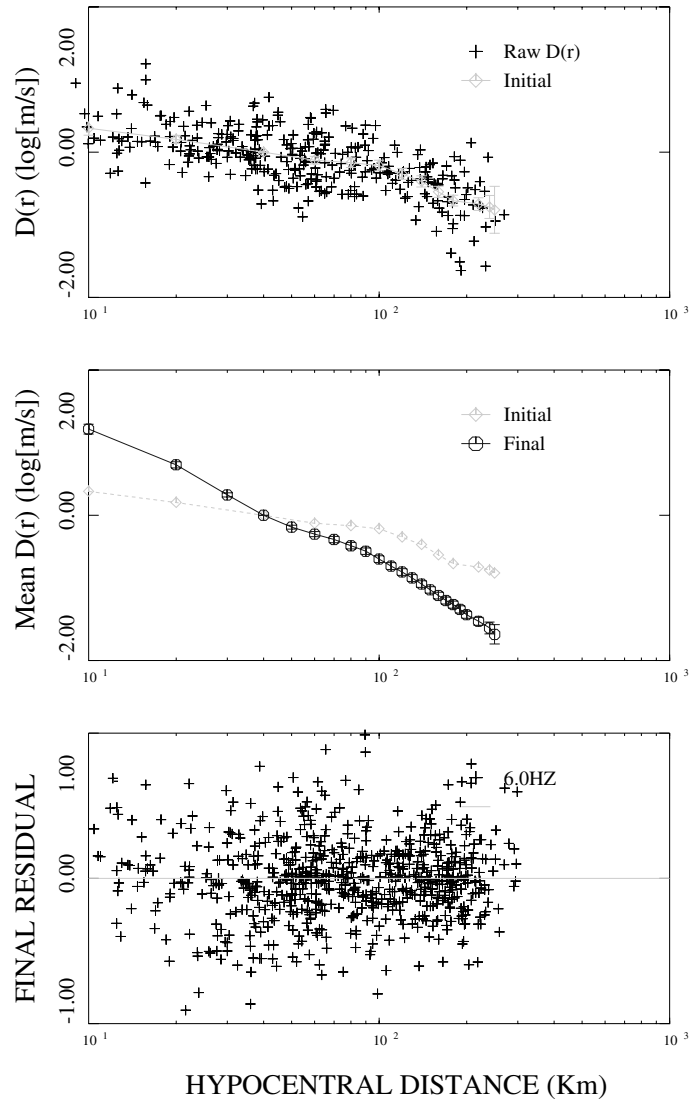
Figure 3.15: Time domain regression analysis for 9.0 Hz. Top, initial estimate of D(r) using the coda normalization technique. Shown on top of observations used in the general regression. Middle, initial and final propagation functionals. Bottom, final residuals of the regression analysis.
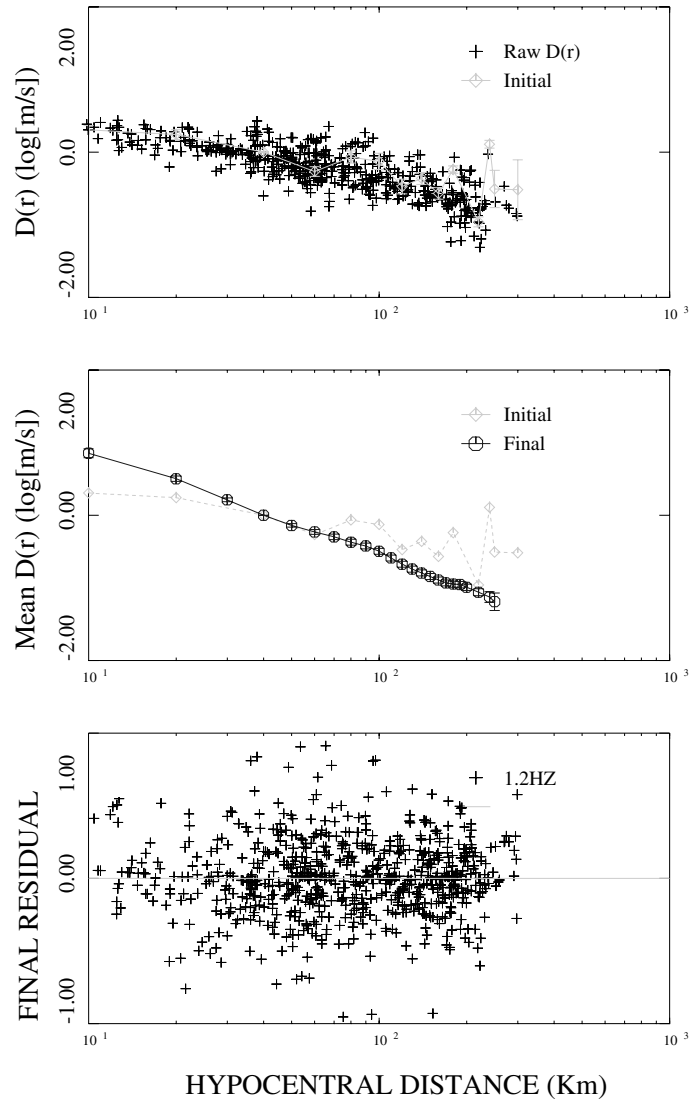
Figure 3.16: Fourier velocity regression analysis for 1.2 Hz. Top, initial estimate of D(r) using the coda normalization technique. Shown on top of observations used in the general regression. Middle, initial and final propagation functionals. Bottom, final residuals of the regression analysis.
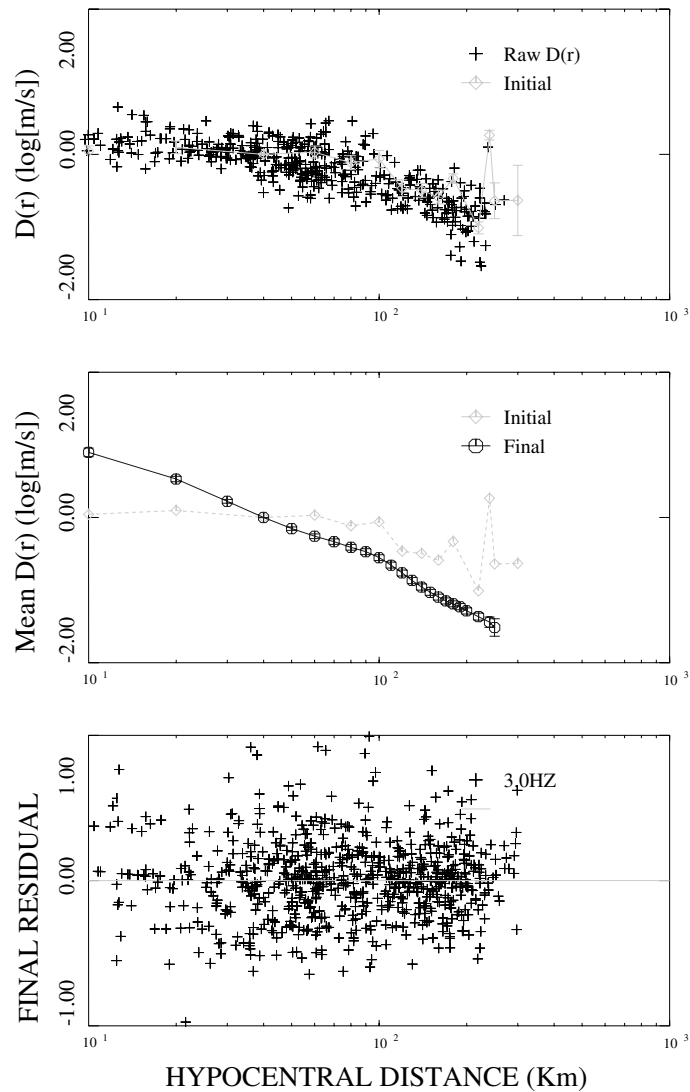
Figure 3.17: Fourier velocity regression analysis for 3.0 Hz. Top, initial estimate of D(r) using the coda normalization technique. Shown on top of observations used in the general regression. Middle, initial and final propagation functionals. Bottom, final residuals of the regression analysis.

Regression Analysis for f = 6.0

Fourier Velocity
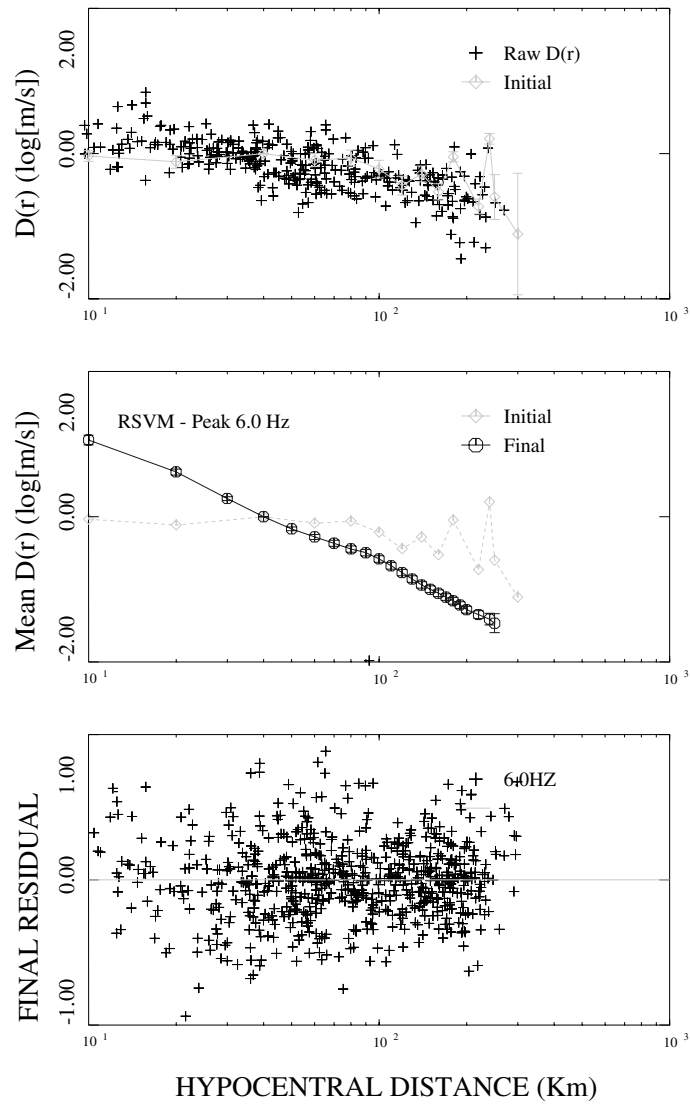
Figure 3.18: Fourier velocity regression analysis for 6.0 Hz. Top, initial estimate of D(r) using the coda normalization technique. Shown on top of observations used in the general regression. Middle, initial and final propagation functionals. Bottom, final residuals of the regression analysis.

Filtered Velocity   Fourier Velocity
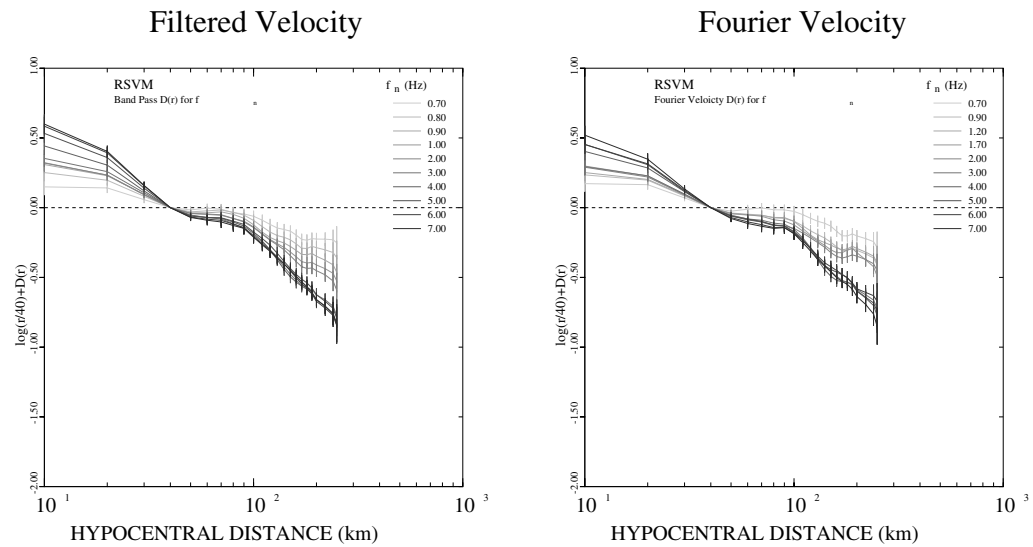
Figure 3.19: Comparison between the filtered time domain D(r) and the Fourier velocity corrected for 1/r geometrical spreading. Error bars are plotted.

are lower than at high frequencies. Also we can see that, in general, the filtered velocity attenuation functional have lower uncertainties than the Fourier ones, perhaps reflecting effect of noise associated with determining a good duration window.
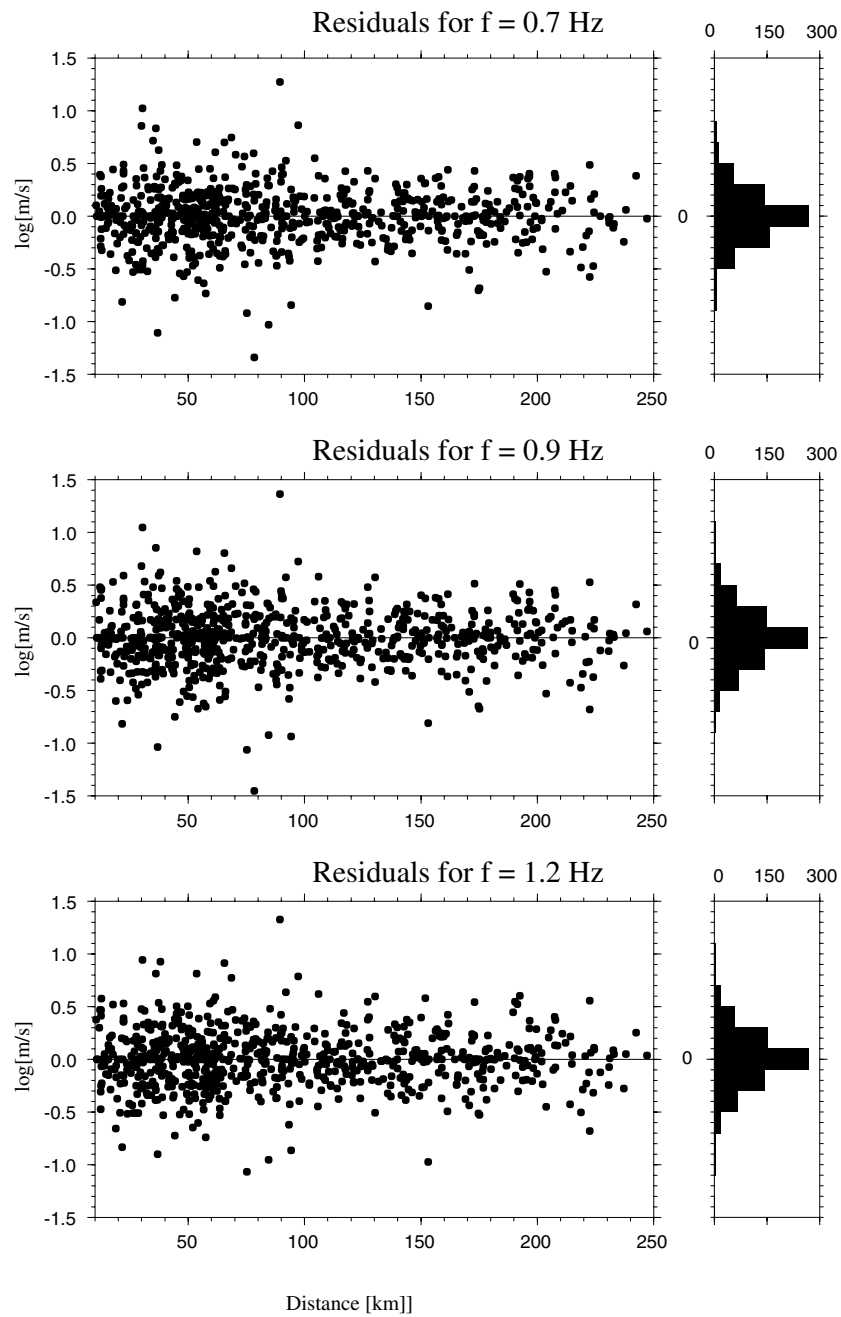
Figure 3.20: Final filtered velocity residuals at 0.7, 0.9 and 1.2 Hz. Each symbol represents one measurement, the histogram on the right indicates the number of measurements in 0.2 log units.
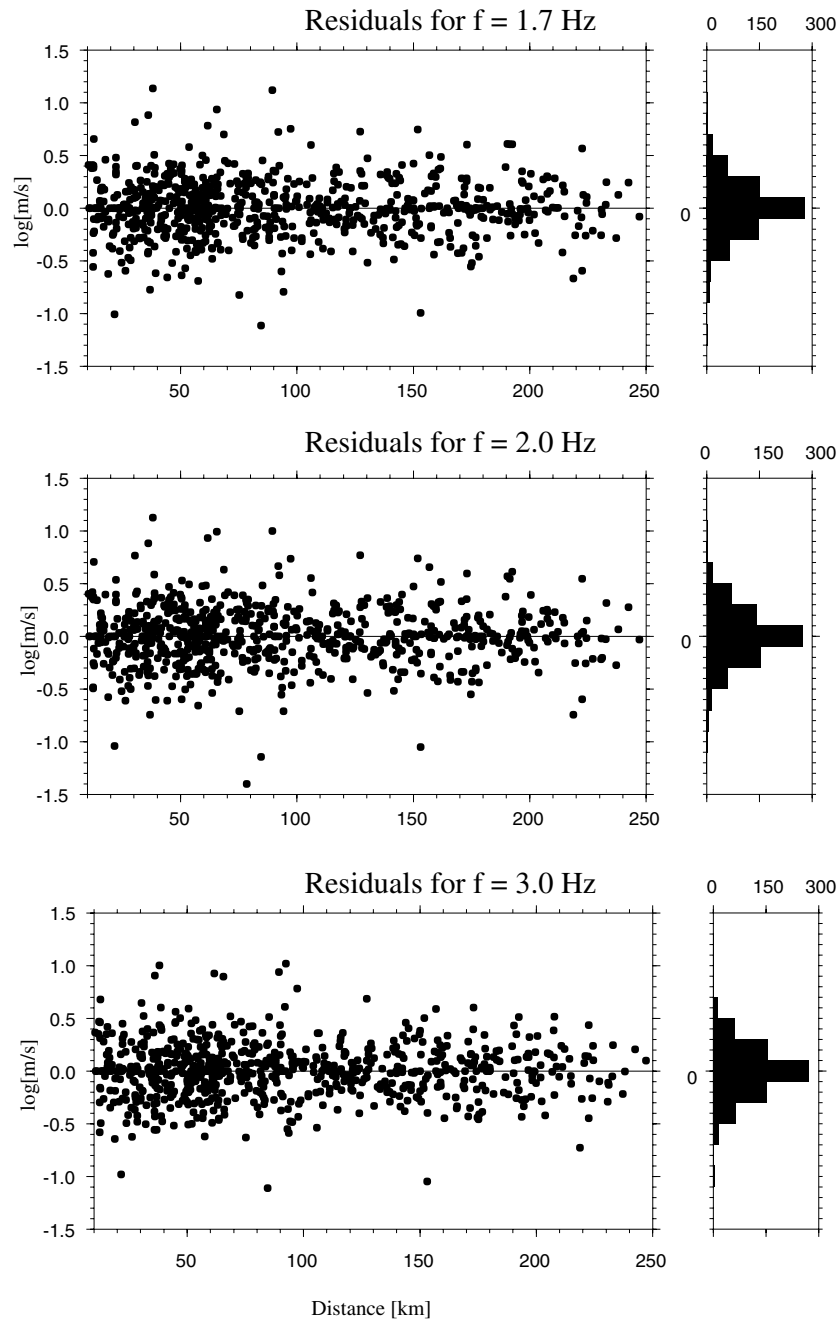
Figure 3.21: Final filtered velocity residuals at 1.7, 2.0 and 3.0 Hz. Each symbol represents one measurement, the histogram on the right indicates the number of measurements in 0.2 log units.
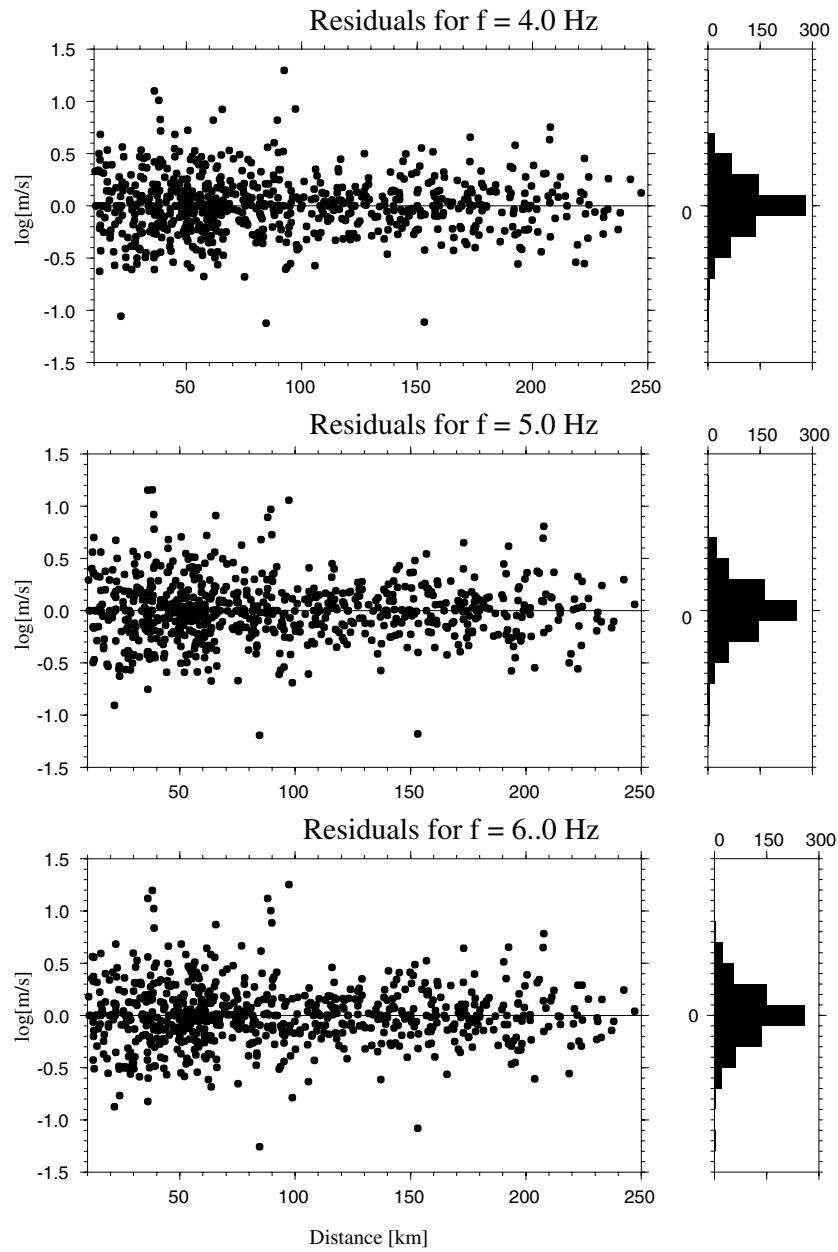
Figure 3.22: Final filtered velocity residuals at 4.0, 5.0 and 6.0 Hz. Each symbol represents one measurement, the histogram on the right indicates the number of measurements in 0.2 log units.
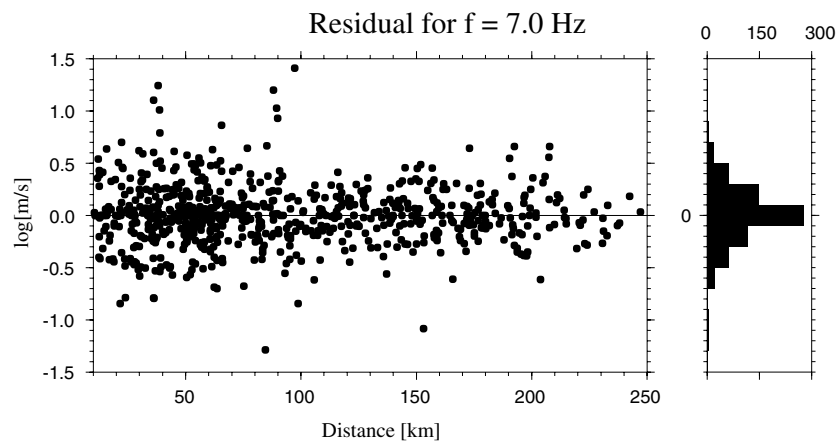
Figure 3.23: Final filtered velocity residuals at 7.0 Hz. Each symbol represents one measurement, the histogram on the right indicates the number of measurements in 0.2 log units.

Filtered Velocity Attenuation Functional									
f (Hz)	r (km)	$D(r,f)$	σ	Nobs	f (Hz)	r (km)	$D(r,f)$	σ	Nobs
0.7	10.00	0.510	0.07	16	0.8	10.00	0.450	0.08	18
0.7	20.00	0.275	0.04	48	0.8	20.00	0.224	0.05	55
0.7	40.00	0.000	0.00	59	0.8	40.00	0.000	0.00	83
0.7	60.00	-0.177	0.04	75	0.8	60.00	-0.182	0.04	86
0.7	80.00	-0.264	0.05	45	0.8	80.00	-0.249	0.05	50
0.7	100.00	-0.317	0.05	28	0.8	100.00	-0.337	0.05	35
0.7	120.00	-0.378	0.05	21	0.8	120.00	-0.418	0.05	27
0.7	140.00	-0.402	0.05	21	0.8	140.00	-0.428	0.06	25
0.7	160.00	-0.479	0.05	19	0.8	160.00	-0.506	0.06	23
0.7	180.00	-0.572	0.05	32	0.8	180.00	-0.623	0.05	36
0.7	220.00	-0.621	0.05	25	0.8	220.00	-0.685	0.06	28
0.7	250.00	-0.570	0.21	0	0.8	250.00	-0.580	0.24	0
1.2	10.00	0.387	0.08	18	1.9	10.00	0.300	0.09	18
1.2	20.00	0.201	0.05	57	1.9	20.00	0.149	0.05	60
1.2	40.00	0.000	0.00	92	1.9	40.00	0.000	0.00	100
1.2	60.00	-0.160	0.04	92	1.9	60.00	-0.145	0.04	94
1.2	80.00	-0.209	0.05	48	1.9	80.00	-0.222	0.05	44
1.2	100.00	-0.291	0.05	36	1.9	100.00	-0.327	0.06	34
1.2	120.00	-0.366	0.06	26	1.9	120.00	-0.387	0.06	25
1.2	140.00	-0.413	0.06	25	1.9	140.00	-0.469	0.06	23
1.2	160.00	-0.551	0.06	23	1.9	160.00	-0.659	0.06	21
1.2	180.00	-0.665	0.05	38	1.9	180.00	-0.758	0.06	37
1.2	220.00	-0.728	0.06	28	1.9	220.00	-0.785	0.06	26
1.2	250.00	-0.606	0.26	0	1.9	250.00	-0.558	0.27	0

Table 3.3: Attenuation functional at 0.7, 0.8, 1.2 and 1.9 Hz. The columns give values of frequency (first and sixth columns), hypocentral distance (second and seventh columns), attenuation D(r,f) at a reference distance of 40 km (third and eighth columns), associated uncertainty (fourth and nineth columns) and number of observations (fifth and tenth columns).

Filtered Velocity Attenuation Functional									
f (Hz)	r (km)	$D(r, f)$	σ	Nobs	f (Hz)	r (km)	$D(r, f)$	σ	Nobs
2.0	10.00	0.254	0.09	18	3.0	10.00	0.233	0.09	18
2.0	20.00	0.141	0.05	59	3.0	20.00	0.151	0.05	59
2.0	40.00	0.000	0.00	96	3.0	40.00	0.000	0.00	93
2.0	60.00	-0.142	0.05	90	3.0	60.00	-0.123	0.05	82
2.0	80.00	-0.227	0.06	43	3.0	80.00	-0.205	0.06	40
2.0	100.00	-0.341	0.06	30	3.0	100.00	-0.308	0.07	20
2.0	120.00	-0.419	0.06	24	3.0	120.00	-0.443	0.07	20
2.0	140.00	-0.485	0.06	21	3.0	140.00	-0.549	0.07	18
2.0	160.00	-0.663	0.07	19	3.0	160.00	-0.717	0.07	17
2.0	180.00	-0.782	0.06	32	3.0	180.00	-0.834	0.06	28
2.0	220.00	-0.832	0.07	22	3.0	220.00	-0.883	0.07	18
2.0	250.00	-0.790	0.25	0	3.0	250.00	-0.749	0.28	0
4.0	10.00	0.259	0.09	18	5.0	10.00	0.302	0.10	18
4.0	20.00	0.158	0.05	59	5.0	20.00	0.180	0.06	58
4.0	40.00	0.000	0.00	88	5.0	40.00	0.000	0.00	83
4.0	60.00	-0.107	0.05	73	5.0	60.00	-0.134	0.05	70
4.0	80.00	-0.183	0.06	37	5.0	80.00	-0.200	0.06	35
4.0	100.00	-0.279	0.07	20	5.0	100.00	-0.254	0.07	19
4.0	120.00	-0.402	0.07	17	5.0	120.00	-0.353	0.07	16
4.0	140.00	-0.491	0.07	17	5.0	140.00	-0.427	0.07	15
4.0	160.00	-0.620	0.07	16	5.0	160.00	-0.558	0.07	15
4.0	180.00	-0.708	0.07	24	5.0	180.00	-0.638	0.07	19
4.0	220.00	-0.783	0.08	14	5.0	220.00	-0.672	0.08	12
4.0	250.00	-0.787	0.29	0	5.0	250.00	-0.682	0.30	0

Table 3.4: Attenuation functional at 2 , 3 , 4 and 5 Hz. The columns give values of frequency (first and sixth columns), hypocentral distance (second and seventh columns), attenuation D(r,f) at a reference distance of 40 km (third and eighth columns), associated uncertainty (fourth and nineth columns) and number of observations (fifth and tenth columns).

Filtered Velocity Attenuation Functional									
f (Hz)	r (km)	$D(r, f)$	σ	Nobs	f (Hz)	r (km)	$D(r, f)$	σ	Nobs
6.0	10.00	0.332	0.10	17	7.0	10.00	0.349	0.10	16
6.0	20.00	0.178	0.06	56	7.0	20.00	0.168	0.06	55
6.0	40.00	0.000	0.00	71	7.0	40.00	0.000	0.00	68
6.0	60.00	-0.111	0.06	55	7.0	60.00	-0.112	0.06	51
6.0	80.00	-0.146	0.07	28	7.0	80.00	-0.136	0.07	21
6.0	100.00	-0.189	0.08	17	7.0	100.00	-0.148	0.08	13
6.0	120.00	-0.306	0.08	13	7.0	120.00	-0.247	0.08	11
6.0	140.00	-0.402	0.08	13	7.0	140.00	-0.349	0.08	12
6.0	160.00	-0.515	0.08	14	7.0	160.00	-0.501	0.08	13
6.0	180.00	-0.565	0.08	17	7.0	180.00	-0.609	0.08	15
6.0	220.00	-0.551	0.09	10	7.0	220.00	-0.569	0.10	7
6.0	250.00	-0.510	0.31	0	7.0	250.00	-0.368	0.33	0

Table 3.5: Attenuation functional at 6 and 7 Hz. The columns give values of frequency (first and sixth columns), hypocentral distance (second and seventh columns), attenuation D(r,f) at a reference distance of 40 km (third and eighth columns), associated uncertainty (fourth and nineth columns) and number of observations (fifth and tenth columns).

				Fourier Attenuation Functional				
f (Hz)	r (km)	$D(r, f)$	σ	Nobs	f (Hz)	r (km)	$D(r, f)$	σ	Nobs
0.7	10.00	0.819	0.10	16	0.8	10.00	0.945	0.10	18
0.7	20.00	0.625	0.05	48	0.8	20.00	0.582	0.05	55
0.7	40.00	0.000	0.00	59	0.8	40.00	0.000	0.00	83
0.7	60.00	-0.068	0.07	75	0.8	60.00	-0.132	0.07	86
0.7	80.00	-0.260	0.07	45	0.8	80.00	-0.343	0.07	50
0.7	100.00	-0.295	0.08	28	0.8	100.00	-0.376	0.09	35
0.7	120.00	-0.497	0.09	21	0.8	120.00	-0.616	0.09	27
0.7	140.00	-0.548	0.09	21	0.8	140.00	-0.670	0.09	25
0.7	160.00	-0.695	0.10	19	0.8	160.00	-0.838	0.10	23
0.7	180.00	-0.767	0.10	32	0.8	180.00	-0.888	0.10	36
0.7	220.00	-0.873	0.12	35	0.8	220.00	-0.997	0.12	28
0.7	250.00	-0.972	0.17	35	0.8	250.00	-1.156	0.17	6
1.2	10.00	0.973	0.11	18	1.9	10.00	1.038	0.10	18
1.2	20.00	0.576	0.05	57	1.9	20.00	0.614	0.05	60
1.2	40.00	0.000	0.00	92	1.9	40.00	0.000	0.00	100
1.2	60.00	-0.150	0.07	92	1.9	60.00	-0.124	0.06	94
1.2	80.00	-0.340	0.07	48	1.9	80.00	-0.351	0.07	44
1.2	100.00	-0.368	0.09	36	1.9	100.00	-0.396	0.08	34
1.2	120.00	-0.665	0.09	26	1.9	120.00	-0.648	0.09	35
1.2	140.00	-0.712	0.10	25	1.9	140.00	-0.709	0.09	23
1.2	160.00	-0.844	0.10	24	1.9	160.00	-0.908	0.10	21
1.2	180.00	-0.874	0.10	28	1.9	180.00	-0.834	0.10	37
1.2	220.00	-1.001	0.12	28	1.9	220.00	-1.071	0.12	26
1.2	250.00	-1.086	0.17	6	1.9	250.00	-1.177	0.16	5

Table 3.6: Fourier Attenuation functional at 0.7, 0.8, 1.2 and 1.9 Hz. The columns give values of frequency (first and sixth columns), hypocentral distance (second and seventh columns), attenuation D(r,f) at a reference distance of 40 km (third and eighth columns), associated uncertainty (fourth and nineth columns) and number of observations (fifth and tenth columns).

Fourier Attenuation Functional

f (Hz)	r (km)	$D(r, f)$	σ	Nobs	f (Hz)	r (km)	$D(r, f)$	σ	Nobs
2.0	10.00	1.016	0.10	18	3.0	10.00	1.019	0.10	18
2.0	20.00	0.584	0.05	59	3.0	20.00	0.585	0.05	59
2.0	40.00	0.000	0.00	96	3.0	40.00	0.000	0.00	93
2.0	60.00	-0.178	0.06	90	3.0	60.00	-0.188	0.06	82
2.0	80.00	-0.408	0.07	43	3.0	80.00	-0.383	0.07	40
2.0	100.00	-0.437	0.08	30	3.0	100.00	-0.443	0.08	20
2.0	120.00	-0.665	0.09	24	3.0	120.00	-0.732	0.09	20
2.0	140.00	-0.744	0.09	21	3.0	140.00	-0.907	0.09	18
2.0	160.00	-0.932	0.10	19	3.0	160.00	-1.054	0.10	17
2.0	180.00	-0.924	0.10	32	3.0	180.00	-1.121	0.10	28
2.0	220.00	-1.055	0.12	22	3.0	220.00	-1.330	0.12	18
2.0	250.00	-1.215	0.16	6	3.0	250.00	-1.442	0.16	6
4.0	10.00	1.197	0.11	18	5.0	10.00	1.290	0.12	18
4.0	20.00	0.602	0.05	59	5.0	20.00	0.596	0.06	58
4.0	40.00	0.000	0.00	88	5.0	40.00	0.000	0.00	83
4.0	60.00	-0.196	0.07	73	5.0	60.00	-0.187	0.07	70
4.0	80.00	-0.391	0.07	37	5.0	80.00	-0.399	0.08	35
4.0	100.00	-0.484	0.09	20	5.0	100.00	-0.488	0.09	19
4.0	120.00	-0.710	0.09	17	5.0	120.00	-0.712	0.10	16
4.0	140.00	-0.956	0.09	17	5.0	140.00	-0.947	0.10	15
4.0	160.00	-1.102	0.10	16	5.0	160.00	-1.008	0.11	15
4.0	180.00	-1.100	0.10	24	5.0	180.00	-1.087	0.11	19
4.0	220.00	-1.358	0.12	14	5.0	220.00	-1.376	0.14	12
4.0	250.00	-1.507	0.17	5	5.0	250.00	-1.458	0.20	5

Table 3.7: Fourier Attenuation functional at 2.0, 3.0, 4.0 and 5.0 Hz. The columns give values of frequency (first and sixth columns), hypocentral distance (second and seventh columns), attenuation D(r,f) at a reference distance of 40 km (third and eighth columns), associated uncertainty (fourth and nineth columns) and number of observations (fifth and tenth columns).

Fourier Attenuation Functional

f (Hz)	r (km)	$D(r, f)$	σ	Nobs	f (Hz)	r (km)	$D(r, f)$	σ	Nobs
6.0	10.00	1.312	0.12	17	7.0	10.00	1.425	0.11	16
6.0	20.00	0.559	0.06	56	7.0	20.00	0.547	0.06	55
6.0	40.00	0.000	0.00	71	7.0	40.00	0.000	0.00	68
6.0	60.00	-0.231	0.07	55	7.0	60.00	-0.258	0.07	51
6.0	80.00	-0.432	0.08	28	7.0	80.00	-0.451	0.08	21
6.0	100.00	-0.506	0.09	17	7.0	100.00	-0.499	0.09	13
6.0	120.00	-0.738	0.10	13	7.0	120.00	-0.795	0.10	11
6.0	140.00	-0.930	0.10	13	7.0	140.00	-0.925	0.10	12
6.0	160.00	-1.009	0.11	14	7.0	160.00	-1.109	0.11	13
6.0	180.00	-1.118	0.11	17	7.0	180.00	-1.162	0.11	7
6.0	220.00	-1.352	0.14	10	7.0	220.00	-1.414	0.14	3
6.0	250.00	-1.359	0.20	4	7.0	250.00	-1.637	0.18	0

Table 3.8: Fourier Attenuation functional at 6.0 and 7.0 Hz. The columns give values of frequency (first and sixth columns), hypocentral distance (second and seventh columns), attenuation D(r,f) at a reference distance of 40 km (third and eighth columns), associated uncertainty (fourth and nineth columns) and number of observations (fifth and tenth columns).

3.5   Duration

Duration is a function of the earthquake size and of the dispersion and scattering that elastic waves experience along source-receiver paths. A correct estimation of the ground motion duration at a specific site is very important for engineering purposes, since severe non-linear behavior is triggered in loose, water-saturated sediments at a relatively low levels of peak ground motion (down to 0.1 g), by exceeding some critical value of duration (Kramer, 1996).

An estimate of the duration of the signals as a function of distance from the source can be obtained empirically from the data. Atkinson and Boore (1995) used the duration of the time window that contained the $5\% - 95\%$ fraction of the seismic energy that follows the S-wave. Raoof et al., (1999) found results more consistent with RVT estimates by using the $5\% - 75\%$ duration definition, which is what I used, the objective of this study is to have a set of observations that permit the use of the stochastic simulation of random vibration theory as described by Boore (1983). In RVT the relation between maximum amplitudes and RMS amplitudes depends only on moments of the ground motion spectrum and the signal duration.

Tables 3.9, 3.10 and 3.11 list the duration determined using the procedure described in 2.3 for different frequencies and distances. Figure 3.24 compares the distance dependence of duration for the different frequencies showing that low frequency signal components have longer duration than high-frequency components. Similar results have been observed in Southern California (Raoof et al., 1999), but for other regions as the case of Utah (Jeon, 2000) this tendency of decreasing duration with increasing
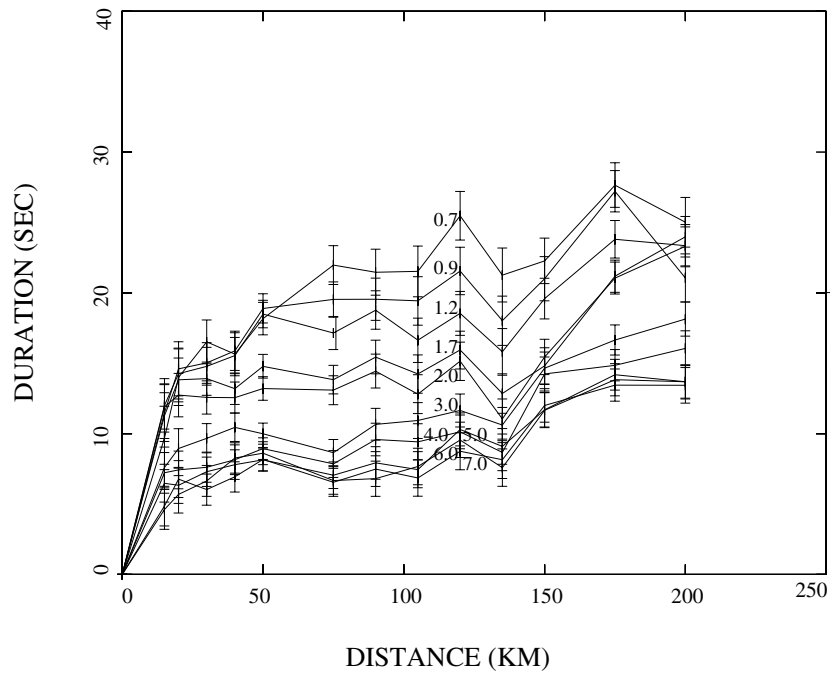
Figure 3.24: Distance dependence of duration for filtered data at the different frequencies. Each curve is a linear regression from the observed durations.

frequencies was not observed.

The rapid increase of duration at distances less than 20 km explains part of the differences in the time and frequency domain $D(r)$ shown in Figure 3.19. A duration increasing with distance makes time domain peaks decay more rapidly with distance than the Fourier velocity spectra. The relative distance in dependence of duration at larger distances means that both $D(r)$'s will be similar. The strong frequency dependence $f < 3$ Hz may be due to low frequency waves within the 3-D shallow structure of the region.

Figure 3.25 show a tendency for scatter in residual durations to increase with distance. For low frequencies scattering is higher than at higher frequencies.
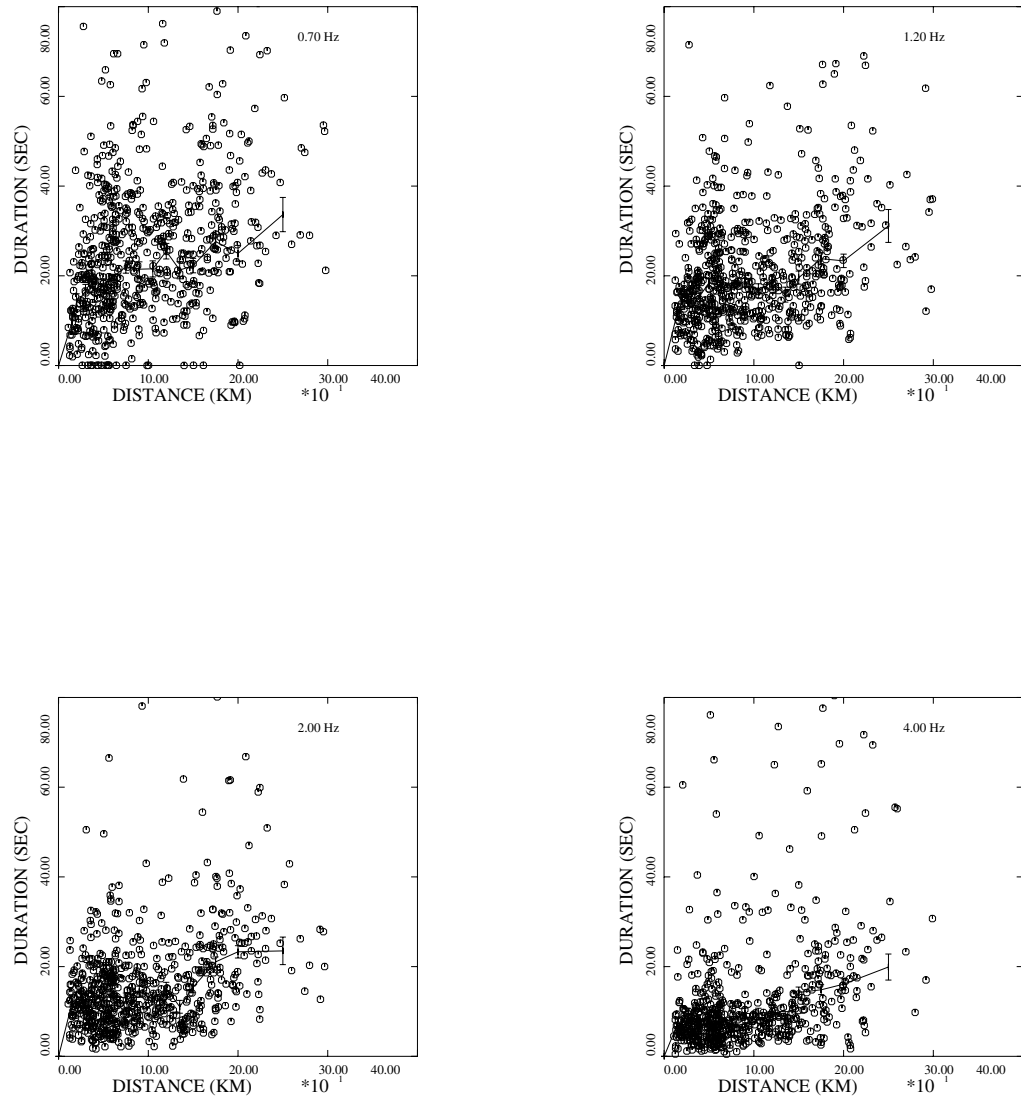
Figure 3.25: Duration data and regression lines as a function of distance for filter frequencies of 0.7, 1.2, 2.0 and 4.0 Hz.
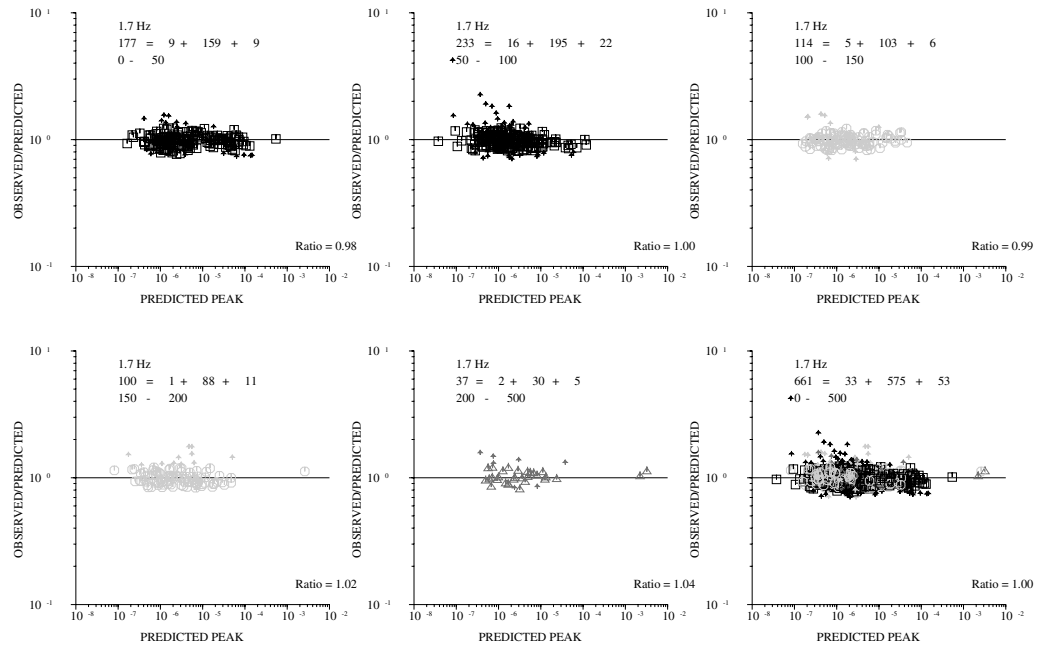
Figure 3.26: Comparison of observed to predicted peak amplitudes as a function of predicted peaks for filtered frequency at 1.7 Hz. Each figure represent a different distance range. The total number of observation is separated in the 0-5%, 5-95% or 95%-100% bounds of the predicted peak. The distance range and the geometric mean ratio is plotted.

In figures 3.26 and 3.27 is compared the ratio of observed peak values to those predicted by RVT using the measured duration. If RVT is appropriate and if the duration is properly defined, then most of the observations should be within the bounds 5-95% of the predicted peak. For example at 1.7 Hz, 575 of 661 (86 %) are in the second bin. The duration definition is good when the ratio between the observed and predicted peak motion is 1.0 and the distribution of peak is centered. This comparison justifies our definition of duration. At high frequencies there are small problems with small events recorded at short distances, which indicates the importance of using high signal to noise ratio data.
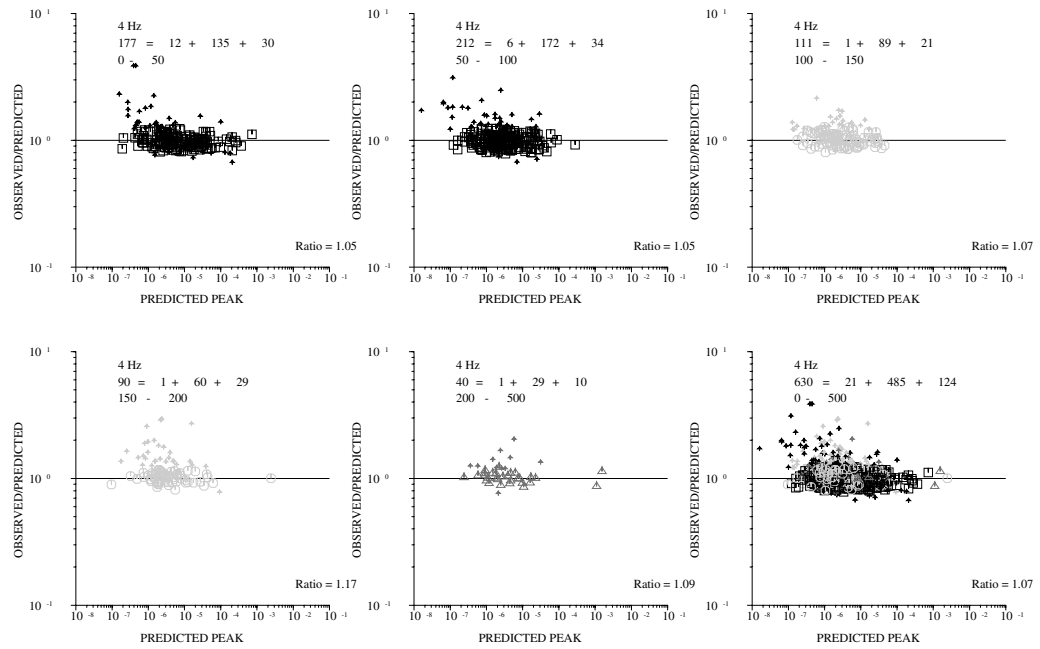
Figure 3.27: Comparison of observed to predicted peak amplitudes as a function of predicted peaks for filtered frequency at 4.0 Hz. Each figure represent a different distance range. The total number of observation is separated in the 0-5%, 5-95% or 95%-100% bounds of the predicted peak. The distance range and the geometric mean ratio is plotted.

Duration Term for central Mexico									
f (Hz)	r (km)	Dur	σ	Nobs	f (Hz)	r (km)	Dur	σ	Nobs
0.7	0.00	0.00	0.01	1	0.9	0.00	0.00	0.01	1
0.7	15.00	9.70	2.24	15	0.9	15.00	11.49	2.04	16
0.7	20.00	14.01	2.00	23	0.9	20.00	14.60	1.92	23
0.7	30.00	16.52	1.55	44	0.9	30.00	15.02	1.44	48
0.7	40.00	15.64	1.53	45	0.9	40.00	15.89	1.39	51
0.7	50.00	18.17	1.15	87	0.9	50.00	18.90	1.03	100
0.7	75.00	21.98	1.38	67	0.9	75.00	19.53	1.25	76
0.7	90.00	21.47	1.63	36	0.9	90.00	19.56	1.50	40
0.7	105.00	21.52	1.79	30	0.9	105.00	19.43	1.72	29
0.7	120.00	25.48	1.72	33	0.9	120.00	21.56	1.68	31
0.7	135.00	21.26	1.92	27	0.9	135.00	18.02	1.75	30
0.7	150.00	22.25	1.61	39	0.9	150.00	20.98	1.57	38
0.7	175.00	27.73	1.58	40	0.9	175.00	27.29	1.47	42
0.7	200.00	25.53	1.72	32	0.9	200.00	21.50	1.67	30
0.7	250.00	30.47	2.84	10	0.9	250.00	28.89	2.69	10
1.2	0.00	0.00	0.01	1	1.7	0.00	0.00	0.01	1
1.2	15.00	12.01	1.90	18	1.7	15.00	11.28	1.63	18
1.2	20.00	14.27	1.81	24	1.7	20.00	13.82	1.56	25
1.2	30.00	14.78	1.34	51	1.7	30.00	13.90	1.18	49
1.2	40.00	15.55	1.29	55	1.7	40.00	13.19	1.12	55
1.2	50.00	18.50	0.98	103	1.7	50.00	14.79	0.84	109
1.2	75.00	17.15	1.18	81	1.7	75.00	13.84	1.02	83
1.2	90.00	18.78	1.37	46	1.7	90.00	15.44	1.20	45
1.2	105.00	16.64	1.57	33	1.7	105.00	14.23	1.37	34
1.2	120.00	18.54	1.56	33	1.7	120.00	15.94	1.35	34
1.2	135.00	15.81	1.66	30	1.7	135.00	12.85	1.42	32
1.2	150.00	19.58	1.45	42	1.7	150.00	14.82	1.30	41
1.2	175.00	23.83	1.33	48	1.7	175.00	21.17	1.15	49
1.2	200.00	23.64	1.48	35	1.7	200.00	23.97	1.41	30
1.2	250.00	29.49	2.41	11	1.7	250.00	25.36	2.24	10

Table 3.9: Duration at 0.7, 0.9, 1.2 and 1.7 Hz. The columns give values of frequency (first and sixth columns), hypocentral distance (second and seventh columns), duration between 5(third and eighth columns), associated error bar (fourth and nineth columns) and number of observations (fifth and tenth columns).

Duration Term for central Mexico									
f (Hz)	r (km)	Dur	σ	Nobs	f (Hz)	r (km)	Dur	σ	Nobs
2.0	0.00	0.00	0.01	1	3.0	0.00	0.00	0.01	1
2.0	15.00	11.90	1.59	20	3.0	15.00	7.59	1.47	18
2.0	20.00	12.74	1.55	25	3.0	20.00	8.94	1.42	24
2.0	30.00	12.57	1.18	50	3.0	30.00	9.66	1.05	47
2.0	40.00	12.57	1.11	57	3.0	40.00	10.49	1.02	50
2.0	50.00	13.21	0.84	111	3.0	50.00	10.21	0.76	105
2.0	75.00	13.09	1.03	84	3.0	75.00	8.57	0.94	77
2.0	90.00	14.44	1.21	44	3.0	90.00	10.67	1.14	37
2.0	105.00	12.81	1.39	34	3.0	105.00	10.94	1.28	29
2.0	120.00	15.14	1.36	34	3.0	120.00	11.64	1.18	35
2.0	135.00	11.04	1.43	31	3.0	135.00	10.62	1.26	31
2.0	150.00	15.45	1.26	42	3.0	150.00	14.65	1.17	38
2.0	175.00	21.01	1.14	49	3.0	175.00	16.60	1.08	42
2.0	200.00	23.32	1.34	33	3.0	200.00	18.12	1.18	32
2.0	250.00	25.16	2.02	14	3.0	250.00	23.80	1.83	13
4.0	0.00	0.00	0.01	1	5.0	0.00	0.00	0.01	2
4.0	15.00	7.22	1.45	19	5.0	15.00	6.48	1.36	21
4.0	20.00	7.42	1.35	27	5.0	20.00	6.33	1.29	28
4.0	30.00	7.62	1.07	47	5.0	30.00	7.29	1.06	47
4.0	40.00	8.16	1.06	48	5.0	40.00	7.81	1.06	45
4.0	50.00	9.01	0.77	103	5.0	50.00	8.20	0.78	94
4.0	75.00	7.82	0.95	75	5.0	75.00	7.03	0.96	70
4.0	90.00	9.58	1.16	36	5.0	90.00	7.92	1.17	34
4.0	105.00	9.42	1.30	29	5.0	105.00	7.44	1.30	28
4.0	120.00	10.12	1.21	34	5.0	120.00	10.30	1.19	33
4.0	135.00	8.68	1.30	29	5.0	135.00	9.10	1.29	28
4.0	150.00	14.24	1.22	35	5.0	150.00	11.71	1.25	31
4.0	175.00	14.84	1.12	39	5.0	175.00	14.09	1.11	37
4.0	200.00	16.10	1.20	33	5.0	200.00	13.51	1.16	33
4.0	250.00	20.65	2.04	11	5.0	250.00	18.77	2.06	9

Table 3.10: Duration at 2, 3, 4 and 5 Hz. The columns give values of frequency (first and sixth columns), hypocentral distance (second and seventh columns), duration between 5(third and eighth columns), associated error bar (fourth and nineth columns) and number of observations (fifth and tenth columns).

Duration Term for central Mexico									
f (Hz)	r (km)	Dur	σ	Nobs	f (Hz)	r (km)	Dur	σ	Nobs
6.0	0.00	0.00	0.01	2	7.0	0.00	0.00	0.01	2
6.0	15.00	4.62	1.42	20	7.0	15.00	4.86	1.41	20
6.0	20.00	5.69	1.33	27	7.0	20.00	6.77	1.31	27
6.0	30.00	6.64	1.10	45	7.0	30.00	6.02	1.10	44
6.0	40.00	8.27	1.08	44	7.0	40.00	6.93	1.08	43
6.0	50.00	8.61	0.82	87	7.0	50.00	8.18	0.84	79
6.0	75.00	6.68	0.98	68	7.0	75.00	6.55	0.99	64
6.0	90.00	6.81	1.25	30	7.0	90.00	7.49	1.24	30
6.0	105.00	7.67	1.30	27	7.0	105.00	6.86	1.30	27
6.0	120.00	9.56	1.26	30	7.0	120.00	8.75	1.31	27
6.0	135.00	7.59	1.33	27	7.0	135.00	8.16	1.34	25
6.0	150.00	11.66	1.24	32	7.0	150.00	12.00	1.19	34
6.0	175.00	13.85	1.15	37	7.0	175.00	13.48	1.14	37
6.0	200.00	13.72	1.18	33	7.0	200.00	13.56	1.23	29
6.0	250.00	16.45	2.23	8	7.0	250.00	19.11	2.17	8

Table 3.11: Duration at 6 and 7 Hz. The columns give values of frequency (first and sixth columns), hypocentral distance (second and seventh columns), duration between 5(third and eighth columns), associated error bar (fourth and nineth columns) and number of observations (fifth and tenth columns).

3.6   Parameterization of the Propagation Term

I parameterize the geometrical spreading and attenuation functions to create a theoretical Fourier velocity spectra of the propagation term. Although the most important results of this work are listed in tables 3.3 - 3.11. I now translate those values into a more compact representation suitable for engineering and hazard applications. I model the results in terms of a simple function of geometric spreading and a frequency dependent seismic attenuation. The simplified parameterization can not match the observed attenuation curves perfectly and interpretation of the parameters in terms of geology is a difficult exercise that I avoid.

The parameterization of $D(r)$ consists of applying (2.3), solving the forward modeling using RVT and comparing to the prediction with the empirical regression estimates. It is important to note that many of the parameters of the propagation functional trade off each other. Specifically the geometrical spreading trades off with the attenuation function $Q(f)$.

The equation

$$D(r, f) = log\left(g(r)exp\left[-\frac{\pi f R}{\beta Q_o f^\eta}\right]\right) \qquad (3.4)$$

is solved using forward modeling described in section 2.6. In any modeling exercise we must choose a measure of misfit that can be used to favor one set of model parameters over another. In our case we cannot match the complexity of the attenuation relations perfectly. I found a geometrical spreading of

$$g(r) = \begin{cases} r^{-1.3} & r \leq 40\,km \\ r^{-0.5} & r \geq 40\,km \end{cases} \qquad (3.5)$$

and an attenuation functional

$$Q(f) = 88 \ f^{0.73} \tag{3.6}$$

I used a shear wave average velocity β of 3.5 km/s.

The functional form of the distance term may be expressed in different ways. I choose the simplest form for represent the propagation term. The cross-over distance of 40 km in the equation 3.5 is related to the thickness of the crust and the super critical incidence of shear waves reflecting off the Moho. The geometrical spreading at distances shorter than the cross-over distance is related to the propagation of body waves and usually is assumed to be r^{-1}. The faster decay of $r^{-1.3}$ observed at short distances is not completely understood, it may be caused by steep gradients in the velocity structure and uncertainties on the depth estimation. For longer distances the geometrical spreading for surface waves, $r^{-0.5}$, describes the propagation. I tried many different cross-over distances including trilinear geometrical spreading, with nodes between the 40 and 100 km but the observations fit better with the one already presented in 3.5 and 3.6.

The cross-over distance is a physical property of the crust and is not related to the reference distance r_{ref} needed to apply the constraints on the algebraic problem. The reference distance has a more subjective interpretation and is only used as a mathematical tool for solving the problem. In this study the cross-over distance and the reference distance just happen to equal 40 km, but they can have different values in other regions.

The attenuation functional $Q(f) = Q_o \ f^\eta$ trades off with the geometrical spreading. The frequency dependent exponent, η, controls the separation between the different frequencies in the propagation functional; when

$\eta = 0$, Q is constant but, the attenuation at different frequencies differs, low frequencies attenuate slower than high frequencies. When $\eta = 1$, $Q(f)$ is frequency dependent, but the attenuation at different frequencies is the same. This tradeoff of the attenuation operator and geometrical spreading can be reduced if data are available at larger distances and higher frequencies.

The synthetic estimates of the attenuation functional were computed using the RVT. In figures 3.28 and 3.29 I compare the attenuation functional $D(r,f)$ for peak filtered time domain and the Fourier amplitude respectively. At short distances ($r < 40$ km) the fast decay is modeled by a geometrical spreading of $g(r) = r^{-1.3}$ but it seems that a smaller frequency dependent η is needed. Apparently a simple attenuation model at all frequencies and distances cannot match the complete propagation functional. One explanation may be the mixed data set, short distance data are basically generated by shallow events usually on faults within the Basin of México; the large distance data are a mixture between regional and deep earthquakes with different propagation paths. It is important to recall that all parameters modeled trade off with each other. Specifically, the shape of the geometrical spreading function (the slope of each linear segment) trades off with the attenuation parameter $Q(f) = Q_o f^\eta$. The trade off is mostly concentrated on Q_o, since the sensitivity of the attenuation functional on the parameter η is usually very high.

In order to have a more quantitative measurement of the error of the parameterization, a grid search made through the parameter space was

Figure 3.28: Attenuation functional $D(r, f)$ obtained from the regression of the filtered velocities at the frequencies of 0.7, 0.9, 1.2, 1.7, 2.0, 3.0, 4.0, 5.0, 6.0 and 7.0. Gray (or color) tones represent the final regression, the black lines in the background describe the theoretical prediction. The reference hypocentral distance is at 40 km.
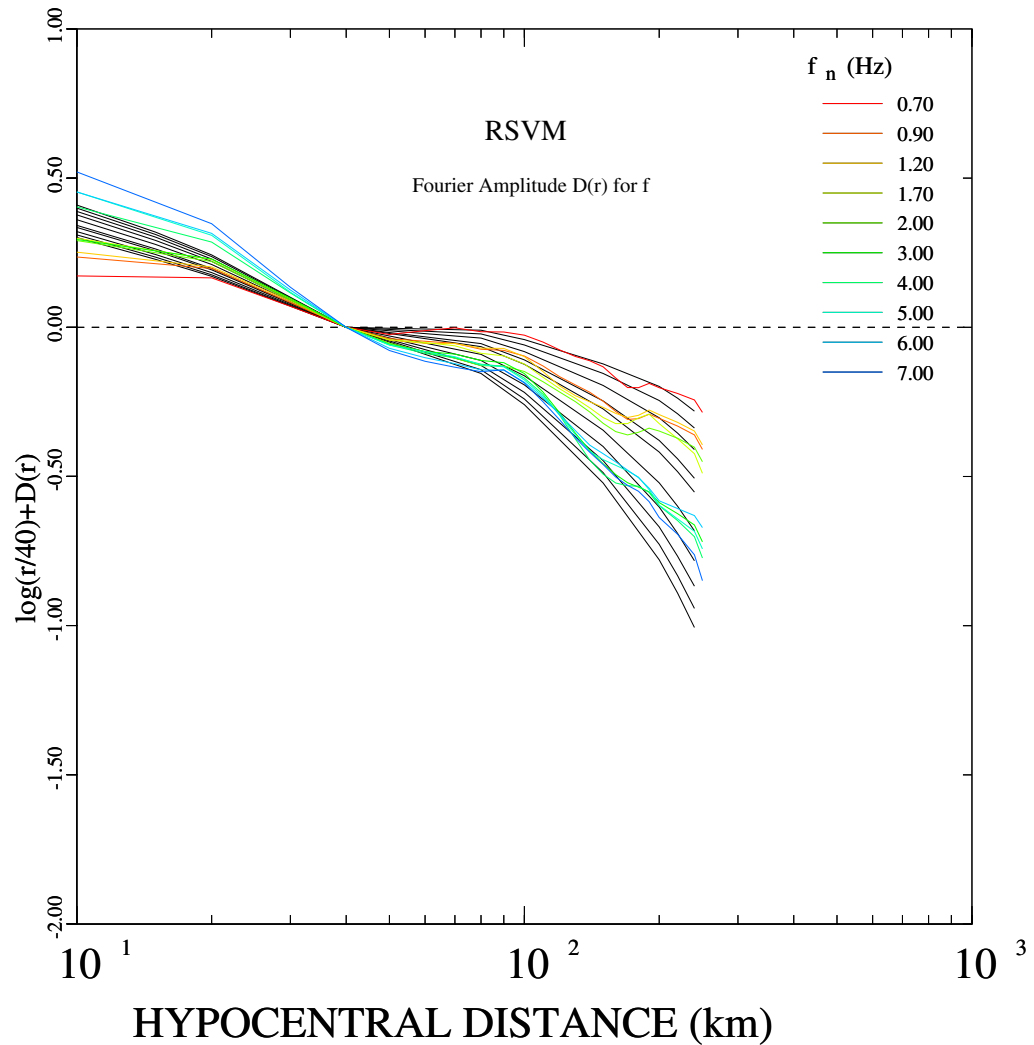
Figure 3.29: Attenuation functional $D(r, f)$ obtained from the regression of the Fourier amplitudes at the frequencies of 0.7, 0.9, 1.2, 1.7, 2.0, 3.0, 4.0, 5.0, 6.0 and 7.0. Gray (or color) tones represent the final regression, the black lines in the background describe the theoretical prediction. The reference hypocentral distance is at 40 km.

performed. I minimized the following function

$$E = \frac{\sum_i \left(D_{iobs} - D_{ipred}/\sigma_i^2\right)^2}{\sum_i \left(1/\sigma_i\right)^2} \tag{3.7}$$

Where D_{iobs} is the propagation function resulting from the regression and D_{ipred} is the one from the RVT, the σ_i are the standard deviation resulting from the regression. Table 3.12 show the errors from different parameters. The values of Q_o tested ranged from 50 to 200, and η from 0.4 to 0.8, the geometrical spreading was fixed to $g(r) = r^{-1.3}$ for $r < 40$ km and $g(r) = r^{-0.5}$ for $r > 40$ km. A minimum error does not reflect entirely the best approximation of the propagation functional, sometimes a minimum error reflects the departure of the observed to the predicted in a general sense, and a visual inspection of the minimum errors is always performed. At large distances the observed propagation functional is more stable, and is easier to model by equation (3.4), for this reason, the minimum error model fits better at large distances, but in the distance range from 40 - 100 km we prefer to model the propagation functional because we have more observations. From Table 3.12 the minimum at $Q_o = 90$ and $\eta = 0.80$ is close to the parameters chosen as the best fit model ($Q_o = 88$, $\eta = 0.73$), the next minimum at $Q_o = 100$ and $\eta = 0.80$ is shown in Figure 3.30, where we observe a poor fit for $R < 40$ km, values of Q_o higher than 100 significantly degrade the fit, even though they can have lower errors. This apparent failure of (3.7) is due to the fact that these are many more observations for $R > 40$ km than for $R < 40$ km.

The non-uniqueness of the solution, and the trade-off between the geometrical spreading and $Q(f)$ is illustrated by estimating a second model with a larger cross over distance at 180 km. I considered that the best

Parameterization errors

Q_o	η	E	$\sqrt{E}$	Q_o	η	E	$\sqrt{E}$
50	0.40	0.827	0.909	100	0.40	0.320	0.566
50	0.50	0.716	0.846	100	0.50	0.293	0.542
50	0.60	0.620	0.787	100	0.60	0.273	0.523
50	0.70	0.540	0.734	100	0.70	0.259	0.509
50	0.80	0.475	0.689	100	0.80	0.250	0.500
60	0.40	0.612	0.782	120	0.40	0.279	0.529
60	0.50	0.532	0.729	120	0.50	0.263	0.513
60	0.60	0.465	0.682	120	0.60	0.251	0.501
60	0.70	0.411	0.641	120	0.70	0.243	0.493
60	0.80	0.370	0.608	120	0.80	0.259	0.509
70	0.40	0.485	0.697	140	0.40	0.259	0.509
70	0.50	0.426	0.653	140	0.50	0.250	0.500
70	0.60	0.378	0.615	140	0.60	0.242	0.491
70	0.70	0.341	0.584	140	0.70	0.238	0.488
70	0.80	0.313	0.559	140	0.80	0.236	0.486
80	0.40	0.407	0.637	180	0.40	0.243	0.493
80	0.50	0.362	0.601	180	0.50	0.239	0.489
80	0.60	0.326	0.571	180	0.60	0.237	0.487
80	0.70	0.300	0.547	180	0.70	0.238	0.487
80	0.80	0.280	0.530	180	0.80	0.239	0.489
90	0.40	0.355	0.596	200	0.40	0.241	0.491
90	0.50	0.321	0.566	200	0.50	0.239	0.488
90	0.60	0.294	0.542	200	0.60	0.238	0.488
90	0.70	0.275	0.524	200	0.70	0.239	0.489
90	0.80	0.261	0.511	200	0.80	0.241	0.491

Table 3.12: Errors for different propagation function parameters. First and fifth columns Q_o, second and sixth columns η, third and and seventh columns E, fourth and eight columns $\sqrt{E}$. The geometrical spreading is fixed to $g(r) = r^{1.3}$ for $r < 40$ km, and $g(r) = r^{0.5}$ for $r > 40$ km. Three different minima are shown.
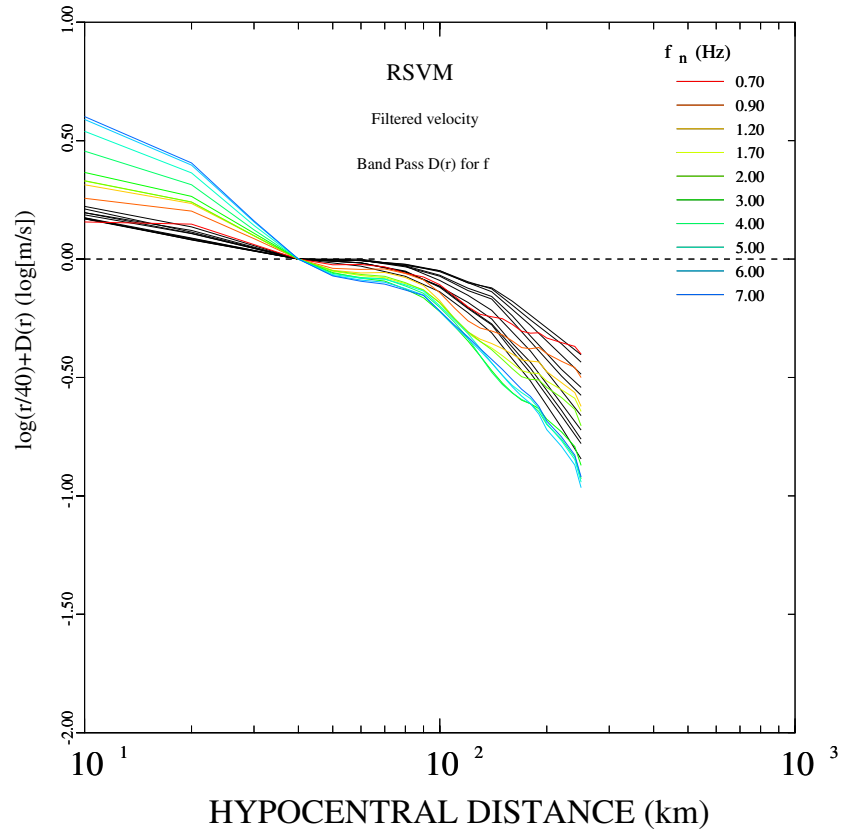
Figure 3.30: Filtered velocity attenuation functional $D(r, f)$ for $Q_o = 100$ and $\eta = 0.80$. Gray tones represent the final regression, the black lines in the background describe the theoretical prediction. The reference hypocentral distance is at 40 km. The theoretical estimates are overpredicted between 40-180 km.

model is

$$Q(f) = 220 f^{0.66} \tag{3.8}$$

and a geometrical spreading of

$$g(r) = \begin{cases} r^{-1.0} & r \leq 180\,km \\ r^{-0.5} & r \geq 180\,km \end{cases} \tag{3.9}$$

Figure 3.31 compares both models: Model 1 - $Q_o = 88$ and $\eta = 0.73$, $g(r) = r^{1.0}$ for $r < 40$ km, and $g(r) = r^{0.5}$ for $r > 40$ km. Model 2 - $Q_o = 220$ and $\eta = 0.66$, $g(r) = r^{1.0}$ for $r < 180$ km, and $g(r) = r^{0.5}$ for $r > 180$ km. I observe that the two models fit the the observed propagation term, Model 1 seems to be more appropriate for short distances (40 - 180 km) while Model 2 is more suitable for large distances (> 180 km), this model is similar to the attenuation function estimated by Ordaz and Singh (1992) for the Guerrero coast. An interesting observation is that the two different models, while different in appearance, reflect in a similar way, the same propagation functional. Thus, caution should be taken when we compare different models considering only the values of Q_o or η, without taking into account the expression of the geometrical spreading. Two different values of Q_o, such as 88 and 220, that may be considered significantly different are in fact in better correspondence than other values similar in magnitude, but with different expression of the geometrical spreading.

3.7   Depth Dependence

To estimate the depth dependence of our results, I performed a general regression using only 566 seismograms generated by 169 shallow events (depth $\leq 15\,km$). I choose the depth of 15 km because at this depth I had
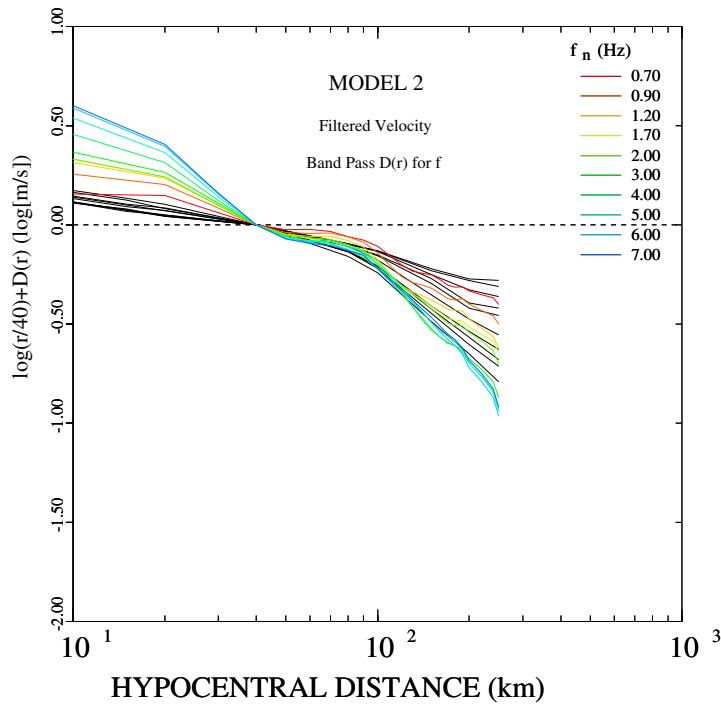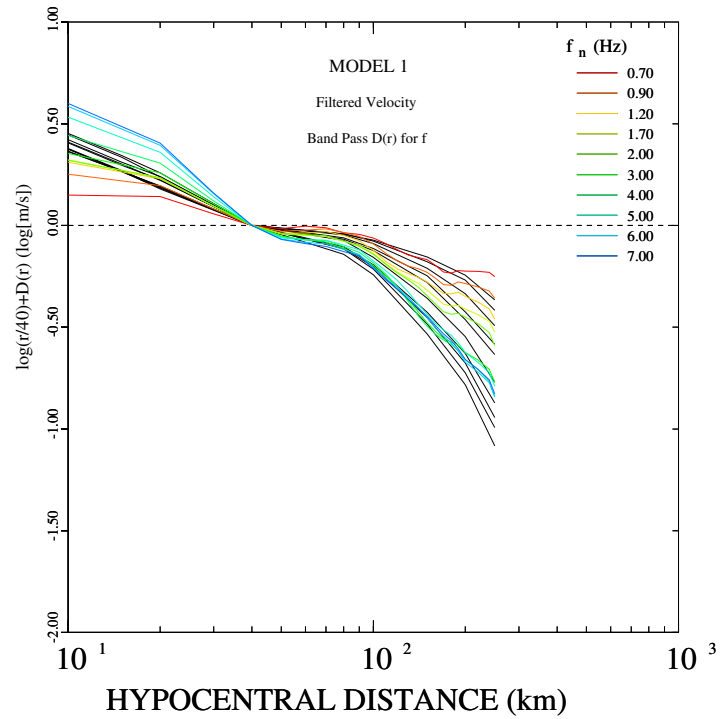
Figure 3.31: Comparison between the two models. Model 1: $Q_o = 88$ and $\eta = 0.73$, $g(r) = r^{1.0}$ for $r < 40$ km, and $g(r) = r^{0.5}$ for $r > 40km$. Model 2: $Q_o = 200$ and $\eta = 0.66$, $g(r) = r^{1.0}$ for $r < 180$ km, and $g(r) = r^{0.5}$ for $r > 180$ km

enough data to perform a regression. Figure 3.32 shows the comparison between the attenuation functions computed using coda normalization for shallow events and the peak-motion regression. The coda normalization again fails especially for short distances. Part of the reason may due to the lack of azimuthal coverage on the focal sphere. Figure 3.33 compares the attenuation functionals $D(R,f)$ for the shallow events to those predicted using Model 1 for the complete data set. The shallow events seem to agree to the predictive model proposed for the entire data set. However they do not constrain the large distance spreading.

To consider possible variation with source depth in México, I also compared the functional $D(r)$ from the complete data set to the one using only shallow events for each single frequency. As seen from Figure 3.34 the attenuation from the entire data set (solid triangles) does not differ significantly from the shallow events (depth $\leq 15\ km$). I should note that focal depth estimations of shallow events in central México is uncertain, due to an inadequate seismic station coverage. Thus a more detailed study on the depth dependence was not possible.

Of particular importance are the intermediate-depth earthquakes in central México. Due to the paucity of earthquakes of this type of earthquake, we could not perform a regression analysis using only these events. The complete data set consists of 72 events deeper than 45 km. The attenuation functional from the regression of the entire data is the average of shallow and deep earthquakes, we expect that shallow and deep events may have significative differences especially at short distances, since they travel different paths. In future research the depth dependence of the propagation functional should be performed in detail as more data are
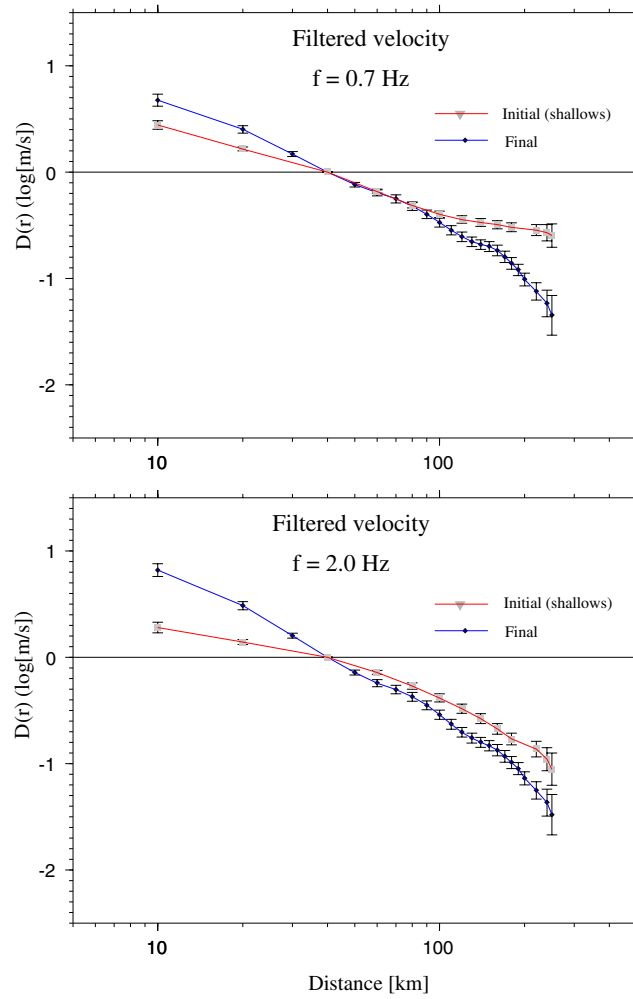
Figure 3.32: Comparison between the attenuation functions computed using coda normalization for shallow events (depth less than 15 km) and the peak-motion regression.
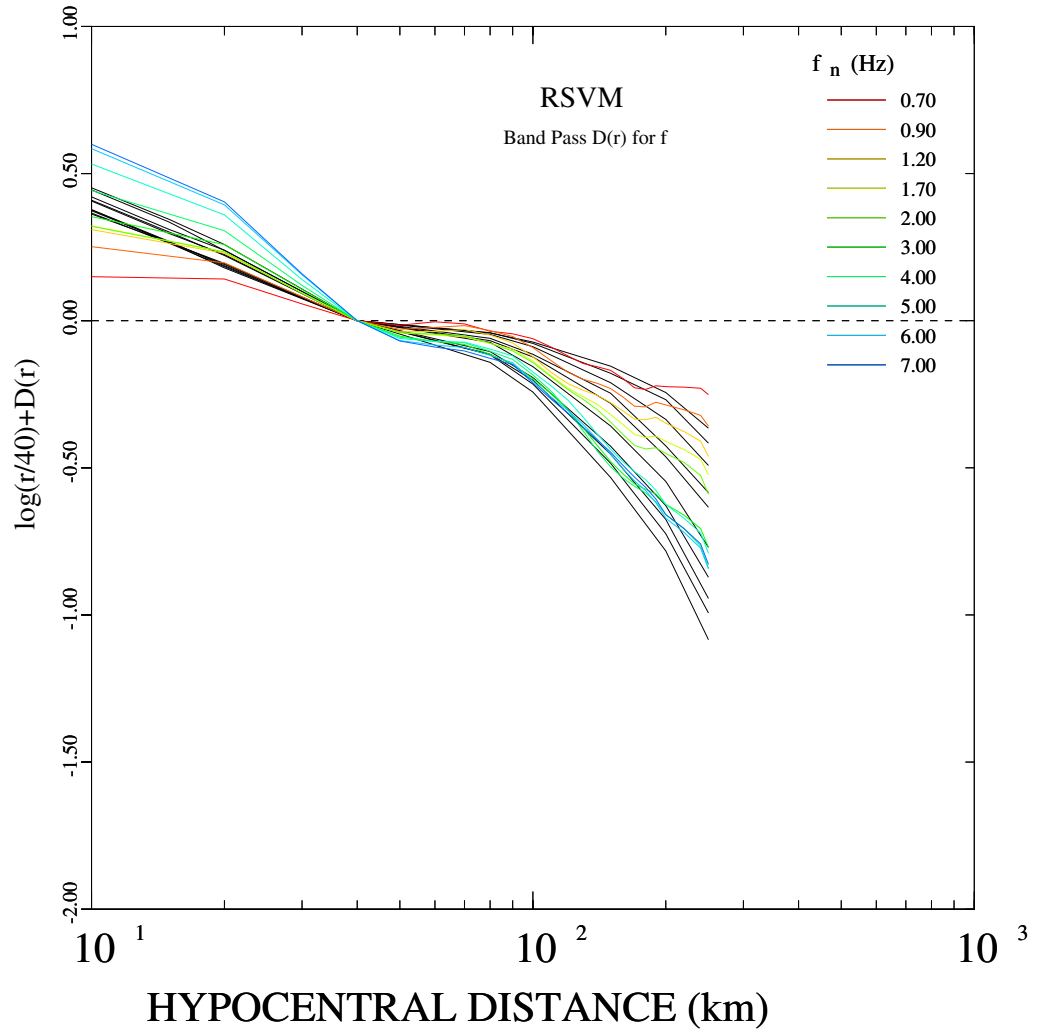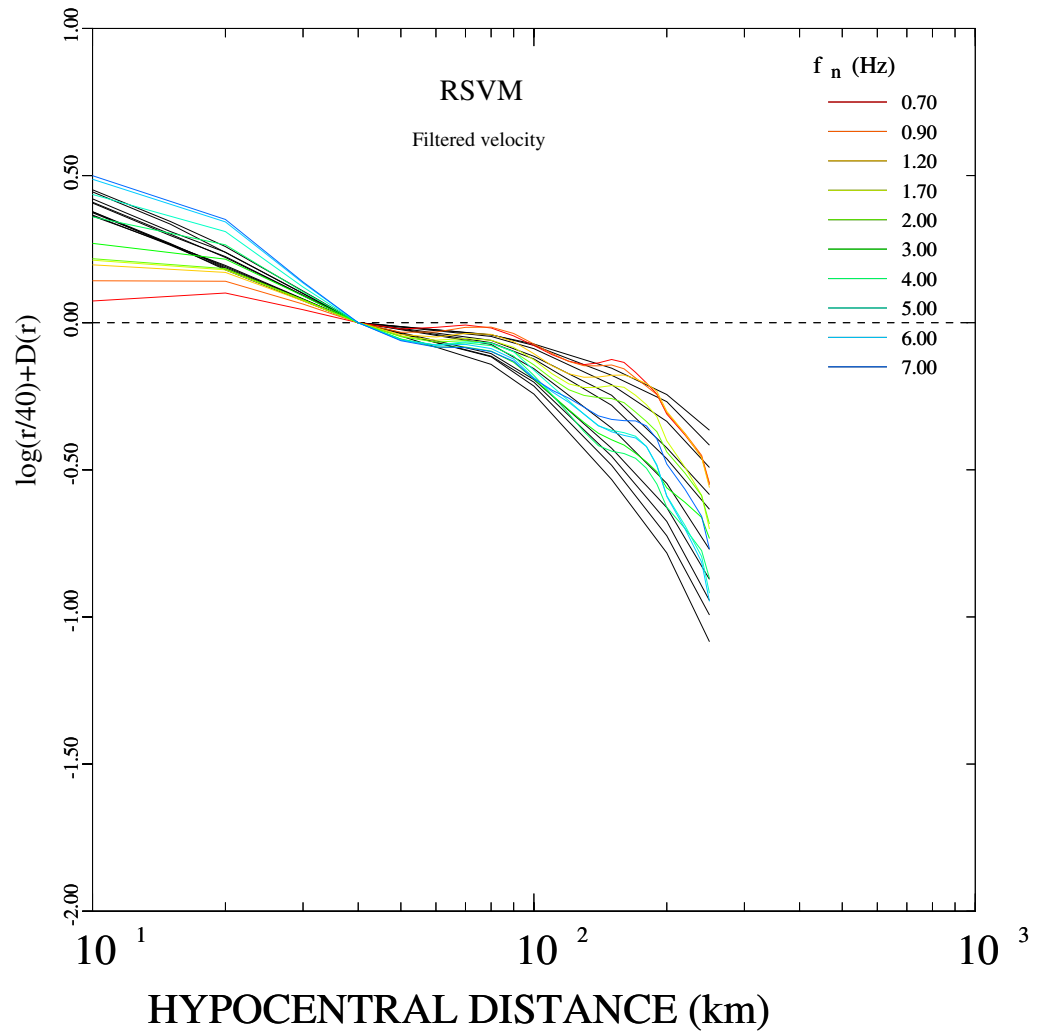
Figure 3.33: Attenuation functional *D(r,f)* for shallow events obtained from the regression of the filtered velocities at the frequencies of 0.7, 0.9, 1.2, 1.7, 2.0, 3.0, 4.0, 5.0, 6.0 and 7.0. Gray tones represent the final regression, the black lines in the background describe the theoretical prediction. The reference hypocentral distance is at 40 km.
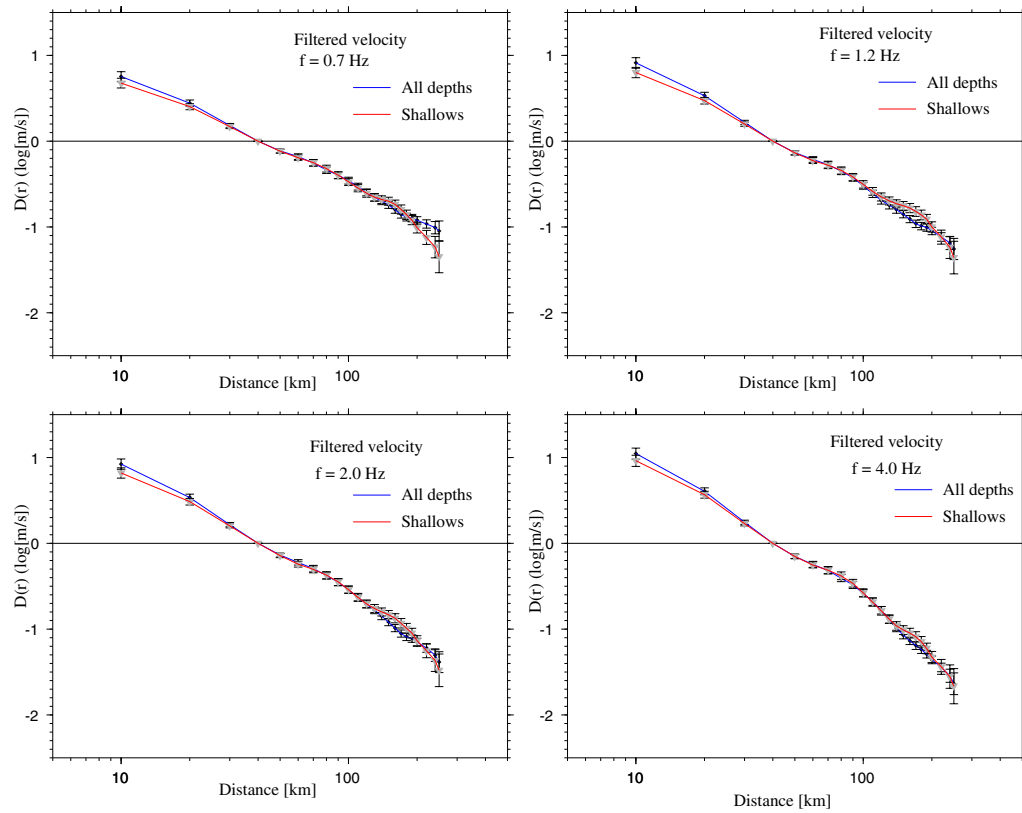
Figure 3.34: Comparison between the attenuation functional from the general regression (black) and the one from the shallow events (gray) at 0.7, 1.2, 2.0 and 4.0 Hz.
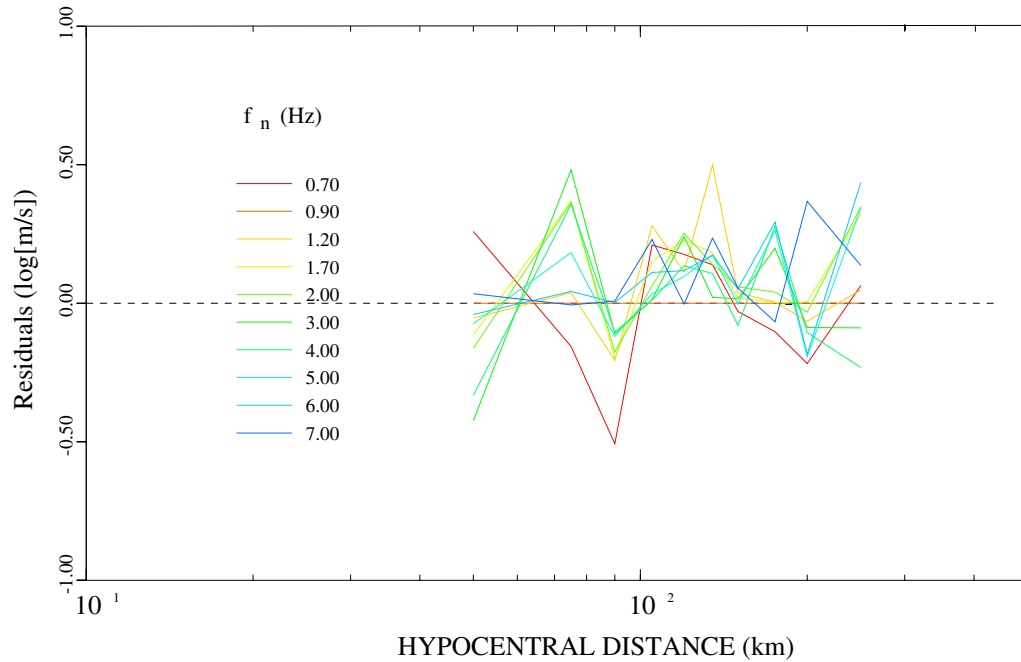
Figure 3.35: Residuals for deep events. (events greater than 45 km).

available.

When there are not enough data, a common practice for studying possible differences is through observation of residuals. Figure 3.35 shows the residuals of the regression for only these deep earthquakes. To do this I selected the residuals as shown in Figure 3.13 and then determined piecewise linear trend by least squares. The general trend of the propagation functional agrees with the complete data set. However a slight bias to the positive side is observed, especially at longer distances ($>$80 km). The residual is defined as

$$Residual = log(Amp) - D(R) - Site - Excitation \qquad (3.10)$$

note that when the $log(Amp) = D(R) + Site + Excitation$ then the residual is zero. Since the most obvious difference between the deep and shallow events is the propagation path, we may attribute this discrepancy to a un-

derestimation of the propagation term. Yamamoto et al. (1997) observed similar characteristics on the variation of attenuation with depth, having observed a slightly decrease of attenuation as increasing depth. Another explanation could be that the excitation level varies with depth; this case will be discussed in more detail in the next chapter.

3.8   Site Effects on Earthquake Ground Motion

It has been long recognized that site effects can affect the nature of strong ground motion (Sanchez-Sesma, 1987). Many factors, including topographic heterogeneities, local amplification in sedimentary basins and geological irregularities, are strongly related to the site effects of the earthquake ground motions. (eg. Esquivel and Sanchez-Sesma, 1980; Ruiz and Esteva, 1981; Trifunac and Hudson,1971; Griffiths and Bollinger, 1979).

Although recent work has emphasized the physical understanding of site effects in a more quantitative manner (Boore and Joyner, 1997), there is still a lack of criteria for dealing with the problem while taking into account source, path and local conditions. Active research is needed to predict more accurately the local effects given the source parameters. Much of the research in this field is concentrated on the understanding of wave propagation and source dynamics (Sanchez-Sesma, 1987). Site effects are present in this study in a network average (Figure 3.36).

The Fourier velocity spectra for a frequency f and a distance r is

$$A(f) = S(f) \times g(r) \times exp\left[\frac{-\pi f r}{\beta Q(f)}\right] \times exp\left[-\pi \kappa f\right] \times V(f) \qquad (3.11)$$

where $S(f)$ is the source term, $g(r)$ the geometrical spreading, β the shear wave velocity, r the hypocentral distance (Boore and Joyner, 1997). The
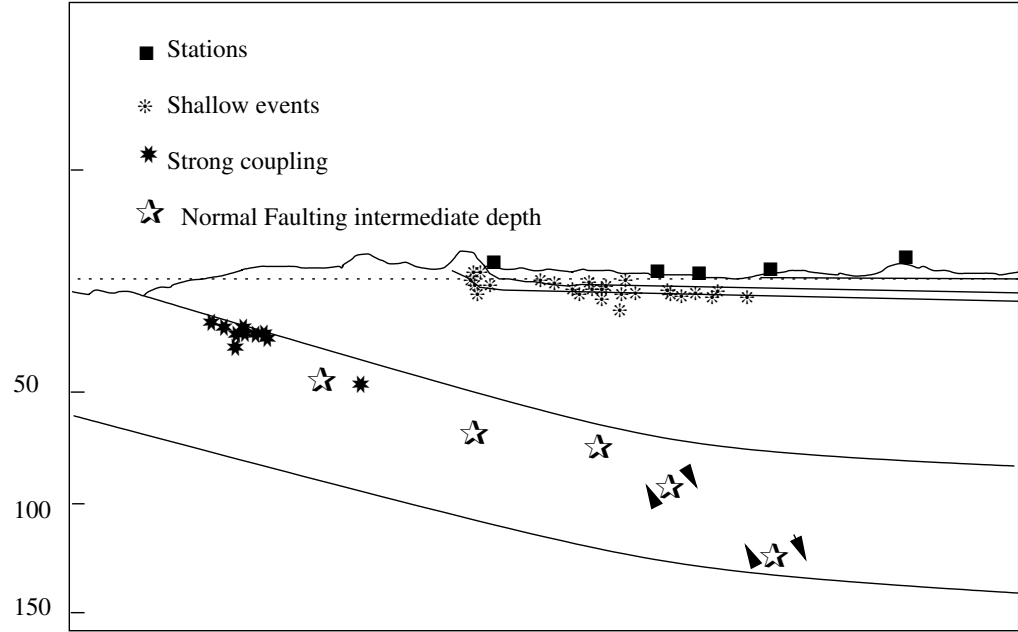
Figure 3.36: Location and type of earthquakes in central México. A common network site effect is expected because of the location of the stations. Two major data sets are present, the shallow low magnitude events including the volcanic events, and the intermediate depth earthquakes. Different propagation terms may be expected because of the different travel paths

V(f) is a frequency dependent site amplification, and κ controls site dependent attenuation of high frequency (Anderson and Hough, 1984).

If we define the network average amplification and κ values as $\overline{V(f)}$ and $\overline{\kappa}$ respectively, the network average site effect including the effective site dependent attenuation high frequency factor, $\overline{\kappa}$, and the amplification factor $\overline{V(f)}$ are mapped into the excitation term in the regression analysis because of the constraint $\sum_{i=0}^{nsites} Site_i(f) = 0$. The regression terms are modeled as (Herrmann, pers. comm.)

$$E(f) = log(S(f)g(r_{ref})exp\left[\frac{-\pi f r_{ref}}{\beta Q(f)}\right]\overline{V(f)}exp\left[-\pi f \overline{\kappa}\right]) \qquad (3.12)$$

$$D(r, f) = log\left(\frac{g(r)exp\left[\frac{-\pi fr}{\beta Q(f)}\right]}{g(r_{ref})exp\left[\frac{-\pi fr_{ref}}{\beta Q(f)}\right]}\right) \qquad (3.13)$$

$$Site = log\left(\frac{V(f)exp\left[-\pi f\kappa\right]}{\overline{V(f)}exp\left[-\pi f\overline{\kappa}\right]}\right) \qquad (3.14)$$

Since the excitation and site terms tradeoff with the network average site effect ($\overline{V(f)}exp\left[-\pi f\overline{\kappa}\right]$) an absolute value for the site and the excitation term is not possible. Knowledge of site amplifications for generic rock sites can complement this study, by permitting a reference to a hard rock site. For this study, these true amplifications are not possible, but we can compare the levels of excitation with some site models in western North America. A complete study using borehole data and S-wave velocities in the crust as a guide for deeper velocities can be used to determine average velocity versus depth, and amplification versus frequency (Boore and Joyner, 1997).

3.9   Site Terms

The site terms from our regression are similar for the time and frequency domain regressions. Recall that to perform the regression the site term at station PLIG was constrained to be zero. The PLIG broadband station recorded the most events in common with both networks. I interpret the excitation term of equation 3.12 as the expected ground motion level for an earthquake at the reference distance $r_{ref} = 40$ km, for this network at a PLIG like site. The site terms represent the motions at other sites relative to that expected at PLIG. This emphasizes the fact that we characterize the motions in a relative sense without any absolute site amplification

or source excitation. There is little frequency variation in the site terms among the stations shown in Figure 3.37. There is no single amplification function and attenuation parameter that can characterize all rock sites, at least, a study for generic rock classes in the México Valley would provide good estimates for the prediction of strong motions at different sites.

From a visual inspection of Figure 3.37 we can see that the site term for each stations may vary from PLIG in a factor of 10. It has been shown that even in the hill-zone sites within and around the valley of México there is an amplification which may reach about 10 at frequencies between 0.2 and 0.7 Hz (Singh et al., 1988; Singh et al., 1995; Ordaz and Singh, 1992). The cause of this amplification is not completely understood yet, and a better explanation is crucial for the seismic hazard of the region, especially for the México Valley, and other cities located in the Mexican Volcanic Belt, where presently there is a lack of appropriate seismic instrumentation and data. In Figure 3.37 we see that each site term is parallel to the other sites, suggesting an homogeneous calibration of the entire network.

The sites in the valley of México may lie over one of the following stratigraphies (Singh et al., 1995)

a) Upper Cretaceous sedimentary rocks about 4 km thick. Stations as PLIG and YAIG on the south of the Valley lie over these rocks.

b) Miocene volcanics (tuffs and recent lava flows) above Oligocene volcanics. With a total thickness of about 2 km. Sites as CUVM and PBVM are located in this lithology.

c) Pleistocene volcanics (lavas) overlying those of Oligocene. The station MDVM is an example of this site.

d) Clays of 10 to 200 m thickness overlying the Miocene volcanics. This

stratigraphy corresponds to the lake-bed zone. We did not use any station located in this type of site.

The only stations in a Cretaceous sedimentary rock are PLIG and YAIG, both stations are BB. We note that YAIG is similar to PLIG but with negative values (see Table 3.13). This suggests amplification on our reference site PLIG. The Quaternary volcanic sites have a trend of increasing amplification with increasing frequency (CGVM,CHVM,LMVM,ORVM).

We observe the highest amplification on two stations PNVM and RFVM. At high frequencies PNVM reached amplifications up to 10 times, this station was triggered only by one event of our data before it was removed and we have no more observations, the latter station (RFVM) replaced PNVM and lies on unconsolidated soil with similar lithology as PNVM (Quintanar, 2000; pers. comm).

Singh et al. (1995) observed amplification of seismic waves at hard sites summarized by the following:

1) All hard sites located above volcanic rocks show amplification.

2) The sites in Iguala (e.g. PLIG) show little if any amplification. They are situated on limestones and shale interbedded with sandstone.

3) At hard sites in the Valley of México, the amplification is least above competent Oligocene volcanic rocks belonging to stratigraphy (c). The period at which maximum amplification occurs is about 3 sec, varying between 1.4 to 4.8 sec in the lake zone of the valley.

We observed a similar situation in this study except that the station at Iguala (PLIG) shows some amplification. Many explanations have been offered for some of the observations about the amplification, all of them are related to the presence of low velocity layers in the Oligocene, Miocene
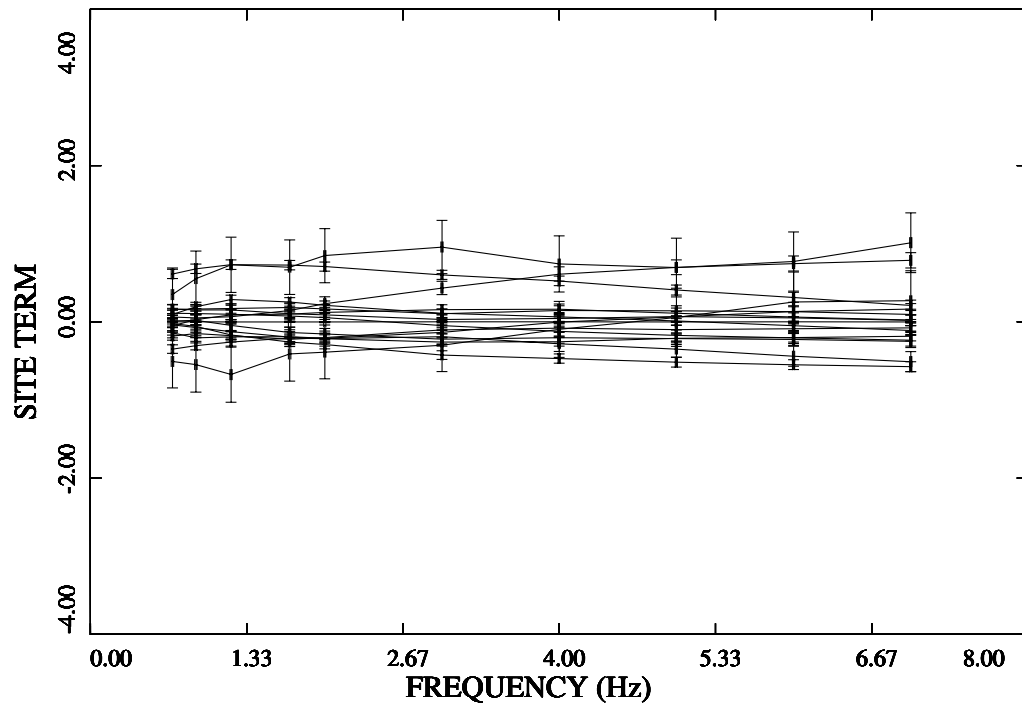
Figure 3.37: Site terms for the filtered velocity as a function of frequency. Each line represent different stations, note that each site term is parallel to the other sites, suggesting an homogeneous calibration of the entire network.

or Pliocene strata (Singh et al., 1995; Ordaz and Singh, 1992; Bard et al., 1988).

Site amplification					
Network	ID	Lithology	2 Hz	4 Hz	6 Hz
RSVM	AYVM	Quaternary Tuff	0.123	0.161	0.006
RSVM	CGVM	Quaternary Tuff	-0.201	-0.003	0.132
RSVM	CIVM	Upper Tertiary Breccia	0.233	0.611	0.745
BB	CUIG	Miocene Breccia	-0.215	-0.280	-0.440
RSVM	CHVM	Quaternary Breccia	-0.165	0.144	0.128
RSVM	PNVM	Upper Tertiary Andesite	0.846	0.741	1.01
BB	PLIG	Cretaceous Limestone	0.000	0.000	0.000
RSVM	MDVM	Miocene Andesite	0.008	0.004	0.004
RSVM	LMVM	Quaternary Breccia	-0.386	-0.009	0.255
RSVM	ORVM	Quaternary Breccia	-0.201	-0.008	-0.008
RSVM	PBVM	Upper Tertiary Basalt	-0.154	-0.202	-0.222
RSVM	PTVM	Upper Tertiary Andesite	-0.288	-0.469	-0.548
BB	PPIG	Upper Tertiary Breccia	-0.005	-0.121	-0.205
RSVM	RFVM	Soil Quaternary sediments	0.706	0.522	0.313
RSVM	SZVM	Upper Tertiary Andesite	0.212	0.006	-0.005
BB	YAIG	Cretaceous Limestone	-0.217	-0.254	-0.200

Table 3.13: Site terms at 2 4 and 6 Hz

4. Relations Between Small and Large Earthquakes

4.1　Source Spectra Observations

Source spectra studies (like spectral scaling relations) are essential for characterizing the rupture process and for estimation of ground motion parameters. In this Chapter I will discuss the relation of source term to the observed excitation $E(f)$ in more detail. The relation was formulated in equation 3.12.

4.2　Events with Unusual Excitation Spectra

An interesting pattern was observed in the excitations. In a plot of all excitations I noted two distinct populations which I easily separated by the different low/high frequency level ratio. After separation I formed averages of those about selected levels which are shown in Figure 4.1. The earthquake pattern which rises with increasing frequency were very easy to distinguish by the *"bell"* shape of the ω^2 model (the ω^2 model will be discussed later in this chapter).

The epicenters of the events with anomalous spectra are plotted in figure 4.2. They form a tight group and may be related to mining and volcanic activity in the region. I identified 47 events with this anomalous characteristic in the excitation term, with depth ranging from 0 to 10 km. Recently (Koch, 2000 pers. comm.) observed similar patterns from a similar study in Germany (Malagnini et al., 2000b). Koch observed differences in the spectral slope, and on the spectral variance. He found that the mining
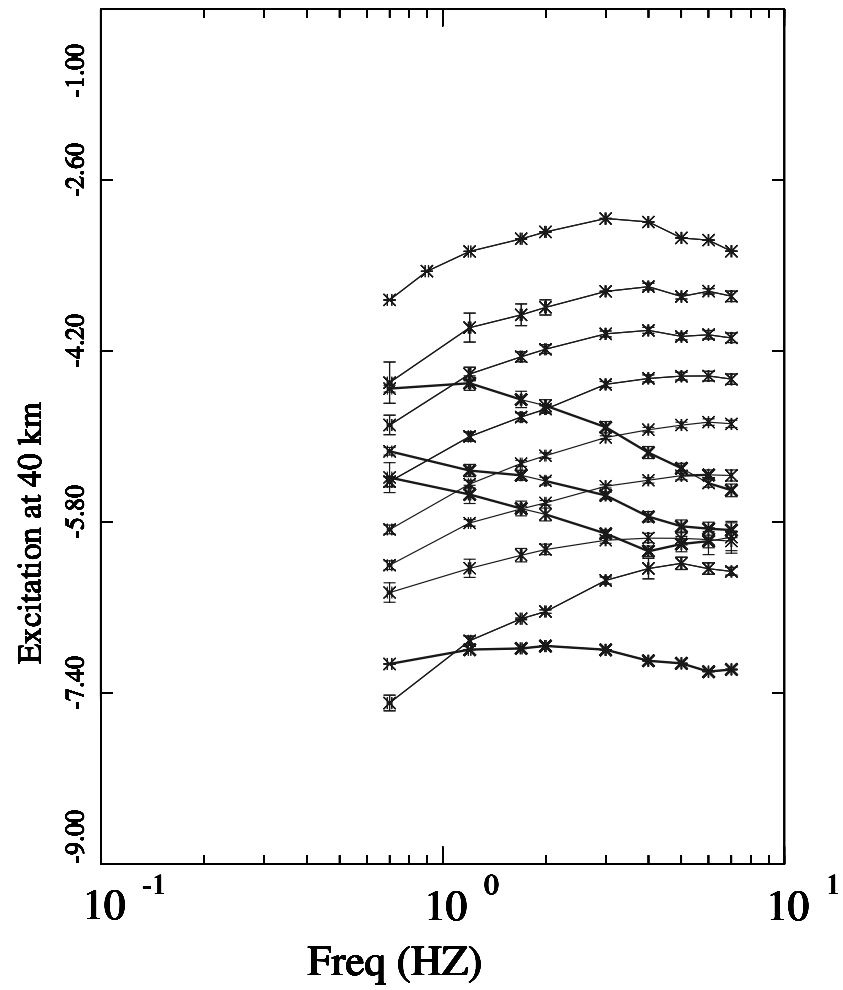
Figure 4.1: Excitation term binned at different levels. The different patterns in the source spectrum are clearly shown.
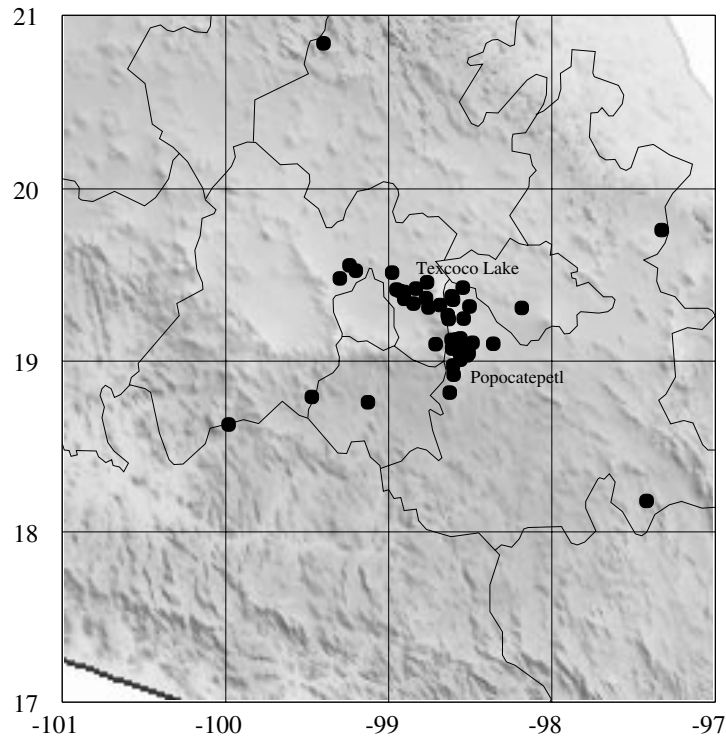
Figure 4.2: Epicenters of events producing unusual excitation spectra. Most are located in the volcanic and mining region near Popocatépetl volcano.

blasts show large levels of spectral variance, while the earthquakes show small variance.

The eastern part of the Valley of México consists of a system of lakes in the Texcoco zone. This region is mined constantly at different locations. I found a considerable number of events in the Texcoco zone that fit the location of known mining. Mining practice gives rise to different type of sources, e.g. in the underground coal mines in the state of Utah, the mining related events originated from the wall and ceiling collapses (Jeon,2000). The excitation terms of those Utah events are similar to those in the Texcoco and Popocatèpetl region in central México.

Volcanic or mining activity can be studied more carefully on the TMVB.

Central México is a very active tectonic region, many active volcanoes on the TMVB contribute to the geologic hazard of the region. The volcanic hazard in central México is a main concern. Two major volcanoes (Colima and Popocatépetl) are constantly monitored. However, in general, the volcanic activity in the TMVB has not been studied in detail. This study provides an excellent tool for volcanic hazard monitoring, e.g. using a regional network to define anomalous, perhaps volcanic events.

The source of small earthquakes and mining blasts is difficult to study. Regional broadband networks usually do not cover the region in detail. On the other hand, portable seismic networks are expensive and do not stay permanently in the region. This study shows the need of permanent operation of the regional seismic networks, and provides important tools for a volcanic monitoring and on the identification of the numerous low-yield mining events.

4.3   Intermediate Depth Earthquakes

In this section I want to describe some characteristics of the intermediate depth earthquakes. On June 15, 1999, a large earthquake (mb 6.3, Ms 6.5, Mw 7.0) occurred in central México. Many cities in the states of Puebla and Oaxaca were severely affected. The earthquake caused damage to the villages near the epicentral region and to historical buildings in the city of Puebla. Singh et al. (1999) determined the earthquake source characteristics using regional data. They estimated a scalar moment of 2.0×10^{26} dyne-cm, and depth of 60 km. The moment tensor solution was obtained from the inversion of filtered (20 - 50 s) BB regional seismograms. From
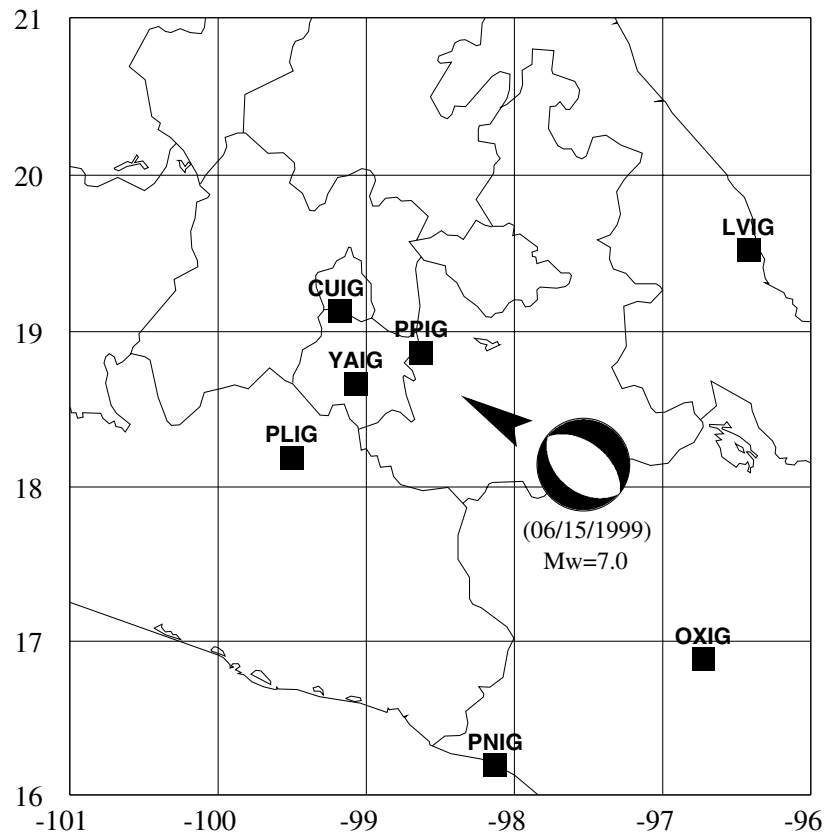
Figure 4.3: Stations and event location for the February 15th, 1999 event. The directivity is indicated by the arrow.

accelerograms they observed that the stations located to the NW show shorter durations of the intense part of the ground motions than the rest of the stations. This suggested a directivity of the source toward the northwest. Pacheco and Singh (2000) performed a teleseismic body wave inversion which also showed directivity towards the NW. The stations in the Valley of México are located at the same direction. Figure 4.3 shows the station locations, and the event location.

Figure 4.4 show the excitation term for the complete data set; the two highest excitation levels correspond to this event. The stations used in this study (YAIG, PLIG, CUIG and PPIG) are located towards the northwest

of the epicenter and show a considerable elevation of the excitation term compared to stations in other azimuths (LVIG, OXIG, PNIG), to obtain the excitation the YAIG, PLIG CUIG and PPIG were removed from the data set and the regression was performed again. LVIG, OXIG and PNIG were not used initially because they cover different distance ranges. They are still located in the region of interest, and for this specific case we were able to perform the regression. The excitation level is three to four times lower for these stations than the ones near the Valley of México.

A small earthquake (mb 4.1) occurred on February 15, 1999 in the southwestern region of central México. Figure 4.4 also shows the excitation level (dash lines) for this event. For such a low magnitude, the high excitation levels are not clearly explained. Radiation pattern, high stress drop for deep earthquakes, and different propagation characteristics need to be considered. These unusual high energy events are common below the downdip edge of the subducted plate (Singh et al., 2000). This event also occurred at a 63 km depth and a satisfactory explanation of the stress regime and stress interactions between these types of earthquakes are still part of active research.

4.4 Earthquake Spectra Scaling Relations

In routine moment tensor inversions the scalar seismic moment (M_0) may not be available for small earthquakes (M≤ 4) because of a poor long period signal-to-noise ratio. The scalar seismic moment is an important physical quantity that relates the fault surface area, the rigidity of the rock and the average displacement on the fault (see equation 4.2), and it is a
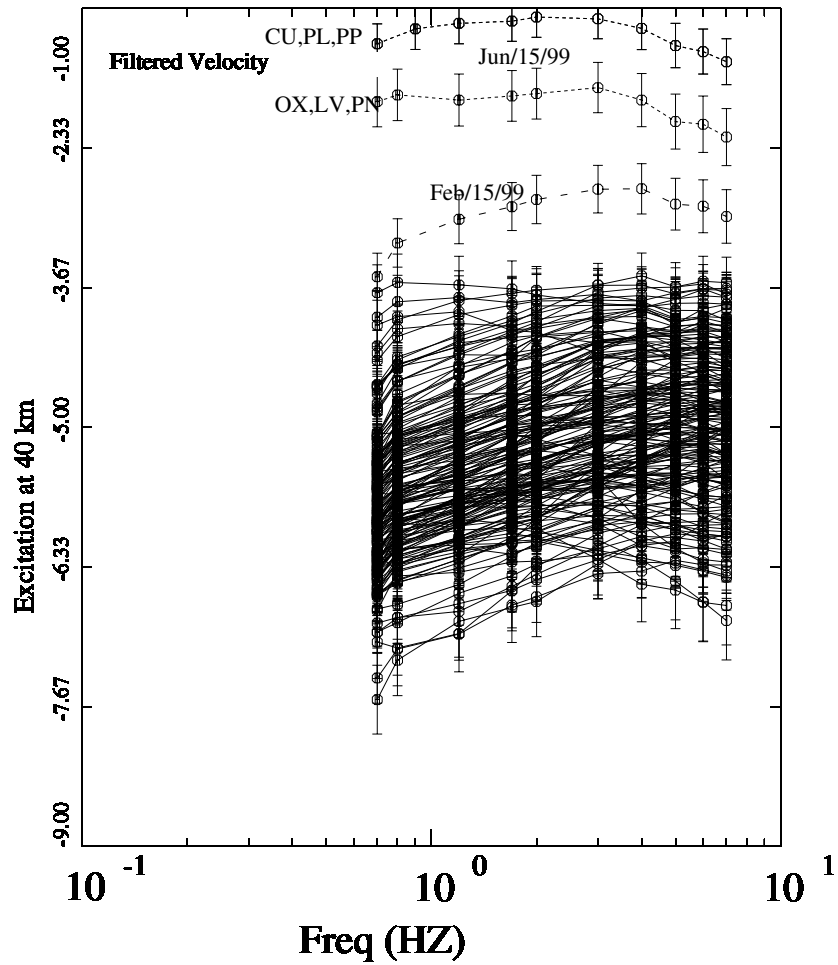
Figure 4.4: Excitation terms. The volcanic events have been removed. The two excitation levels at the top correspond to the same earthquake for different stations, the differences on the excitation levels are attributed to directivity effects (Singh et al.,1999). The third event from the top corresponds to a small earthquake on February 15, 1999.

good estimate of the size of the earthquake. The knowledge of M_0 is important for comparing small and large earthquakes by way of *spectral scaling relations*. These scaling relations usually are expressed in the form of a corner frequency that will be used later for modeling the source term. The corner frequency f_a has the form of

$$f_a = K \left(\beta / L \right) \tag{4.1}$$

where K is a constant depending on the geometry of the source related to the spectrum model (Beresnev and Atkinson, 1997) and L is the fault radius and β is the shear wave velocity. The total seismic moment is defined as

$$M_0 = \mu A D \tag{4.2}$$

where D is the final slip of the source and A is the rupture area and μ is the rigidity of the rock (Aki, 1968). From Hooke's law the stress drop, $\Delta \sigma$, is

$$\Delta \sigma = \mu D / L \tag{4.3}$$

Combining 4.2 and 4.3

$$M_0 = \Delta \sigma L A \approx \Delta \sigma L^3 \tag{4.4}$$

The corner frequency scaling relation in 4.1 then can be expressed in terms of the stress drop and scalar moment M_o. A common spectral scaling relation for a circular rupture was given by Brune (1970)

$$f_a = 4.91 \times 10^6 \beta \left(\Delta \sigma / M_0 \right)^{1/3} \tag{4.5}$$

where β is the shear wave velocity in km/s, $\Delta \sigma$ is in bars and the seismic moment M_0 is in dyne-cm. The constant 4.91×10^6 depends on the geometry of the source and the type of model spectra. The corner frequency f_a

is used to represent the source term in

$$S(f) = \frac{1 - \varepsilon}{1 + (f/f_a)^2} + \frac{\varepsilon}{1 + (f/f_b)^2} \qquad (4.6)$$

where f_a and f_b are two different corner frequencies estimated from the spectral scaling relations (Atkinson and Boore, 1998). The two corner model is an extension of the single-corner Brune model, ε is a relative weighting parameter whose values lies between 0 and 1 (where $\varepsilon = 1$, the two corner model is identical to a single-corner Brune model). When f_a and f_b differ, and $\varepsilon \neq 0$ or 1, equation (4.6) can give intermediate f^{-1} trend between the f^o and f^{-2} asymptotes. The f_a, f_b and ε are functions of M_ω for a specific region. Atkinson and Boore (1998) called these source models as "apparent source spectra" or "effective source spectra", where *apparent* or *effective* refers to the fact that they are deduced empirically from far field observations. They are not physical model of source processes but they represent models of the effect that the source processes have on ground motions observed at sites on the Earth's surface. From equation 4.5 we note that the corner frequency f_a depends on the stress drop (or stress parameter), $\Delta\sigma$, and the scalar seismic moment M_0. When the scalar seismic moment is known, then the only unknown variable to represent the source term is the stress drop ($\Delta\sigma$). While simple in appearance, a true estimation of the stress drop is not possible from seismic observations.

Ordaz and Singh (1992) observed that some Mexican earthquakes which occur on the west coast require different stress drops as a function of their size. Ordaz and Singh observed that the high frequency level of the spectra can be explained with the Brune spectra scaling relation on equation 4.5 requiring $\Delta\sigma$ between 50 to 300 bars for earthquakes bigger than Mw

6. However, the smaller events required higher stress drops (300 to 800 bars) to fit the same model. If this is true, the spectral scaling relation that we are using may not be adequate. This discrepancy may reflect saturation effects attributable to the point-source distance measure, rather than real stresses on the fault (Atkinson and Silva, 1997). Since our data set consists of small earthquakes, there is often no information about the source parameters, other than a local magnitude.

4.5   Excitation Term

Following Atkinson and Boore (1995), we represent the source term as

$$S(f) = \frac{1 - \varepsilon}{1 + (f/f_a)^2} + \frac{\varepsilon}{1 + (f/f_b)^2} \qquad (4.7)$$

where f_a, f_b and ε are described in Table 4.1 for the different model that we tried.

Table 4.1 presents the parameters used to model the source term by different authors. These models have been developed for different regions in the United States. Caution is warranted in applying any of these models to different regions in the world, especially to México.

The two $g(r)$-$Q(f)$ models proposed before (section 3.6) were compared with the observed excitation terms. The prediction of the Fourier velocity spectra for a frequency f at a distance r is

$$a(r, f) = S(f)g(r)e^{-\frac{\pi f r}{Q(f)\beta}}V(f)e^{-\pi f \kappa} \qquad (4.8)$$

where $a(r, f)$ is the Fourier velocity spectra, $S(f)$ is the source spectra defined in equation 4.7, $g(r)$ is the geometrical spreading, $V(f)$ is a frequency dependent site amplification function and κ is a parameter that controls

Source Parameters		
Atkinson and Silva CAL 1997		
ρ	2.7	
β	3.2	
f_a	$log\, f_a = 2.181 - 0.496$	$M \geq 4.6$
	$f_a = f_b$	$M \leq 4.6$
f_b	$log\, f_b = 1.778 - 0.302M$	$M \geq 4.6$
	$log\, f_b = 2.689 - 0.500M$	$M \leq 4.6$
ε	$log\, \varepsilon = 3.440 - 0.746M$	$M \geq 4.6$
	$log\, \varepsilon = 0.0$	$M \leq 4.6$
Atkinson and Boore CAL 1997		
ρ	2.8	
β	3.5	
f_a	$log\, f_a = 2.181 - 0.496M$	$M \geq 4.8$
	$log\, f_a = 2.617 - 0.500M$	$M \leq 4.8$
f_b	$log\, f_b = 1.308 - 0.277M$	$M \geq 4.8$
	$log\, f_b = 2.617 - 0.500M$	$M \leq 4.8$
ε	$log\, \varepsilon = 3.223 - 0.670M$	$M \geq 4.8$
	$log\, \varepsilon = 0.0$	$M \leq 4.8$
Atkinson and Boore ENA 1995		
ρ	2.8	
β	3.8	
f_a	$log\, f_a = 2.41 - 0.53M$	$M \geq 4.0$
	$f_a = f_b$	$M \geq 4.0$
f_b	$log\, f_b = 1.43 - 0.188M$	$M \geq 4.0$
	$log\, f_b = 2.678 - 0.500M$	$M \leq 4.0$
ε	$log\, \varepsilon = 2.52 - 0.637M$	$M \geq 4.0$
	$log\, \varepsilon = 0.0$	$M \leq 4.0$
Boore and Joyner1997		
ρ	2.8	
β	3.5	
$\Delta\sigma$	70 Bars	
f_a	$f_a = 4.9 \times 10^6 \beta \left(\Delta\sigma/M\right)^{1/3}$	
f_b	$f_b = f_a$	
ε	$\varepsilon = 1.0$	

Table 4.1: Source model parameters.

the site attenuation. The Fourier velocity spectra was predicted at a distance of $r = 40$ km and $V(f) = 1$, for the different source models (Figures 4.6, 4.5, 4.8 and 4.7). Model 2 fits the observations better because it predicts the high excitation levels observed in the Tehuacán earthquake, while Model 1 always underestimates the highest values. Perhaps the most simple model is the Boore and Joyner 1997, which represent a circular rupture with a stress parameter ($\Delta\sigma$) of 70 bars is adequate as an initial spectral scaling model.

Although I do not have any calibrated event (the only reliable regional M_o seems to be strongly affected by directivity effects), the value of κ can be estimated from the small earthquakes, since there is little dependence of the shape of spectrum between 1 and 16 Hz as a function of stress drop (Jeon, 2000), thus a $\kappa = 0.04$ sec, was selected. I found that a $\Delta\sigma = 70$ bars was required to match the excitation of small and large earthquakes, however a complete study of seismic sources in this region is strongly recommended in order to calibrate the spectral scaling relations.

Atkinson and Silva CAL 1997
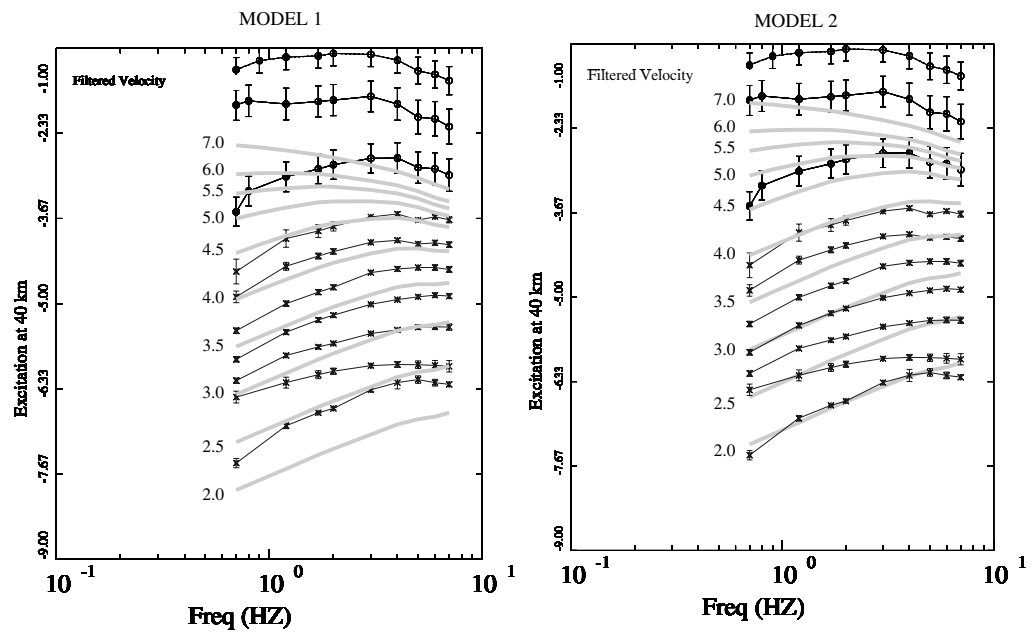
Figure 4.5: Comparison for Atkinson and Silva CAL 1997 source model (smooth gray lines) with observed excitation terms (black lines). The volcanic events have been removed. The two excitation levels at the top correspond to the same earthquake for different stations.

Atkinson and Boore ENA 1995
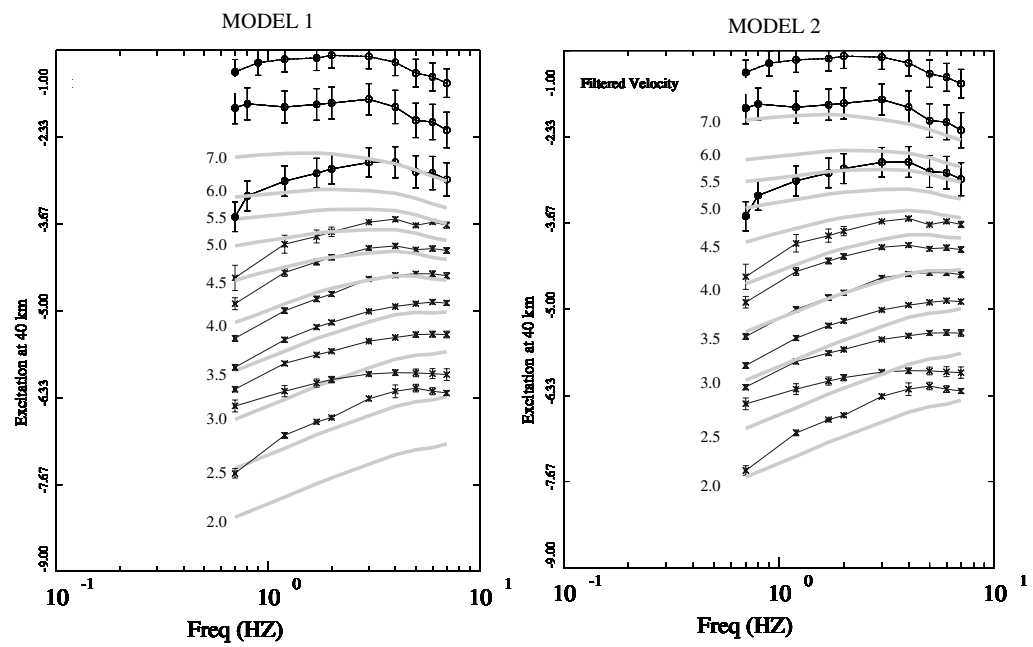
MODEL 1

MODEL 2

Figure 4.6: Comparison for Atkinson and Boore ENA 1995 source model (smooth gray lines) with observed excitation terms (black lines). The volcanic events have been removed. The two excitation levels at the top correspond to the same earthquake for different stations.

Atkinson and Boore CAL 1997
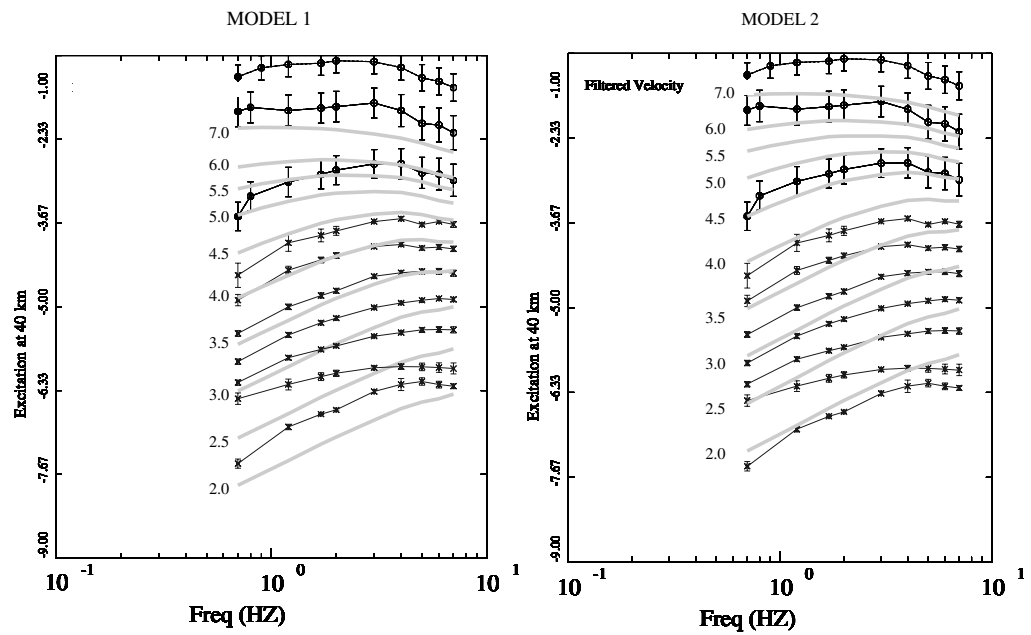
MODEL 1

MODEL 2

Figure 4.7: Comparison for Atkinson and Boore 1998 source model (smooth gray lines) with observed excitation terms (black lines). The volcanic events have been removed. The two excitation levels at the top correspond to the same earthquake for different stations.

Boore and Joyner 1997

MODEL 1

MODEL 2

Filtered Velocity

Excitation at 40 km

Freq (HZ)
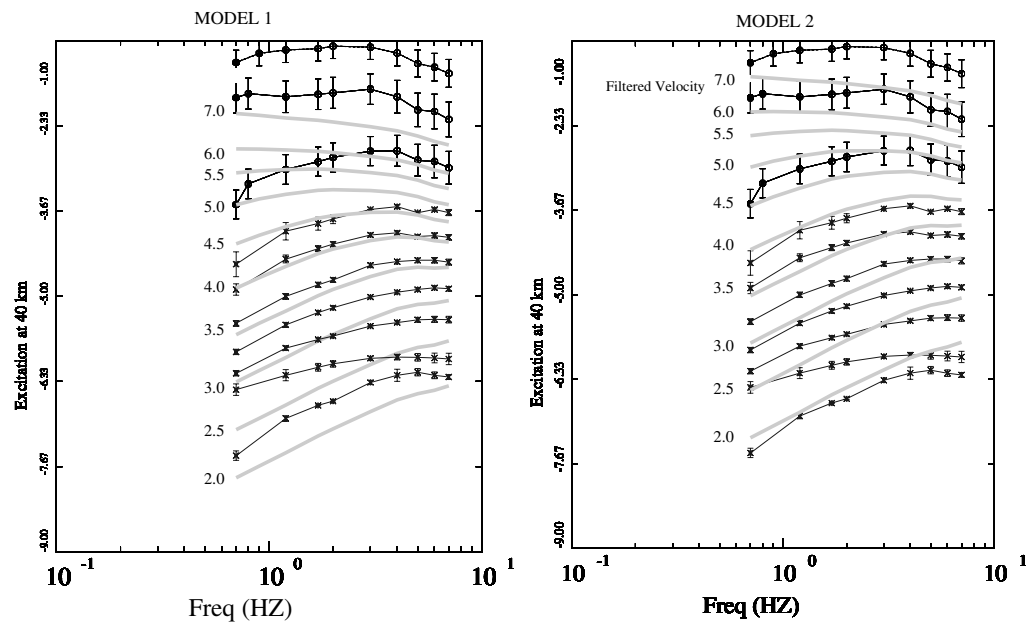
Figure 4.8: Comparison for Boore and Joyner 1997 source model (smooth gray lines) with observed excitation terms (black lines). The volcanic events have been removed. The two excitation levels at the top correspond to the same earthquake for different stations.

5. Results

5.1   Comparision with other Regions

On the basis of recent work (Raoof et al., 1999, Malagnini et al., 2000a,b), new attenuation relations have been developed for other regions, such as Southern California, Italy and Germany. Different tectonic environments may reflect significant differences in the propagation characterization. Comparing our results with Italy, Germany, and central United States (Table 5.1) I find higher ground motion attenuation in central México and Italy (Figures 5.1 and 5.2). The regions are compared only in the distance range of $0 < r < 220$ km using the same frequencies (0.7 to 7 Hz). To enhance presentation, these figures show the deviation from an r^{-1} trend. The horizontal line at zero is the case when there is no anelastic attenuation ($>> Q_o$) with a geometrical spreading of r^{-1}. The main difference between Germany and New Madrid is due to the differences on the geometrical spreading function, and a higher value of Q_o in New Madrid. Both regions are characterized by a low attenuation in the propagation of the seismic waves. On the other hand, Italy and México show high attenuation. The geometrical spreading functions are similar in both regions, except for a transition zone between 50 and 80 km in Italy, characterized by a $g(r) = r^0$. At shorter distances ($r < 50$ km) the body waves dominate the propagation, while at larger distance ($r > 80$ km) the surface waves become the most important propagation. The low frequency dependence η in Italy (0.10) is reflected by the large spread in the propagation function between each frequency.

Propagation Parameters			
Region	Q_o	η	g(r)
New Madrid	900	0.30	r^{-1} $0 < r < 50$ $r^{-0.25}$ $50 < r < 120$ $r^{-0.5}$ $120 < r < 220$ r^{-1} $220 < r < 500$ $r^{-0.5}$ $500 < r < 1000$
Germany	380	0.30	r^{-1} $0 < r < 50$ r^{0} $50 < r < 150$ $r^{-0.5}$ $150 < r < 1000$
Italy	130	0.10	$r^{-0.9}$ $0 < r < 50$ r^{0} $50 < r < 80$ $r^{-0.5}$ $80 < r < 1000$
central México	88	0.72	$r^{-1.3}$ $0 < r < 40$ $r^{-0.5}$ $40 < r < 220$

Table 5.1: Attenuation and geometrical spreading parameters for New Madrid, Germany, Italy and central México.

Central México is characterized by low Q_o compared to other regions in the world, this is an expected result in the TMVB because of the high tectonic activity. However, due to the high frequency dependence $\eta = 0.72$, attenuation at higher frequencies does not differ much from that of lower frequencies as is the case of the Apennines in central Italy. Malagnini et al. (2000a) studied the regional attenuation along the Apennines, he found an attenuation of $Q(f) = 130\,f^{0.10}$ combined with a geometrical spreading: $r^{-0.9}$ for $r \leq 50\,km$, r^{0} for $50 \leq r \leq 80\,km$ and $r^{-0.5}$ for $r \geq 80\,km$. For low frequencies (0.7 to 1 Hz) the attenuation in México is higher than other regions (Figure 5.3). For frequencies between 2 and 3 Hz the attenuation is very similar to the Italian region (Figure 5.4), while for higher frequencies (6.0 and 7.0 Hz) the attenuation curve for Italy decays faster than the Mexican (Figure 5.5).

The values of Q_o found for México and the Apennines may be typical
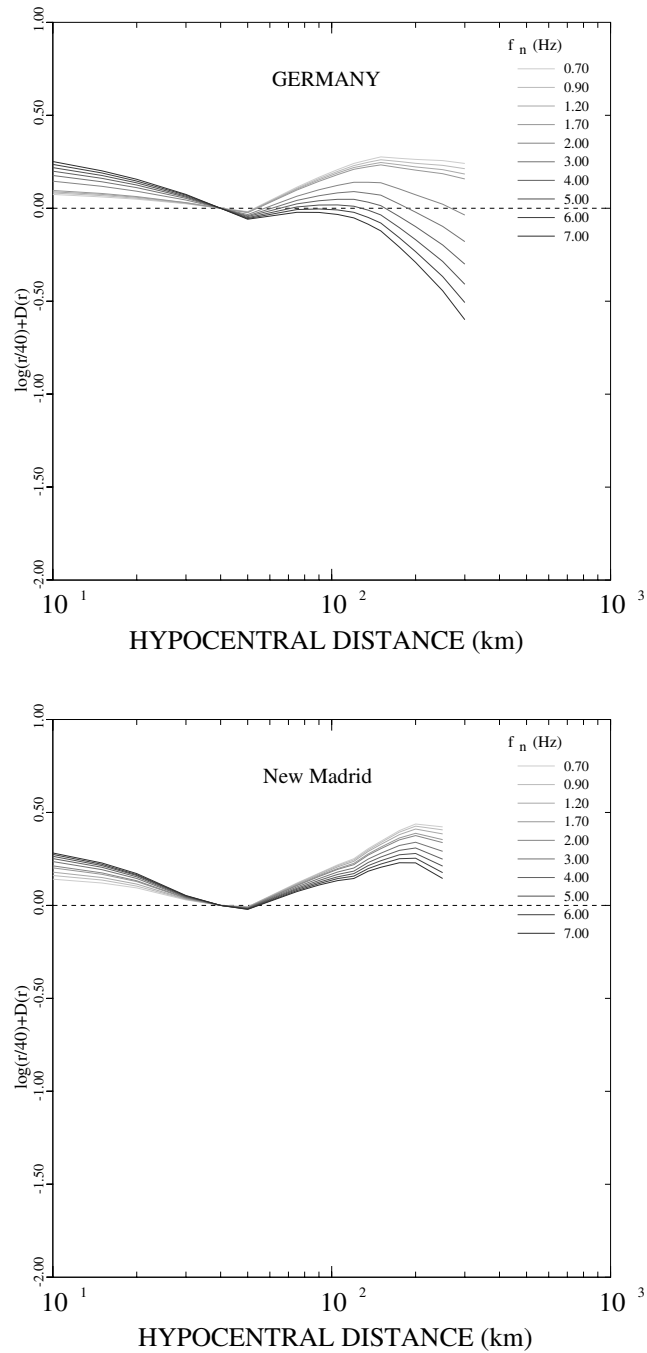
Figure 5.1: Comparison of attenuation of the filtered velocity obtained in different regions in the world. a) Germany, b) New Madrid (Central United States).
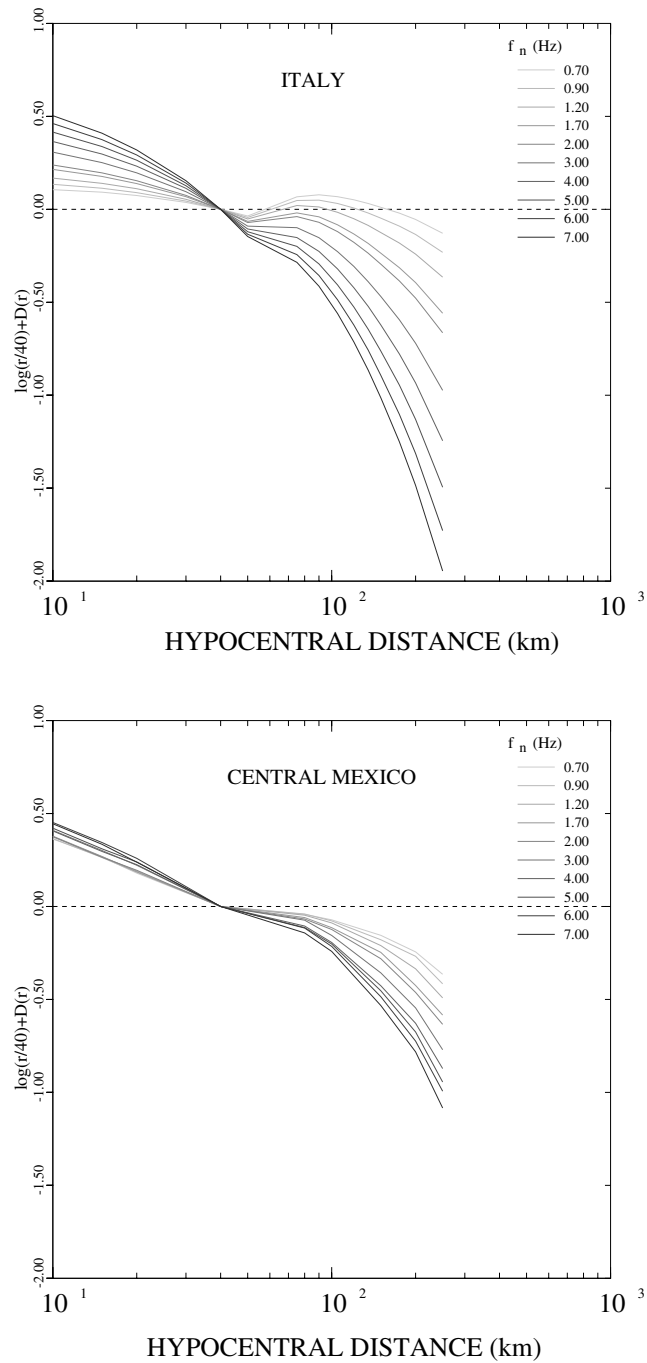
Figure 5.2: Comparison of attenuation of the filtered velocity obtained in different regions in the world. a) Italy, b) Central México.
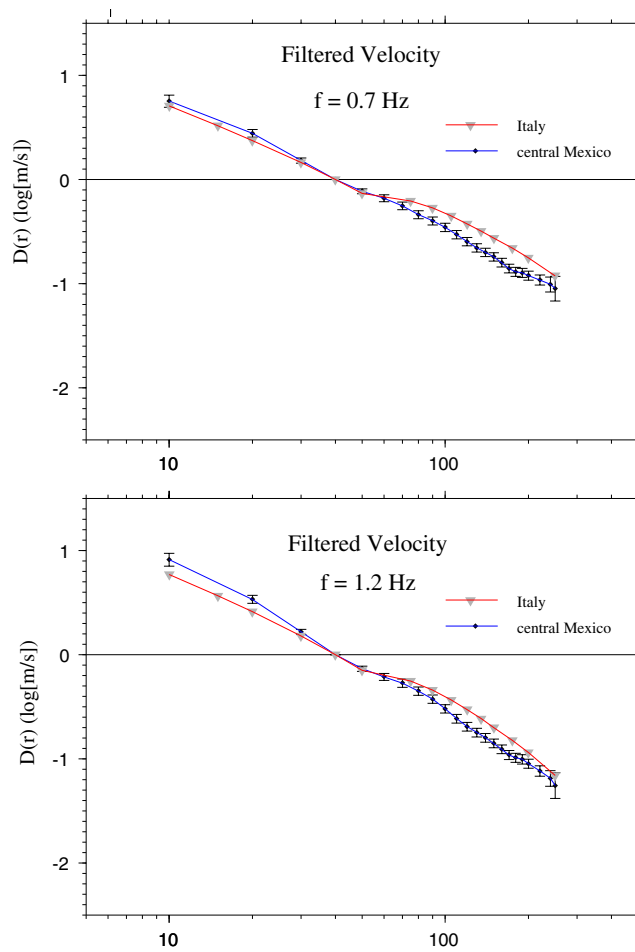
Figure 5.3: Comparison of the central México attenuation functional obtained from the general regression on the peak amplitude at 0.7 and 1.2 Hz (black or blue) and the estimates from Italy (gray or red).
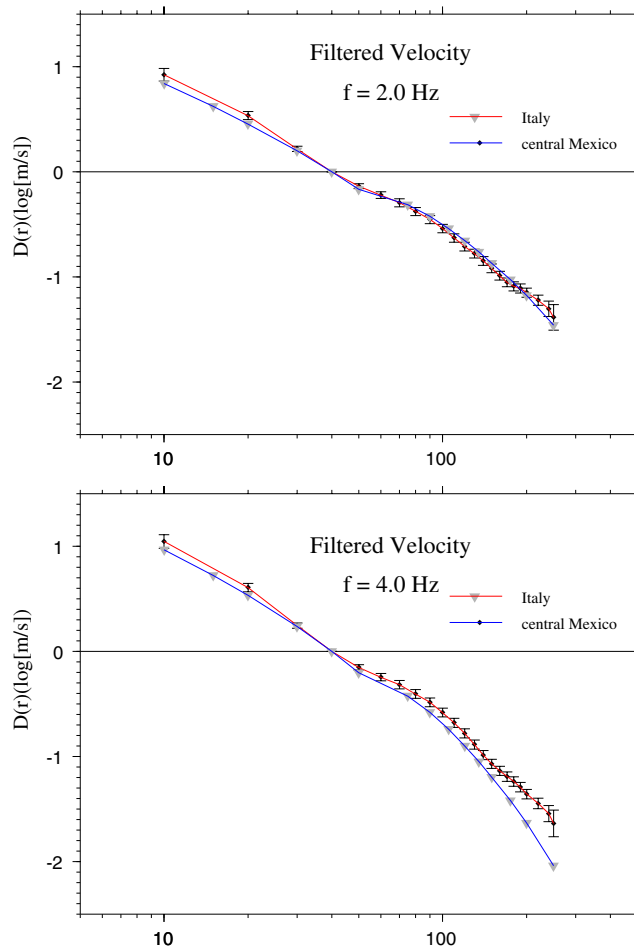
Figure 5.4: Comparison of the central México attenuation functional obtained from the general regression on the peak amplitude at 2.0 and 4.0 Hz (black or blue) and the estimates from Italy (gray or red).
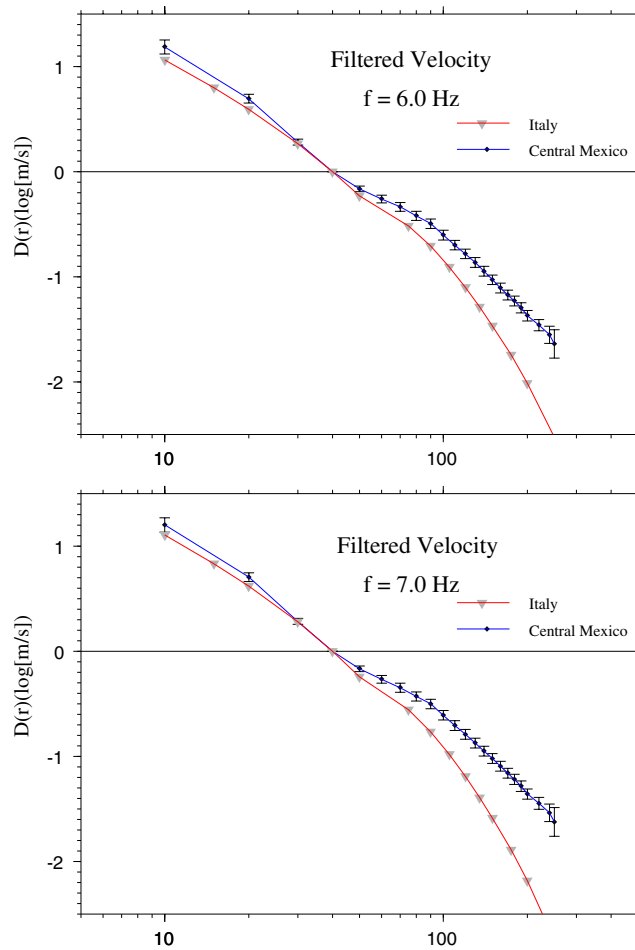
Figure 5.5: Comparison of the central México attenuation functional obtained from the general regression on the peak amplitude at 6.0 and 7.0 Hz (black or blue) and the estimates from Italy (gray or red).

of active regions and may be related to the presence of fluids in the rocks, active faults and fractured rocks, and high heat flow (Mitchell, 1995). Stable regions such as Germany and New Madrid in the central United States have lower attenuation, characteristic of a relatively old history of crustal deformation and long episode of stability. On the other hand, the apparent high seismic attenuation in the TMVB shows the importance of the effects of the local geology with the subsequent consequences for the estimation of seismic hazard in a region that has severely affected by damaging earthquakes many times.

This is clearly a high attenuation region where seismic hazard is not dominated by local seismicity, the most damaging earthquakes in the zone are caused by the subduction zone, especially the coastal earthquakes located about 300 km far from the Valley of México. This intriguing observation seems to be contradictory, but the regional propagation from the coastal events seems to follow a different pattern; large scale variations of the lateral velocity structure may strongly contribute to the amplification and attenuation of the seismic waves, especially the Lg waves. Future studies should include the coastal events from the subduction zone with stations located within and around the TMVB. Some authors (Yamamoto et al., 1997; Campillo et al., 1988; Furumura and Kennett, 1999) have proposed that the propagation of the seismic waves in the TMVB may be affected by some sort of wave-guide geological structure.

5.2 Discussion

The TMVB is a complex tectonic structure and is characterized by two systems of fractures oriented northwest and northeast (Mooser, 1972). This structure is associated with the subduction of the Cocos and Rivera plates during the late Cenozoic. The tectonic processes from the Oligocene and Miocene gave rise to a wide variety of active volcanoes distributed along the TMVB. The heat flow measured in this region is the highest in southern México of about $92\,mWm^{-2}$ (Ziagos et al., 1985). The high attenuation observed in central México is in agreement with the geophysical characteristics of the region, since the largest active volcanoes are located along the TMVB.

There is a considerable difference between our results and those estimated by Ordaz and Singh (1992). Figure 5.6 compares the propagation functional using the parameters estimated by Ordaz and Singh with those estimated in this study. A substantial difference is observed at all distances. However I think that these differences reflect the different regions covered in the studies (Figure 5.7). While I used only inland earthquakes mostly traveling within the TMVB, Ordaz and Singh used only coastal events traveling through the Guerrero tectono-stratigraphic terrane (see Campa and Coney, 1983). This difference shows the importance of a detailed study of the tectonic regions. No large-scale systematic research on regional attenuation in central México within the TMVB had been carried out before. The results presented here are the first for this specific region and they are in agreement with the low observed Q_o which is expected of tectonically active regions.

The different numerical values for the quality factor and geometrical spreading are presented to show the non-uniqueness of the interpretation of the propagation term. Figure 5.8 shows the difference between the observed propagation functional and that predicted using RVT. I compared the two models of section 3.6.

Model 1:

$$Q(f) = 88\,f^{0.73} \tag{5.1}$$

with the geometrical spreading of

$$g(r) \begin{cases} r^{-1.3} & r \leq 40\ km \\ r^{-0.5} & r \geq 40\ km \end{cases} \tag{5.2}$$

Model 2:

$$Q(f) = 220\,f^{0.66} \tag{5.3}$$

with the geometrical spreading

$$g(r) \begin{cases} r^{-1.0} & r \leq 180\ km \\ r^{-0.5} & r \geq 180\ km \end{cases} \tag{5.4}$$

I note that for short distances the prediction may be inaccurate due to errors on the depth estimation. In model 1 the general propagation at large distances seems to attenuate slower than the predicted. For Model 2, there is a better agreement between the observed and the predicted propagation functional at large distances (> 100 km). However in the range between 40-80 km the predicted values are underestimated.

At larger distances the propagation does not occur only within the TMVB and the regional attenuation is averaged from a large scale crustal propagation. For these larger distances a greater value of Q_o is needed, and the values estimated by Ordaz and Singh (1992) or Castro et al. (1990) maybe in better agreement than the one presented in this study. Thus, the
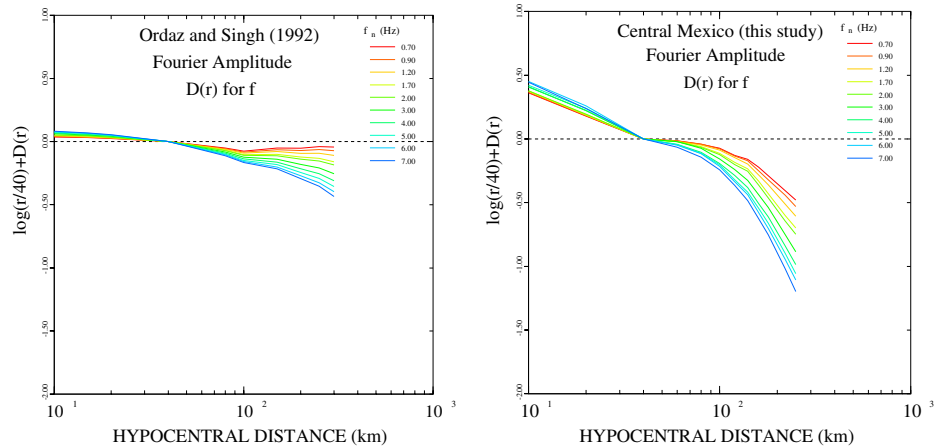
Figure 5.6: Propagation functional using the Ordaz and Singh (1992) model (left) and our model (right).

discrepancies between different studies seems to corroborate the fact that different tectonic regions have important differences in the propagation of high frequency signals.

The intriguing observation of long coda duration in the TMVB has been reported before (Yamamoto, 1997; Canas, 1986). Application of the coda normalization technique to estimate $D(r)$ does not match the general regression results. There are several ways to explain this discrepancy. Part of this deviation may be due to the incomplete azimuthal coverage on the radiation pattern, especially for deep events (the coda wave requires an isotropic backscattered media). From a visual inspection of seismograms, the record of earthquakes with travel paths along the TMVB shows a slow Lg-coda decay and consequently a coda duration longer than any other earthquake of similar magnitude in southern México (Yamamoto et al., 1997), for this reason Lg coda-Q estimated by Yamamoto is considerably higher than that obtained in the present dissertation. The difference between the coda normalization and the propagation functional from the
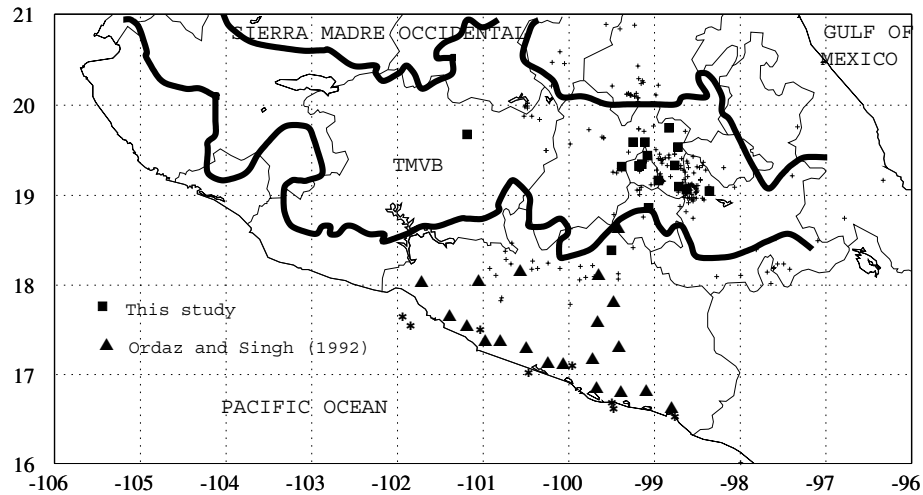
Figure 5.7: Location of stations used in this study (squares) and the ones used in Ordaz and Singh (triangles). Events used in this study (small cross), and events used by Ordaz and Singh (stars). The TMVB boundary is shown in thick lines. The region covered in this study comprises the central part of the TMVB, while the region covered by Ordaz and Singh is located mostly in the Guerrero Coast.

general regression violate the assumption that coda-Q is equal to Q_o for this region.

The considerable long-duration ground shaking in México City has been studied many times (Bard et al., 1988; Sanchez-Sesma et al., 1988; Kawase and Aki, 1989; Mateos et al., 1993a,b; Chavez-Garcia and Bard, 1993a,b, Bard and Chavez-Garcia, 1993). It is widely accepted that the strong amplification of the seismic waves arises from the presence of highly compressible saturated clays, which form the lake-bed zone in the Basin of México City and the strong impedance contrast that these clays layers have with the bedrock beneath. While the amplification has been predicted more or less with a good level of confidence, the long ground motion oscillation has been difficult to predict unless unrealistic physical parameters are employed on the simulation, such as neglecting the anelastic
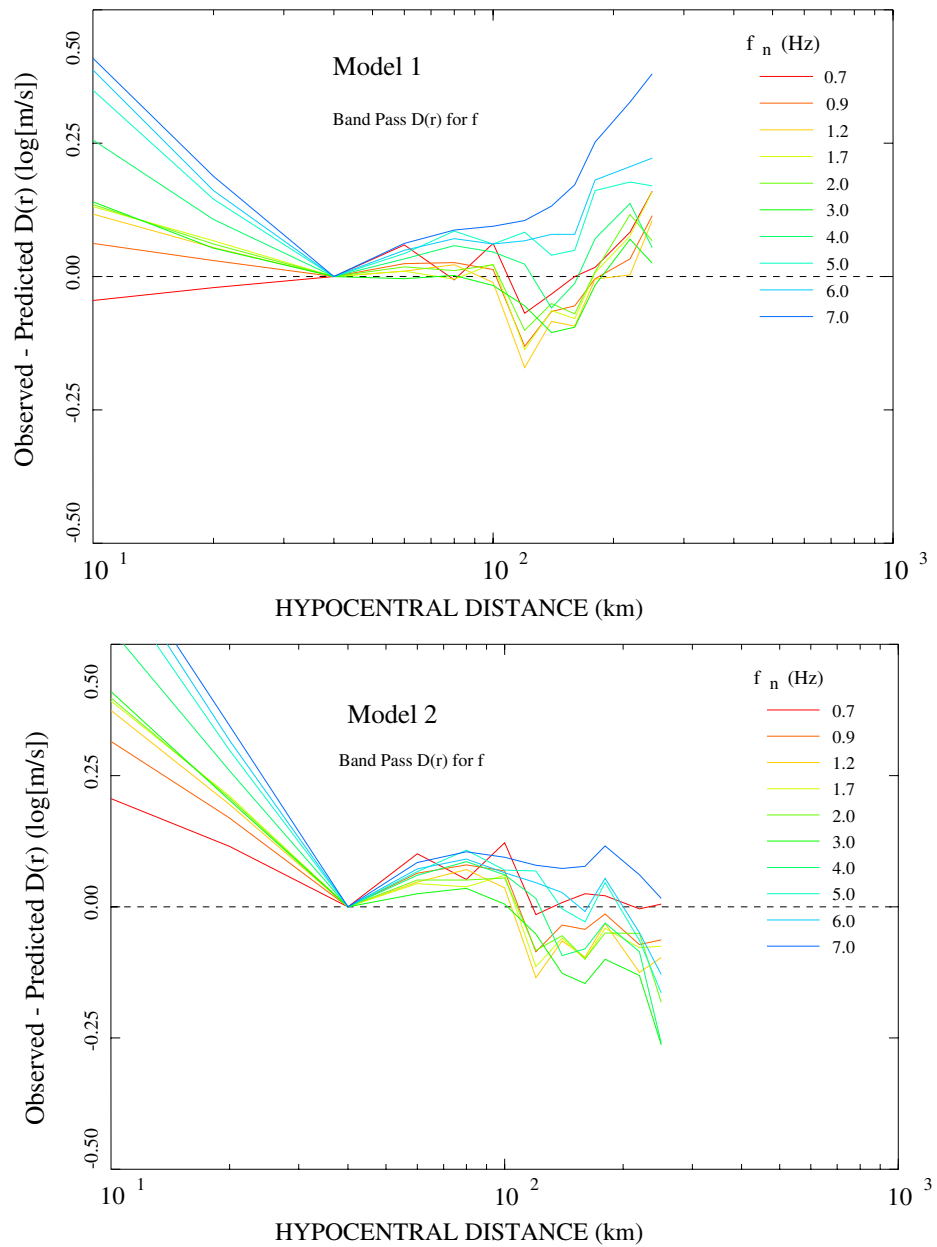
Figure 5.8: Difference between the observed and predicted propagation functional $D(R)$ for the filtered velocity. The errors at short distances are due to wrong depth estimation. Top, Model 1: $Q_o(f) = 88f^{0.73}$, bottom Model 2: $Q_o(f) = 220f^{0.66}$

attenuation effect (Kawase and Aki, 1989), or considering a very rough to-pography in the bottom (Bard et al. 1988). Many other mechanisms have been debated, such as the influence of lateral resonance of horizontally propagating P waves in the clay layer (Mateos et al.1993a,b) and gravity wave generated in soft soil form strong ground shaking (Lomnitz,1992), such mechanisms are very unlikely to affect the Valley of México (Chavez-Garcia and Bard 1993a,b; Lomnitz, 1995; Sanchez-Sesma and Luzon, 1996). Some of these ideas have been exposed to a lively scientific discussion (e.g. Lomnitz, 1995) proposing and rejecting continuously the different causes of the long duration of strong shaking. But the main problem is not ex-plaining the cause of this long duration of ground shaking. But what to do about earthquake hazard on soft ground (Lomnitz et al., 1999).

Another line of explanation was proposed for the long ground shaking of the soft soils in México City, the incident wave on the lake-bed zone is the result of a long multipathing and scattering effect of the seismic waves during the long propagation path (Singh and Ordaz, 1993; Furumura and Kennett, 1997). The present study has not used stations in the soft soil, nor long propagation path from the coast, however the study of the regional propagation within the TMVB is very important in order to understand the cause of the possible mechanisms of the anomalously long-duration shak-ing during the propagation of the seismic waves from the coastal events. As proposed by Barker et al. (1996) the long S-wave coda may result from scattering from the boundaries of the Mexican Volcanic Belt surrounding México City, the long coda and low frequency durations observed in this study seems to corroborate the above observation. Scattering can decrease the amplitude of a seismic phase by shifting energy from the direct arrival

back into the coda (Lay and Wallace, 1995); this redistribution of energy is reflected as an apparent attenuation of the seismic waves, and is often characterized by an exponential attenuation quality factor Q_s. The Q_o measured in the present study is the combination of an intrinsic anelastic attenuation Q_i and a scattering attenuation Q_s. Where the total attenuation Q_o is given as (Mayeda et al., 1992)

$$\frac{1}{Q_o} = \frac{1}{Q_s} + \frac{1}{Q_i} \tag{5.5}$$

A highly scattering media is characterized as a highly attenuative region, but this is not a true anelastic process. The scattering attenuation affects the duration of the seismic waves train, increasing it as scattering attenuation increases.

Regional propagation plays a very important role for studying complex interference effects, especially the study of the Lg phase. This particular phase only propagates in the crust as a sum of a number of higher-mode surface waves sampling from the free surface to the crust-mantle boundary. Furumura and Kennett (1998) observed that the relative amplitude of Lg is enhanced on the basin of México City, especially at distances beyond 250 km; they also observed that the amplitude of the Lg wave is suddenly weakened after traveling through México City. The enhanced Lg wave train for the inland stations is not seen in records of the coastal ones at similar distances. Ordaz and Singh (1992) observed that the Lg wave has a large amplitude from shallow earthquakes. Furumura and Kennett (1998) proposed that the heterogeneity in the crustal wave-guide produced by the subduction of the Cocos Plate and the near-surface geology of low velocity rocks of the TMVB was the cause of a regional amplification of

the Lg waves. With the observations mentioned above, I suggest that the present study gives support to the idea of the dominance of the Lg wave at regional distances, even that the distance coverage did not extend beyond 250 km. However, the general trend observed in Figure 5.8 (top) suggests the tendency of enhancing the amplitude of the Lg waves with increasing distance. I should note that the farthest events of our data are located towards the coast.

Singh and Ordaz (1993) observed that the long-duration coda observed in the lake bed is present in the coda recorded in the hill zone. Fäh et al. (1994) performed a 2-D simulation to evaluate the seismic wave disturbances caused by the heterogeneities in the Basin of México City, they concluded that the dispersion of high-frequency surface waves through a long propagation path was the cause of the long-duration ground shaking, Shapiro et al. (1997) proposed that the anomalously low shear-wave velocity of the volcanic rocks on the TMVB was the cause of this dispersion of the seismic waves. They observed a significant increase on the signal duration using 2-D simulations.

The cause of long-duration ground shaking in the lake-bed is still under debate. Our definition of time duration is seen in a slightly different manner, it only considers the duration of the maximum ground motion amplitude, instead of measuring the entire coda duration. I use duration as an input parameter that estimate the maximum peak using RVT. Whatever is the cause of the long-duration coda and high amplification, the propagation functional was estimated in using the duration observations.

Because of the nature of the data used in this study, the earthquakes used come from different sources: deep and shallow earthquakes are present

in this region, small and large events, volcanic events, intermediate depth normal faulting earthquakes. This mixed data set affects our results. One problem when I deal with deep earthquakes is the radiation pattern. The radiation pattern ($R_{\theta\varphi}$) average is generally assumed $\simeq 0.55$ when the focal sphere is completely sampled (Boore, 1983). For deep earthquakes recorded at local and regional distances this is not the case and the average radiation pattern should be accounted for. Large earthquakes may have directivity effects and should be taken into account as the case of the June 15, 1999 earthquake. Somerville et al. (1997) modified ground motion attenuation relations to include the amplitude effects of rupture directivity. These variations become significant around the period of 0.6 Hz.

The attenuation at low frequencies (0.7 Hz) seems to be higher than other parts of the world, especially at the resonance periods of the lake bed (around 2 seconds). For the Tehuacán earthquake, most of these resonance frequencies were filtered out when the seismic waves reached the Valley of México. This high attenuation at low frequencies (0.5 - 0.9 Hz) explains why some of the deep earthquakes do not affect the valley of México as strongly as similar size shallow events from the coast. Apparently, the shallow coastal events excite larger S, Lg and surface waves than the deeper regional events, all these propagation effects reflect the nature of the earthquake and the propagation path. Thus a single propagation functional does not entirely characterize the propagation of the seismic waves in a complex region such as central México.

In the event of a large earthquake near the Valley of México the propagation of the seismic waves will be very different than the ones coming from the coast. The possible scenarios which may have devastating con-

sequences should be considered. Future revisions of the seismic codes should take into account different propagation effects depending on the travel path and earthquake source depth. The traditional approach of estimating the seismic hazard using simple predictive relationships should be reviewed in order to have more realistic predictions for the earthquake damages depending on the location, source mechanism and propagation path.

Large-scale systematic research for the attenuation relations must be done in more detail in México by considering the different characteristics of the earthquake sources, seismic wave propagation, tectonic activity, maximum magnitudes, and earthquake recurrence, for the different geotectonic provinces. This study has only considered the central part of México, especially the propagation of the seismic waves traveling within the TMVB with inland foci. Other regions, as the Guerrero or Oaxaca, have been studied (Castro et al. 1990; Ordaz and Singh, 1992; Castro et al. 1994) but many other active regions have not been investigated with the same detail (eg. Jalisco, Baja California Norte or Chiapas).

The background seismicity of an active region may be able to predict ground motion even for earthquakes of larger size (M$\geq$ 7). An absolute calibration was not performed because of the uncertainties about the moment magnification of small events combined with the directivity effect and observed site amplification. However, from a visual inspection of the source models and the excitation terms (Figures 4.6 to 4.7) I observe that in general there is a good agreement between the observed and the predicted terms. The source characteristics in central México need more study since the observed excitation levels depend strongly on the assumed ge-

ometrical spreading at short distances. Some anomalous excitation levels need to be explained especially for the intermediate depth earthquakes that seem to be highly energetic events. A satisfactory explanation of the stress regime and stress interactions in this region is still debated (Singh et al., 2000).

The overall results indicate that, in general, central México is characterized by a rapid decay of amplitude with distance similar to those in other tectonically active region as Italy.

5.3 Future Directions

Mapping earthquake damage potential is imprecise. It requires knowledge of the quantitative ground motion expectations, and many subjective interpretations about costs and intensities. It also requires a complete catalog and some geophysical interpretations about maximum magnitudes on active faults. Some critical assumptions about earthquake process have to be considered:

- Propagation of seismic waves in deep soils

- Maximum magnitude earthquake for central México and the TMVB

- Spectral scaling of earthquakes

- Regional seismic wave propagation

- Complete study of the Mexican earthquake catalog

Deep soil deposits are common in the Basin of México. The effect of the deep soil is the result of two competing effects: low material strength

that will increase the surface motion but the greater thickness of the soil column also absorbs more energy. Herrmann (personal communication) has included the effect of deep soils in probabilistic seismic hazard maps as an effort to predict earthquake ground motion parameters in a more realistic manner.

Regional seismic wave propagation was studied in this dissertation. In future studies it will be important to study the coastal events. Previous studies (Ordaz and Singh, 1993) did not consider stations within the TMVB, and I would like to compare the propagation of the coastal events from the inland ones.

Zuñiga et al. (1998) have investigated the earthquake catalog in order to asses the seismic hazard in México. The minimum magnitude for completeness is M 4.3. Most of the events are shallow (depth <50 km) and those from the subduction zone.

On the basis of recent experience in estimating seismic hazard maps for the central United States (Herrmann et al. 1999), I prefer to include the historical seismicity using a spatially-smoothed model (Frankel, 1995). This approach seems to be appropriate for reducing the subjective judgments involved in selecting seismic sources, especially in regions where low seismicity is common. His procedure is focused toward constructing the hazard maps directly from the historic seismicity. The maximum likelihood of the a-values is defined as the number of events greater than the minimum magnitude within a grid. This value is smoothed and used directly to estimate the annual rate of exceeding ground motion at a specific site. The probabilistic seismic hazard maps are very sensitive to the time recurrence of major earthquakes, completeness of the earthquake catalog,

source spectra models and maximum magnitudes. All of these parameters need to be refined for a good estimation of the seismic hazard.

I should note an important observation from this study. The attenuation relations not only depend on the specific characteristics of the region (tectonic environment, fluid content, heat flow, etc.) but also depend on the source characteristics and propagation paths (focal mechanisms, distance from the source, etc.). This should be an important consideration for seismic hazard evaluation. The classical approach of probabilistic hazard assessment only considers a single attenuation relation for a given region. It is more appropriate, however, to consider different source, propagation, and site characteristics, and whether is necessary or not, different attenuation relations for a single site. For example, in the case of central México, the events within the TMVB are more likely to propagate according to the attenuation relation estimated in this study, but the seismic waves of the events from the coast may propagate with less attenuation.

5.4   Final remarks

The regional attenuation of earthquake ground motion was calculated in central México using data from two different networks, RSVM and BB, with epicentral distance in the range of 2 - 250 km. I found that the coda normalization technique provides an estimate of the propagation functional for distances greater than the cross-over distance, but it fails for deep earthquakes, especially at short distances. I measured the average attenuation of S and Lg waves to estimate a geometrical spreading

$$g(r) = \begin{cases} r^{-1.3} & r \leq 40 \, km \\ r^{-0.5} & r \geq 40 \, km \end{cases}$$

and the anelastic attenuation functional $Q(f) = 88\,f^{0.73}$. A second model may also be considered with a $g(r)$ of

$$g(r) = \left\{ \begin{array}{ll} r^{-1} & r \leq 180\,km \\ r^{-0.5} & r \geq 180\,km \end{array} \right.$$

and the $Q(f) = 220\,f^{0.66}$. Preference is given to the second model because it better predicts the high excitation levels of the large earthquakes. (Figures 4.5 to 4.8).

The results of this study indicate that low-frequency signals have longer durations than the high-frequency ones. Low-frequency vibrations are of particular importance for México City, where severe damage appears to be related to the ground motion at about 0.5 Hz for coastal events, however the attenuation relations for these events seem are different than those for inland events within central México. The attenuation at low frequencies (0.7 Hz) seems to be higher than other parts of the world at the same frequencies. If this is correct, I can explain the high attenuation of the seismic waves for some earthquakes in this region, especially for the intermediate depth ones. Independent studies are needed to provide κ, $\Delta\sigma$ and source spectral parameters. I estimated a preliminary $\kappa = 0.04$, by modeling small earthquakes with a stress drop of 70 bars. Intermediate depth and shallow earthquakes are considered in the regression analysis.

Many different regions in the world have similar tectonic environments and propagation characteristics. One example is the Cascadia zone in the northwest of the continental United States. Studies in regions with environments similar to central México may help to understand better the wave propagation characteristics in México by analogy.

Central México is currently characterized by a low rate of earthquake

activity. A sufficient number of strong ground motion recordings do not exist to define strong ground motion scaling relations, however abundant vertical component waveforms from small earthquakes may provide an initial estimation of the attenuation relations.

This study has demonstrated that the background seismicity of an active region can be used to estimate the predictive relations for large earthquakes, even though validation are not complete. Other regions in México (Chiapas, Oaxaca or Jalisco), should be studied in the same level of detail.

Finally future seismic hazard research is strongly recommended to focus on deep soil effects, maximum magnitudes and spectral scaling relations.

Appendix A. Random Vibration Theory

A simplified analytic form for predicting peak amplitude from the rms acceleration has been published by Boore (1983), and its derivation is repeated here.

Hanks and McGuire (1981) used the following equation based on random vibration theory to predict the peak acceleration from the rms acceleration

$$\frac{a_{peak}}{a_{RMS}} = [2ln(N)]^{1/2}$$

N is the number of extrema in a time interval T. For stationary time series

$$N = 2f_c T$$

where f_c, is the central frequency. Note that the constant 2 is due to the fact that two extrema are present in each cycle of motion.

Cartwright and Longuet-Higgins (1959) demonstrated that the expression above is an approximation valid for large N. In general

$$\frac{a_{peak}}{a_{RMS}} = \eta_{max}$$

where

$$\eta_{max} = \int_{-\infty}^{+\infty} \eta \frac{d}{d\eta} [1 - q(\eta)]^N$$

$q(\eta)$ is the cumulative probability of η exceeding a given value, η_{max} is the expected peak value for the time history. N depends on the spectral moments, as well as the probability distribution of the peaks does. Separating this integral into two parts, from $-\infty$ to 0 and from 0 to ∞ and integrating

by parts

$$\eta_{max} = \int_{-\infty}^{0} [1 - q(\eta)]^N \, d\eta + \int_{0}^{\infty} \left\{ 1 - [1 - q(\eta)]^N \right\} d\eta$$

when N is large $[1 - q(\eta)]^N$ is very small unless q is of order $1/N$. This integral is easily solved numerically, neglecting the terms of order $(lnN)^{1/2}$. Cartwright and Longuet-Higgins (1959, equation 6.7) expressed $q(\eta)$ as

$$q(\eta) = (1 - \varepsilon^2)^{1/2} e^{-\theta}$$

where $\theta = \frac{1}{2}\eta^2$, and $\varepsilon^2 = \frac{m_o m_4 - m_2^2}{m_o m_4}$. The probability distribution of the peaks is

$$p(\eta) = \frac{d}{d\eta} [1 - q(\eta)]^N$$

Boore (1983) expanded the integrand of the integral by binomial series and integrated term by term

$$\eta_{max} = \sqrt{\frac{\pi}{2}} \sum_{l=1}^{n} (-1)^{l-1} \frac{C_l^N}{\sqrt{l}} \xi^l$$

where C_l^N are binomial coefficients and ξ is a measure of the bandwidth of the spectrum given by

$$\xi = m_2/(m_o m_4)^{1/2}$$

At any choice of η_{max}, spectral moments are required

$$m_k = \frac{1}{\pi} \int_{0}^{\infty} \omega^k |A(\omega)|^2 \, d\omega$$

The spectral moments can also be used to estimate the dominant frequency of peaks in a time history and consequently N, the number of extrema

$$f_p = \frac{1}{2\pi} \left(m_4/m_2 \right)^{\frac{1}{2}}$$

$$N = 2T \frac{1}{2\pi} \left(m_4/m_2 \right)^{\frac{1}{2}}$$

and

$$a_{RMS} = \left(\frac{m_0}{T} \right)^{\frac{1}{2}}$$

From the above equations we have shown that after choosing the duration T, the relation between maximum amplitudes and rms amplitudes depends only on the spectral moments of the ground motion spectrum. within the duration window. These relations can be applied to the ground velocity, acceleration or response spectra by converting the displacement spectrum to velocity or acceleration. In the case of response spectra for lightly damped oscillations, care must be taken with the duration used (Joyner and Boore, 1983)

Appendix B. Calibration of the RSVM seismic network

A reliable seismic network requires a good selection of sites, calibration and data storage. For a seismic hazard assessment, a calibrated network is essential to estimate the predictive relationships. The instrument calibration consists of defining the damping constants and characteristic frequencies of the sensor and the electronics as poles and zeroes in the Laplace domain, which are polynomial roots of the transfer function. The short period network (1.0 Hz) in the Valley of México is operated by the "Instituto de Geofisica, UNAM". This permanent network was designed to study the seismicity in the region and is the main source of data for this study. Thus a detailed instrument calibration is needed. The data available have been recorded since 1994.

The theoretical poles and zeroes were calculated for two cases: Lennartz sensors with low-pass filter of 10 Hz and gain of 4 and the same sensor with a 5 Hz and gain of 20.

The SEED response files for both cases are:

LENNARTZ 10 Hz
B053F03 Transfer function type: A [Laplace Transform (Rad/sec)]
B053F04 Stage sequence number: 1
B053F05 Response in units lookup: M/S - velocity
B053F06 Response out units lookup: V - volts
B053F07 A0 normalization factor: 1.376710e+09
B053F08 Normalization frequency: 1.000000e00
B053F09 Number of zeroes: 2
B053F14 Number of poles: 7 # Complex zeroes: # i real imag real_error imag_error
B053F10-13 0 0.000000e+00 0.000000e+00 0.000000E+00 0.000000E+0
B053F10-13 1 0.000000e+00 0.000000e+00 0.000000E+00 0.000000E+0
Complex poles: # i real imag real_error imag_error
B053F15-18 0 -6.280000e+01 0.000000e+00 0.000000E+00 0.000000E+00
B053F15-18 1 -4.398000e+01 4.487320e+01 0.000000E+00 0.000000E+00
B053F15-18 2 -4.398000e+01 -4.487320e+01 0.000000E+00 0.000000E+00
B053F15-18 3 -4.398000e+01 4.487320e+01 0.000000E+00 0.000000E+00
B053F15-18 4 -4.398000e+01 -4.487320e+01 0.000000E+00 0.000000E+00
B053F15-18 5 -4.398260e+00 4.487120e+00 0.000000E+00 0.000000E+00
B053F15-18 6 -4.398260e+00 -4.487120e+00 0.000000E+00 0.000000E+00
Gain STAGE
B058F03 Stage sequence number: 1
B058F04 Gain: 3.2768E+08
B058F05 Frequency of gain: 1.000000E+00 HZ
B058F06 Number of calibrations: 0

LENNARTZ 5 Hz
B053F03 Transfer function type: A [Laplace Transform (Rad/sec)]
B053F04 Stage sequence number: 1
B053F05 Response in units lookup: M/S - velocity
B053F06 Response out units lookup: V - volts
B053F07 A0 normalization factor: 4.369650e+07
B053F08 Normalization frequency: 1.000000e00
B053F09 Number of zeroes: 2
B053F14 Number of poles: 7
Complex zeroes:
i real imag real_error imag_error
B053F10-13 0 0.000000e+00 0.000000e+00 0.000000E+00 0.000000E+0
B053F10-13 1 0.000000e+00 0.000000e+00 0.000000E+00 0.000000E+0
Complex poles:
i real imag real_error imag_error
B053F15-18 0 -3.142000e+01 0.000000e+00 0.000000E+00 0.000000E+00
B053F15-18 1 -2.199000e+01 2.243657e+01 0.000000E+00 0.000000E+00
B053F15-18 2 -2.199000e+01 -2.243657e+01 0.000000E+00 0.000000E+00
B053F15-18 3 -2.199000e+01 2.243657e+01 0.000000E+00 0.000000E+00
B053F15-18 4 -2.199000e+01 -2.243657e+01 0.000000E+00 0.000000E+00
B053F15-18 5 -4.398260e+00 4.487120e+00 0.000000E+00 0.000000E+00
B053F15-18 6 -4.398260e+00 -4.487120e+00 0.000000E+00 0.000000E+00
Gain STAGE
This Stage is usually ONE and will be added to a GAIN-ONLY later
B058F03 Stage sequence number: 1
B058F04 Gain: 1.31072E+08
B058F05 Frequency of gain: 1.000000E+00 HZ
B058F06 Number of calibrations: 0

The gain factors were estimated as follow:

$$(Preamp) \times (A/D) \times (Sensitivity) \times (Scale)$$

For the Lennartz 10 Hz:

$$5 \times 4096/5 \times 400 \times 200 = 3.2768E + 08 \; counts/m/s$$

and for the Lennartz 5 Hz:

$$20 \times 4096/5 \times 400 \times 200 = 1.31072E + 08 \; counts/m/s$$

The $(Preamp)$ is the gain from the sensor to the A/D converter. The (A/D) is the digitizer conversion factor in *counts/volts*. The nominal sensitivity is 400 volts/m/s. The side factor is required since the digital data stream from the field is transmitted in a floating point format. The scale factor converts the field floating point value to a true integer representation of the voltage.

The station CUVM consists of a temporal Lennartz sensor connected to the GEOS digitizer. During the period October - December, 1998, CUVM was operating with a Lennartz 5Hz. On the same seismic pier, an STS-1 from the BB network is connected. Figure 5.9 compares a CUVM recording with the BB for an event occurred on October 8, 1998, after converting the CUIG recording into a CUVM instrument. This exercise validated the CUVM response.

A similar analysis was done to the L-4 Mark sensors. The response files are:
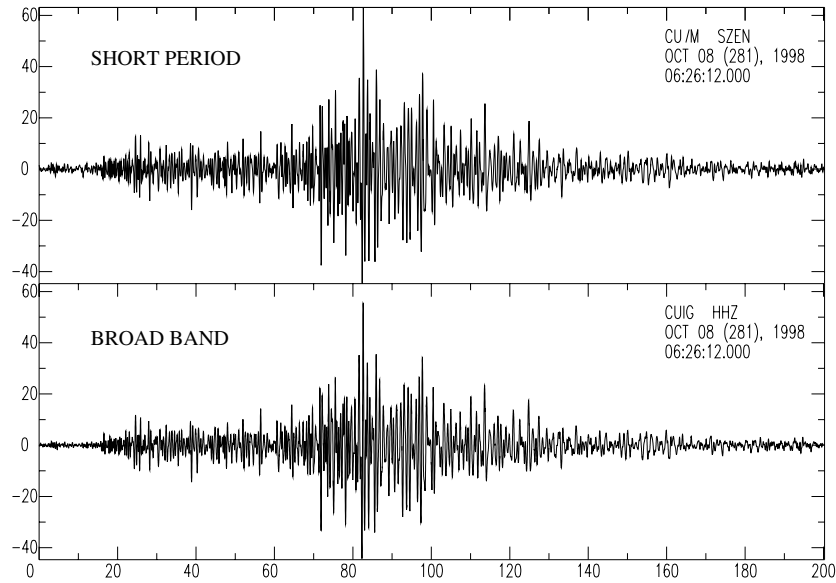
Figure 5.9: Comparison between the CUVM RSVM station and CUIG BB station. Units are in counts, the CUIG is transformed into a CUVM convolving the instrument response, and filtered from 0.25 to 3 Hz.

```
MARK L-4 10 Hz
B053F03 Transfer function type: A [Laplace Transform (Rad/sec)]
B053F04 Stage sequence number: 1
B053F05 Response in units lookup: M/S - velocity
B053F06 Response out units lookup: V - volts
B053F07 A0 normalization factor: 1.376710e+09
B053F08 Normalization frequency: 1.000000e00
B053F09 Number of zeroes: 2 B053F14 Number of poles: 7
# Complex zeroes: # i real imag real_error imag_error
B053F10-13 0 0.000000e+00 0.000000e+00 0.000000E+00 0.000000E+0
B053F10-13 1 0.000000e+00 0.000000e+00 0.000000E+00 0.000000E+0
# Complex poles:
# i real imag real_error imag_error
B053F15-18 0 -6.280000e+01 0.000000e+00 0.000000E+00 0.000000E+00
B053F15-18 1 -4.398000e+01 4.487320e+01 0.000000E+00 0.000000E+00
B053F15-18 2 -4.398000e+01 -4.487320e+01 0.000000E+00 0.000000E+00
B053F15-18 3 -4.398000e+01 4.487320e+01 0.000000E+00 0.000000E+00
B053F15-18 4 -4.398000e+01 -4.487320e+01 0.000000E+00 0.000000E+00
B053F15-18 5 -4.398260e+00 4.487120e+00 0.000000E+00 0.000000E+00
B053F15-18 6 -4.398260e+00 -4.487120e+00 0.000000E+00 0.000000E+00
# Gain STAGE
B058F03 Stage sequence number: 1
B058F04 Gain: 2.830110E+08
B058F05 Frequency of gain: 1.000000E+00 HZ
B058F06 Number of calibrations: 0
```

```
Mark L-4 5 Hz
B053F03 Transfer function type: A [Laplace Transform (Rad/sec)]
B053F04 Stage sequence number: 1
B053F05 Response in units lookup: M/S - velocity
B053F06 Response out units lookup: V - volts
B053F07 A0 normalization factor: 4.369650e+07
B053F08 Normalization frequency: 1.000000e00
B053F09 Number of zeroes: 2
B053F14 Number of poles: 7
# Complex zeroes:
# i real imag real_error imag_error
B053F10-13 0 0.000000e+00 0.000000e+00 0.000000E+00 0.000000E+0
B053F10-13 1 0.000000e+00 0.000000e+00 0.000000E+00 0.000000E+0
# Complex poles:
# i real imag real_error imag_error
B053F15-18 0 -3.142000e+01 0.000000e+00 0.000000E+00 0.000000E+00
B053F15-18 1 -2.199000e+01 2.243657e+01 0.000000E+00 0.000000E+00
B053F15-18 2 -2.199000e+01 -2.243657e+01 0.000000E+00 0.000000E+00
B053F15-18 3 -2.199000e+01 2.243657e+01 0.000000E+00 0.000000E+00
B053F15-18 4 -2.199000e+01 -2.243657e+01 0.000000E+00 0.000000E+00
B053F15-18 5 -4.398260e+00 4.487120e+00 0.000000E+00 0.000000E+00
B053F15-18 6 -4.398260e+00 -4.487120e+00 0.000000E+00 0.000000E+00
# Gain STAGE
B058F03 Stage sequence number: 1
B058F04 Gain: 6.553600E+08
B058F05 Frequency of gain: 1.000000E+00 HZ
B058F06 Number of calibrations:
```

Figures 5.10 and 5.11 show the magnification curves for the instrument response of the Mark L-4 at 5 an 10 Hz respectively. The figures 5.12 and 5.13 present curves similar for the Lennartz seismometers.
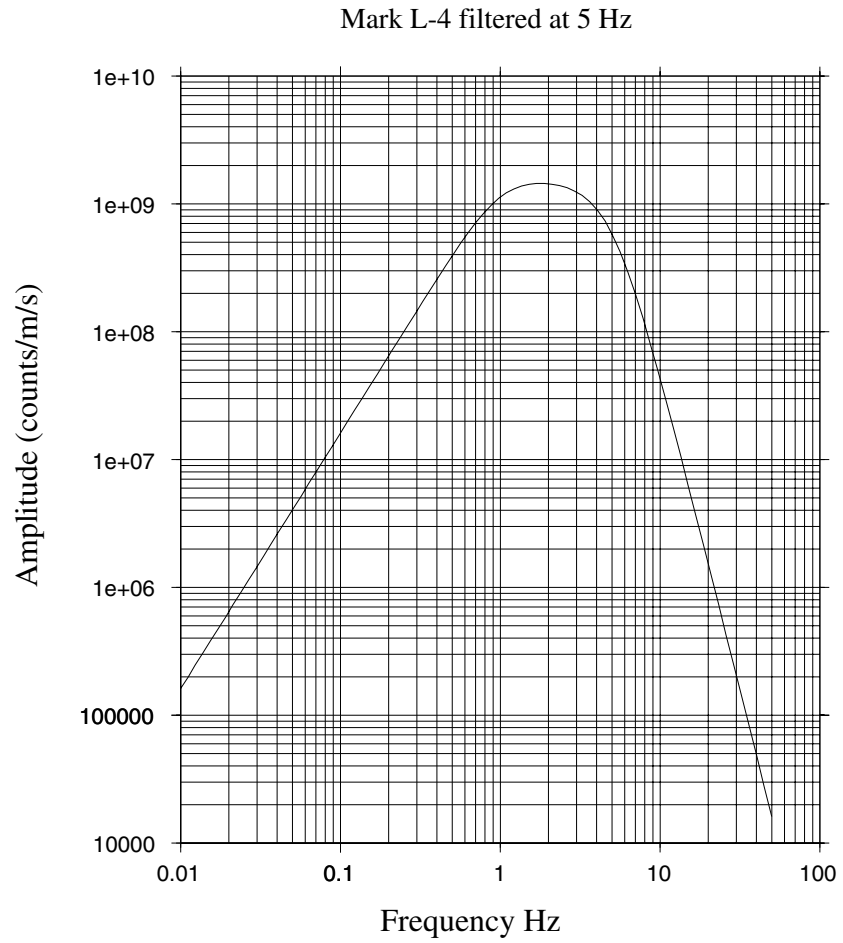
Figure 5.10: Magnification curve for the Mark L-4 filtered at 5 Hz.

Mark L-4 filtered at 10 Hz
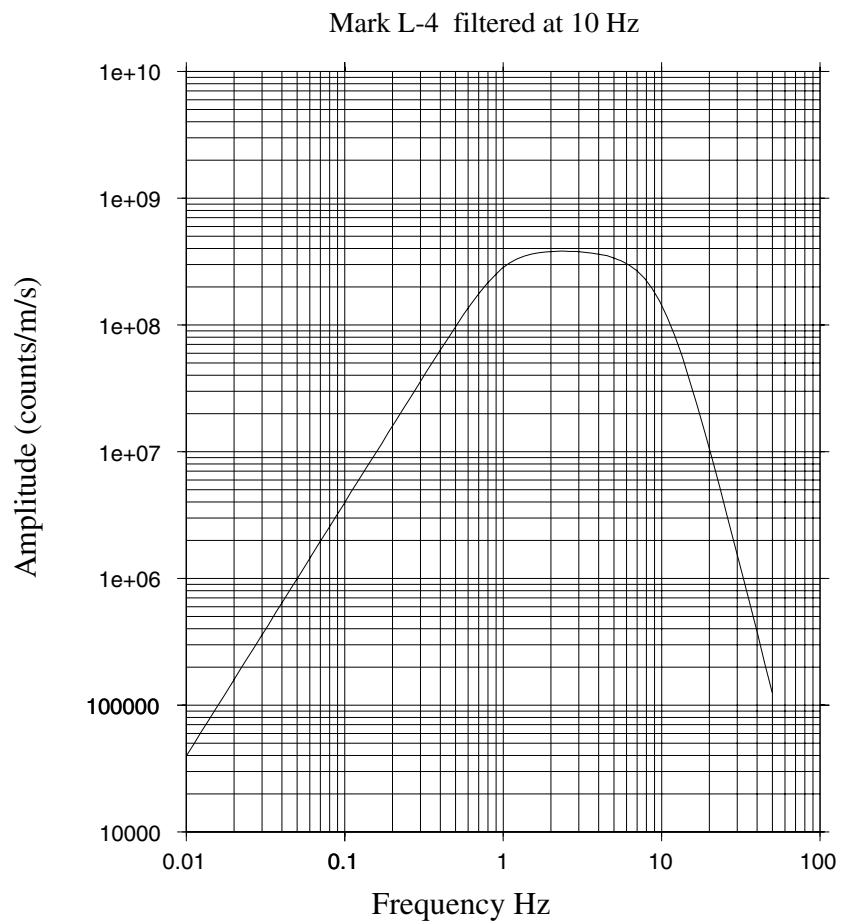
Figure 5.11: Magnification curve for the Mark L-4 filtered at 10 Hz.
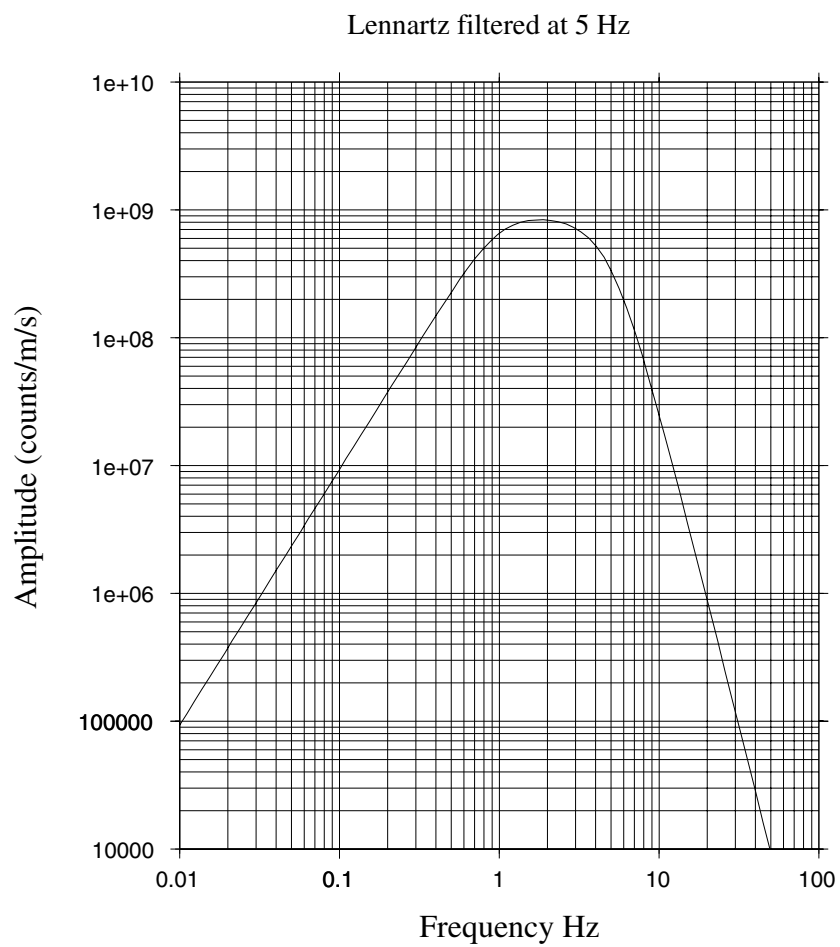
Figure 5.12: Magnification curve for the Lennartz filtered at 5 Hz.

Lennartz filtered at 10 Hz
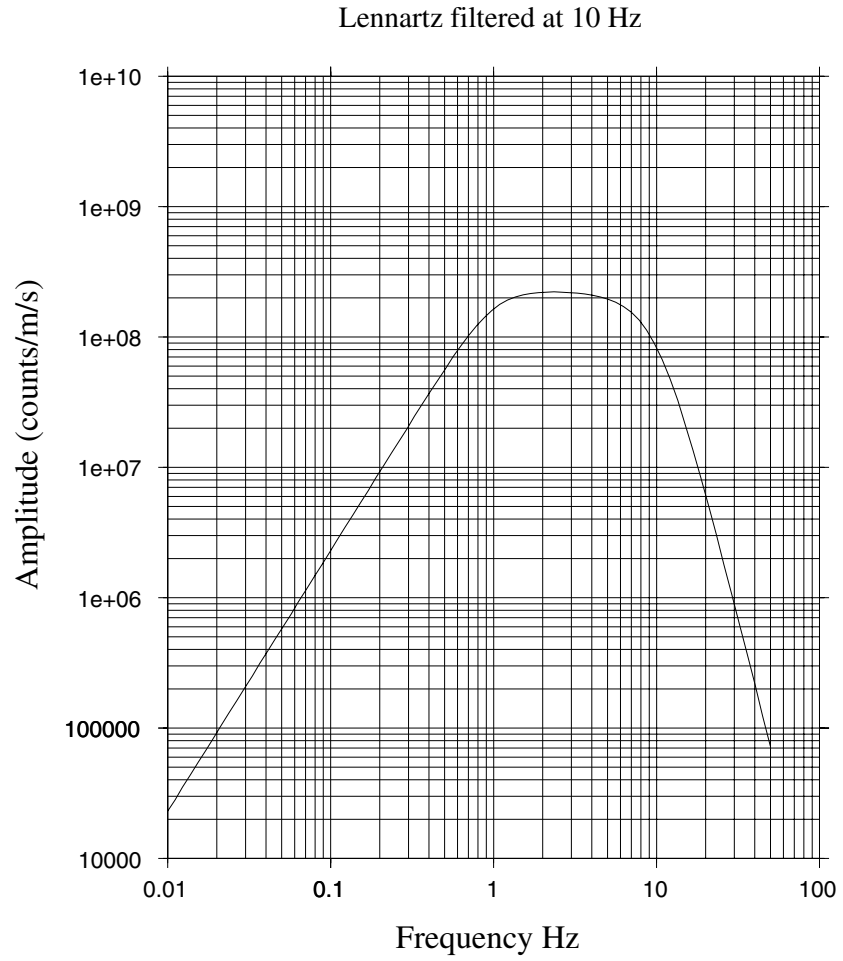
Figure 5.13: Magnification curve for the Lennartz filtered at 10 Hz.

Appendix C. Seismic Hazard in Central México

Seismic hazard analysis can be approached in two different ways: deterministically and probabilistically. In the deterministic approach, one seismic scenario is assumed and some ground motion parameters (for example peak acceleration or peak spectral amplitude of the response spectra) are predicted. The deterministic seismic hazard analysis (DHA) is very common for studying nuclear power plants or large dams, DHA is an easy way to evaluate the worst-case ground motion, however, it provides no information of the uncertainties in earthquakes size, location and time recurrence.

In the Valley of México, the most common study has been a deterministic hazard analysis, usually using large west coast earthquake for design. Using the information available, the critical cases for ground motion have been estimated, the dynamic amplification in the lake bed has been predicted by modeling shear wave propagation in alluvial valleys. For each geotechnical zone (lake-bed, transition, hill-zone) a seismic design spectra has been proposed (Perez-Rocha et al., 1997).

Critical facilities must be safer than residential buildings. After the tremendous experience of the Michoacán earthquake, the México City inhabitants found that a major hospital system collapsed (the "Centro Médico") in addition to the main communication building ("SCT"). The enormous impact of losing critical facilities is a main concern of the population. An example was the striking rescue of the new-born babies in the "Centro Médico". Power plants, dams, transportation networks, bridges, critical

governmental offices and defense facilities are more examples of critical structures, as well as the industrial areas of strategic importance for the economy of the region. In essence, new regulations are needed in order to define critical facilities.

The second approach for studying the seismic hazard is the probabilistic seismic hazard analysis (PHA) that provides a tool for quantifying the uncertainties. A proper probabilistic seismic hazard analysis requires a careful study of the source parameters. In addition the study of distribution of earthquakes size for each specific region is needed, and the distribution of earthquakes with time, and their probability density distribution is required.

A four step procedure to evaluate the probabilistic seismic hazard (Kramer, 1996):

1. Identification and characterization of earthquake sources. In most cases uniform probability distribution is assumed. This distribution is combined with the source geometry to obtain the probability distribution of source-to-site distance.

2. Seismicity of temporal distribution of earthquake recurrence. This is known as the *recurrence relationship*, which specifies the average rate at which an earthquake of some size will be exceeded.

3. The ground motion prediction at the site. This *predictive relationship* is estimated by a regression analysis of recorded earthquakes.

4. The uncertainties in earthquake location, earthquake size and ground motion parameter prediction are combined to obtain the probability

that the ground motion parameter will be exceeded during a particular time period.

The geometry of earthquakes sources is an important consideration. This geometry depends on the tectonic processes. The traditional approach using area-source zones defined in seismo-tectonic provinces was modified by Frankel (1995). The definition of seismo-tectonic provinces has some level of subjective evaluation, not only in the size, shape and location of the regions, but also in the statistical parameters needed to define its probability density distribution. Instead of defining different seismo-tectonic provinces, Frankel (1995) used a different approach taking into account only the seismicity. The new model is based on historical seismicity that will be spatially-smoothed to different length scales. The number of earthquakes n_i with magnitude greater than m_{ref} in each cell i is counted. This number represents the maximum likelihood estimate of 10^a for that cell and is smoothed spatially by multiplying by a Gaussian function.

For each cell i the smoothed value $\widetilde{n}$ is obtained from

$$\widetilde{n}_i = \frac{\sum_j n_j exp\left(-\Delta_{ij}^2/c^2\right)}{\sum_j exp\left(-\Delta_{ij}^2/c^2\right)} \tag{5.6}$$

In this equation Δ_{ij} is the distance between the ith and jth cells, and c is the correlation distance.

The values of $\widetilde{n}_i$ are binned by the distance for each site, so that N_k denotes the total of $\widetilde{n}_i$ values for cells within a certain distance increment of the site.

For each given site:

$$(10^a)_k = N_k/T \tag{5.7}$$

where *k* is the index for the distance and T is the time in years of the earthquake catalog used to determine N_k.

Gutenberg and Richter (1954) found an expression of the mean rate of exceedance at different magnitudes λ_m, when the maximum magnitude m_{max} is known then the mean annual rate of exceedance can be expressed as

$$\lambda_m = 10^{(a-b(m_{max}-m_o))} \tag{5.8}$$

Where b is obtained by a regression of the seismicity database, m_o is the minimum magnitude in which the catalog is complete.

Probabilistic seismic hazard maps have been proposed since 1970 (Esteva, 1970) for Mexico. More recent versions have been developed in 1993 by the national electric commission (CFE, Comisión Federal de Electricidad) and by the Instituto Panamericano de Geografía e Historia (IPGH) in 1998 (Zuñiga et al., 1998). As noted by Ordaz (1997), the seismic hazard in México requires more integrated studies from the Earth scientists. A more detailed study of the fault systems is needed since they are currently characterized in a very rough manner. A systematic research in this field is needed, refining the previous models, and publishing continuously new hazard map versions on a routine basis.

Adding new ground motion data helps the prediction of the ground motion parameters by refining attenuation and spectral source scaling relations. Some of these models may be included in a logic tree fashion. The

logic tree provides a mechanism for using alternative models, with each one assigned a weighting factor (Coppersmith and Youngs, 1986). Thus, any new attempt to improve the knowledge of the ground motion attenuation relations can be easily added.

The seismic catalog has been studied by Zuñiga et al. (1998) including homogeneity and completeness. The most important sources for the instrumental catalog were

- The catalog of the International Seismological Center (ISC) for the period 1898 to December 1990. This is the reference catalog.

- The catalog of the United States Geological Survey (USGS) known as PDE for the period 1898 to December 1990.

- The catalog of the Instituto de Geofísica, UNAM for the period 1899-1991.

The catalog resulting from the analysis was the basis for defining seismotectonic regions. These regions were used to provide the seismicity estimates, maximum magnitudes and focal mechanisms or fault patterns. Figure 5.14 shows the earthquake location from the Mexican catalog compiled by Zuñiga et al. (1998).

Some seismotectonic regions in the north of the country are considered as an extension of other tectonic provinces of the United States, as is the case of the Fisura del Rio Bravo y Cuencas y Sierras province that is considered the extension of the Basin and Range province. This region is of particular importance because of the Bavispe, Sonora earthquake occurred on May 3, 1887, with estimated magnitude of 7.5 (Natali and Sbar, 1987).
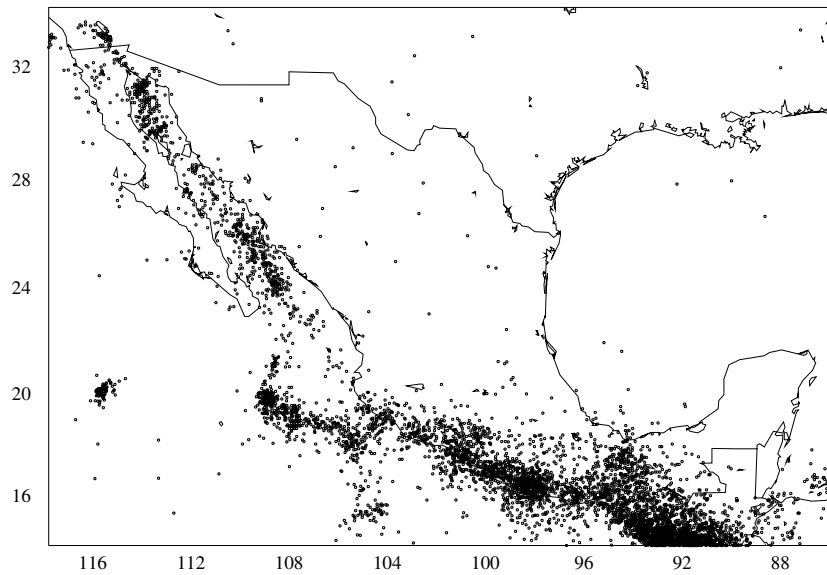
Figure 5.14: Seismicity from 1900 to 1994. The minimum magnitude is $M_s < 4.3$ in which the catalog is complete.

A similar event would have caused considerable damage to the cities of Chihuahua, Ciudad Juarez, Hermosillo, El Paso and Phoenix. This event is one of the largest intraplate earthquake that occurred in North America. The Cuenca de Burgos in the northeast including the states of Coahuila, San Luis Potosi, Nuevo Leon and Zacatecas have low magnitude events; unfortunately there is very little information about earthquakes in this region. Other regions (subduction zones or the Trans Mexican Volcanic Belt) have been studied in more detail. The seismotectonic regions were proposed using all the information about the general characteristics of the earthquakes in the country, considering the potential destructive of the past events (Zuñiga, 1998). Figure 5.15 shows the different seismotectonic regions proposed for the seismic hazard assessment in México.

The attenuation relations used previously for estimating the seismic hazard have considered three different cases: coastal, deep and shallow
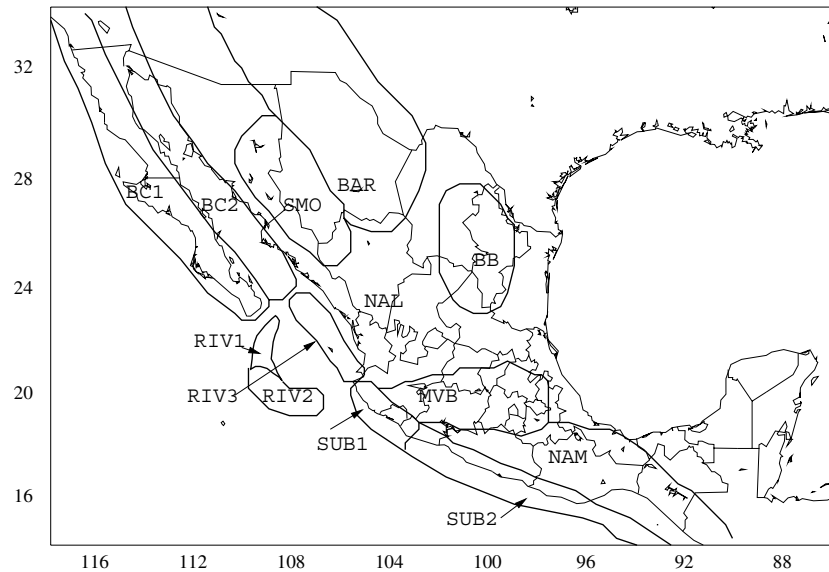
Figure 5.15: Seismotectonic regions proposed for seismic hazard assessment by Zuñiga et al. (1997). BC1, intraplate events (Pacific), Baja California Peninusula. BC2, interplate events (Pacific-North America), Baja California Peninusula. BAR, shallow intraplate events (North America) Cuencas y Sierras y Fisura del Rio Bravo (Basin and Range-Rio Grande Rift). SMO, intraplate shallow events (North America), Sierra Madre Occidental province. BB, intraplate shallow events (North America), Burgos Basin. RIV1, interplate shallow events (Pacific-Rivera), RIV2, interplate strike-slip shallow events (Pacific-Rivera). RIV3, interplate subduction events (Rivera-North America). SUB1, interplate subduction events (Rivera-Cocos-North America). SUB2, interplate subduction events(Cocos-North America). MVB, intraplate shallow events (Trans Mexican Volcanic Belt). NAM, intraplate shallow events (North America).

events. Each of these attenuation relations are represented by different source and propagation models. The coastal earthquakes used the attenuation parameters proposed by Ordaz and Singh (1992) with a finite source model proposed by Singh et al. (1989) and constraints that permit accurately predicting the far field acceleration maxima. The attenuation relation used for the deep earthquakes was similar to the coastal one but used an ω^2 spectral source model using a $\Delta\sigma = 200$ bar. For shallow earthquakes the predictive relation was that proposed by Joyner and Boore (1981) for the California region, applied here primarily to Baja California.

Future revisions of the hazard maps should consider different attenuation relations depending on the tectonic environments, some studies for the north of the country can be modified by using newer scaling relations for the United States, e.g. for the Basin and Ranges province, and other regions require more detailed studies (e.g. the Burgos Basin). Studies on paleoseismicity can contribute significatively to the uncertainties about recurrence period of important earthquakes in México, such as the Bavispe, Sonora earthquake, and assist in refining source zones and maximum magnitudes.

In spite of its history of destructive earthquakes, hazard mapping for much of México faces the same problems as eastern North America, relatively low seismicity rates and little data upon which to base ground motion scaling relations, and also the need to consider the rare, but significant earthquakes. Hazard mapping must periodically be reviewed and updated.

Bibliography

Aki, K. (1968). Seismic displacements near a fault. *J. Geophys. Res.* **73**, 5359-5357.

Aki, K. (1969). Analysis of seismic coda of local earthquakes as scattered waves. *J. Geophys. Res.* **74**, 615-631.

Aki, K. and B. Chouet (1975). Origin of coda waves: source, attenuation and scattering effects. *J. Geophys. Res.* **80**, 3322-3342.

Aki, K. (1980). Attenuation of shear waves in the lithosphere for frequencies from 0.05 to 25 Hz. *Phys. Earth Planet. Inter.*, **21**, 50-60.

Anderson, J. G., J. N. Brune, J. Prince, R. Quaas, S. K. Singh, D. Almora, P. Bodin, M. Oñate, R. Vasquez and J. M. Velasco (1994). The Guerrero accelerograph network. *Geofis. Int.* **33**, 341-372.

Anderson, J. G., and Y. Lei (1994). Non-parametric description of Peak acceleration as a function of magnitude, distance and site in Guerreo México. *Bull. Seism. Soc. Am.*, **84**, 1003-1017.

Anderson, J. G., and S. E. Hough (1984). A model of the shape of the Fourier amplitude spectrum of acceleration at high frequencies. *Bull. Seism. Soc. Am.*, **74**, 1969-1994.

Astiz, L. (1980). Sismicidad en Acambay, Estado de México. El temblor del 22 de febrero de 1979. B. S. Thesis, 130 pp., UNAM, México D.F.

Atkinson, G. M., and D. M. Boore (1995). New ground motion relations for Eastern North America. *Bull. Seism. Soc. Am.*, **85**, 17-30.

Atkinson, G. M., and W. Silva (1997). An empirical study of earthquake source spectra for California earthquakes. *Bull. Seism. Soc. Am.*, **87**, 97-1137.

Atkinson, G. M., and D. M. Boore (1998). Evaluation of models for earthquake source spectra in eastern North America. *Bull. Seism. Soc. Am.*, **88**, 917-934.

Bard, P. Y., and M. Bouchon (1985). The two-dimensional resonance of sediment-filled valleys. *Bull. Seism. Soc. Am.*, **75**, 519-541.

Bard, P. Y., M. Campillo, F. J. Chavez-Garcia and F. J. Sanchez Sesma (1988). A theoretical investigation of large and small scale amplification effects in México City Valley. *Earth. Spectra*, **4**, 609-633.

Bard, P. Y., and F. J. Chavez-Garcia (1993). On the decoupling of surficial sediments from surrounding geology at México City. *Bull. Seism. Soc. Am.*, **83**, 1979-1991.

Barker, J. S., M. Campillo, F. J. Sanchez-Sesma, D. Hongmansand and S. K. Singh (1996). Analysis of wave propagation in the Valley of México from a dense array of seismometers. *Bull. Seism. Soc. Am.*, **80**, 2261-2281.

Beresnev, I. A. and G. M. Atkinson (1997). Modeling finite-fault radiation from the ω^n spectrum. *Bull. Seism. Soc. Am.* **87**, 67-84.

Boore, D. M. (1973). The effect of simple topography on seismic waves: amplifications for accelerations recorded at Pacoima Dam, San Fernando Valley. *Bull. Seism. Soc. Am.*, **63**, 1603-1609.

Boore, D. M. (1983). Stochastic simulation of high frequency ground motions based on seismological models of the radiated spectra. *Bull. Seism. Soc.*, **73**, 1865-1894.

Boore, D. M., and W. B. Joyner (1991). Estimation of ground motion at deep soil sites in eastern North America. *Bull. Seism. Soc. Am.*, **81**, 327-341.

Boore, D. M., and W. B. Joyner (1997). Site amplifications for generic rock sites. *Bull. Seism. Soc. Am.*, **87**, 327-341.

Borcherdt, R. D. (1970). Effects of local geology on ground motion near San Francisco Bay. *Bull. Seism. Soc. Am.*, **60**, 29-61.

Brune, J. N. (1970). Tectonic stresses and spectra of seismic waves from earthquakes. *J. Geophys. Res.*, **75**, 4997-5009.

Building Seismic Safety Council (BSSC) (1994). NEHRP recommended provisions for seismic regulations for new buildings, Part 1 - Provisions, FEMA 222A, Federal Emergency Management Agency, 290 pp.

Campbell, K. (1981). Near-source attenuation peak horizontal acceleration. *Bull. Seism. Soc. Am.*, **71**, 2039-2070.

Campbell, K. (1997). Empirical near source attenuation relationships for Horizontal and Vertical components of peak ground acceleration, peak velocity, and pseudo-absolute acceleration response spectra. *Seism. Res. Lett.*, **68**, 154-179.

Campa, M. F., and Coney, P. J. (1983) Tectono-stratigraphic terranes and mineral resource distribution in México. *Can. J. Earth. Sci.* **20**, 1040-1051.

Campillo, M., P. Y. Bard, F. Nicollin and F. Sánchez Sésma (1988). The México earthquake of September 19, 1985 - the incident wavefield in México City during the great Michoacán earthquake and its interaction with the deep basin, *Earthq. Spectra*, **4**, 591-608.

Campos, J., M., O. Delgado-Rodríguez and M. Milán (1994). A contribution to the tectonics of the northern portion of the central sector of the Trans-Mexican Volcanic Belt (between Queretaro fracture zone and the Mezquital Valley). *EOS Trans. Am Geophys. Union,* **75**, 733.

Canas, J. A. (1986). Estudio del factor anelástico Q de la coda de los terremotos correspondientes a las regiones central y oriental del eje volcánico de México. *Geofis. Int.*, **25**, 503-520.

Coppersmith, K. J. and R. R. Youngs (1986) Capturing uncertainty in probabilistic seismic hazard assessment with intraplate tectonic environments. *Proceedings, 3rd U.S. National Conference on Eart5hquake Engineering* Charleston, South Carolina, **1**, 301-312.

Cartwright, D. E., and M. S. Longuet-Higgins (1956). The statistical distribution of the maxima of a random function. *Proc. Roy. Soc. London*, **A237**, 212-223.

Castro, R., M. Rodriguez, J. Lermo, S. K. Singh and L. Astiz (1983). Estudio de la sismicidad en la región de Acambay Estado de México. *Reporte I. I. 3710*

Castro R., J. G. Anderson and S. K. Singh (1990). Site response, attenuation and source spectra of S waves along the Guerrero, México, subduction process. *J. Geophys. Res.* **87**, 329-338

Castro R., L. Munguia, C. Rebollar, and J. G. Acosta (1994) A comparative analysis of the quality factor Q for the regions of Guerrero and Oaxaca, México. *Geofis. Intl.*, **33**, 373-383.

Chavez-Garcia, F. J. and P. Y. Bard (1993a) Gravity waves in México City? - I. Gravity perturbed waves in anelastic solid. *Bull. Seism. Soc. Am.* **83**, 1637-1655.

Chavez-Garcia, F. J. and P. Y. Bard (1993b) Gravity waves in México City? - II. Coupling between an anelastic solid and fluid layer. *Bull. Seism. Soc. Am.* **83**, 1656-1675.

Cornell, C. A. (1968) Engineering seismic risk analysis. *Bull. Seism.Soc. Am.,* **58**, 1583-1606.

Esquivel, J. A. and F. J. Sanchez-Sesma (1980) Effects on canyon topography on dynamic soil-bridge interaction for incident SH waves, *Proc. World Conf. Earthquake Eng., 7th,* Instanbul, **2**, 153-160.

Esteva, L. (1970) Regionalización sísmica de México para fines de Ingeniería.*Serie azul del Instituto de Ingeniería*, 246.

Fehler, M., M. Hoshiba, H. Sato and K Obara (1986). Separation of scattering and intrinsic attenuation for the Kanto-Tokai region, Japan, using measurements of S wave energy vs hypocentral distance. *Geophys. J. Int*. **81**, 65-91.

Ferrari, L., V. Garduño, G. Pasquare and A. Tibaldi (1994). Volcanic and tectonic evolution of central México: Oligocene to present. *Geof. Int. ,* **33**, 91-105.

Fäh, D., P. Suhadolc, S. Mueller and G. F. Panza (1994). A hybrid method for the estimation of ground motion in sedimentary basins: quantitative modeling for México City. *Bull. Seism. Soc. Am.,* **84**, 383-399.

Frankel, A., J. McGarr, J. Bicknell, L. Mori, L. Seeber, and E. Cranswick (1990). Attenuation of high-frequency shear waves in the crust; measurements from New York state, South Africa, and southern California. *J. Geophys. Res.,* **95**, 17441-17457.

Frankel, A. (1995). Mapping seismic hazard in the central and eastern United States. *Seism. Res. Lett.,* **66**, 11-21.

Furumura, T. and B. L. Kennett (1998). On the nature of regional seismic phases -III. The influence of crustal heterogeneity on the wavefield for subduction earthquakes: the 1985 Michoacan and 1995 Copala, Guerrero, México earthquakes. *Geophys. J. Int.,* **135**, 1060-1084.

Griffiths, D. W. and G. A. Bollinger (1979). The effect of the Appalachian Mountain topography on seismic waves. *Bull. Seism. Soc. Am.,* **69**, 1081-1105.

Gutenberg B. and C. F. Richter (1954) Seismicity of the Earth and associated phenomena. *Princeton N. J., University Press*, 310 pp.

Hanks, T. C. and R. K. McGuire (1981). The character of high frequency strong ground motion. *Bull. Seim. Soc. Am.,* **71**, 2071-2095.

Harmsen, S. (1997). Estimating the diminution of shear wave amplitude with distance: Application to the Los Angeles, California, Urban Area. *Bull. Seism. Soc. Am.*, **87**, 888 -903.

Herrmann, R. B., A. Akinci and R. Ortega (1999). Probabilistic seismic hazard maps for the Central United States. *Seismological Society of America*, Annual meeting 1999.

Idriss, I. M., and H.B. Seed (1968). An analysis of ground motion during the 1957 San Francisco earthquake. *Bull. Seism. Soc. Am.*, **58**, 2013-2032.

Jeon. Y. S. (2000). High frequency earthquake ground motion scaling in Utah. M. S. Dissertation. *Saint Louis University*.

Johnson, L. R., and W. Silva (1981). The effects of unconsolidated sediments upon the ground motion during local earthquakes. *Bull. Seism. Soc. Am.*, **71**, 127-142.

Johnson, C. A., and C. G. A. Harrison (1989). Tectonics and volcanism in Central México: A Landsat thematic mapper perspective. *Remote Sens. Environ.*, **28**, 273-286.

Joyner, W. B., and D. M. Boore (1981). Peak horizontal acceleration and velocity from strong motion records including records from the 1979 Imperial Valley, California, earthquake. *Bull. Seism. Soc. Am.*, **71**, 2011-2038.

Kawase, H and K. Aki (1989). A study on the response of a soft basin for incident S, P, and Rayleigh waves with special reference to the long duration observed in México City. *Bull. Seism. Soc. Am.*, **79**, 1361-1382.

Klein, F. W., R. Y. Koyonagi, J. S. Nakata and W. R. Tanigawa (1987) The seismicity of Kilauea's magma system. *Geol. Surv. Prof. Pap. (U.S.)*, **1350**, 1019-1185.

Kramer, S. (1996). *Geotechnical earthquake engineering*. Prentice Hall. First edition.

Lay, T. and E. Okal (1983). The Gilbert Islands (Republic of Kiribati) earthquake swarm of 1981-1983. *Phys. Earth Planet. Inter*. **21**, 283-303.

Lay, T. and T. C. Wallace (1995). Modern global seismology. *Academic Press Inc.*

Lermo, J., J. Soto, A. Huidobro, J. Cuenca, H. Mijares, C. Meza and J. Flores (1997) Análisis preliminar de la sismicidad en la cuenca de México y zonas aledañas. *Memor. Nat. Con. Ing. Sism*. 205-215.

Lomnitz C. (1990) México 1985: the case for gravity waves, *Geophys. J. Int.*, **102**, 569-572.

Lomnitz C. (1995) Comments on two articles on gravity waves by Chavez-Garcia and Bard (1993,a,b), *Bull. seism. Soc. Am.* **85**, 1971.

Lomnitz C., J. Flores, O. Novaro, T. H. Seligman and R. Esquivel (1999) Seismic coupling of interface modes in sedimentary basins: A recipe for disaster *Bull. seism. Soc. Am.* **89**, 14-21.

Malagnini, L., R. B. Herrmann and M. Di Bona (2000a). Ground motion scaling in the Apennines (Italy). submitted to *Bull. Seism. Soc. Am.*

Malagnini, L., R. B. Herrmann and K. Koch (2000b). Regional ground motion scaling in Central Europe. submitted to *Bull. Seism. Soc. Am.*

Mateos, J., J. Flores, O. Navarro, J. M. Alvarez-Tostado and T. H. Seligman (1993a) Generation of inhomogeneous P waves in a layered medium. *Tectonophysics*, **218**, 247-256.

Mateos, J., J. Flores, O. Navarro, T. H. Seligman and J. M. Alvarez-Tostado (1993b) Resonant response models for the Valley of México - II. The trapping of horizontal P waves. *Geophys. J. Int.*, **113**, 449-462.

Mayeda, K., S. Koyanagi, M. Hoshiba, K. Aki and Y. Zengh (1992). A comparative study of scattering, intrinsic and coda Q^{-1} for Hawaii, Long Valley and Central California between 1.5 and 15 Hz. *Jour. Geophys. Res.*, **97**, 6643-6659.

Mitchell, B. J. (1995). Anelastic structure and evolution of continental crust and upper mantle from surface wave attenuation. *Rev. Geophys.*, **33**, 441-462.

Moczo, P. and P. Y. Bard (1993). Wave diffraction, amplification and differential motion near strong lateral discontinuities, *Bull. Seism. Soc. Am.*, **83**, 85-106.

Mooser, F. and M. Maldonado (1961). Tectónica penecontemporánea a lo largo de la Costa Mexicana del Oceano Pacífico. *Geofis. Inter.* **1**, 1-20.

Natali, S. G. and M. L. Sbar (1982). Seismicity in the epicentral region of the 1887 northeastern Sonoran earthquake, México.

Bull. Seism. Soc. Am., **72**, 181-196.

Ordaz, M., and S. K. Singh (1992). Source spectra and spectral attenuation of seismic waves from Mexican earthquakes an evidence of amplification in the hill zone of México City. *Bull. Seism. Soc. Am.*, **82**, 24-43.

Ordaz, M. (1997). Sismicidad y Riesgo Sísmico. Sociedad Mexicana de Ingeniería Sísmica. *Memorias del XI congreso nacional*. Veracruz Ver.

Ordaz, M., and C. Reyes (1999). Earthquake hazard in México City: Observations versus computations. *Bull. Seism. Soc. Am.*, **89**, 1379-1383.

Pacheco, J. F., and S. K. Singh (2000). A study of the 1999 Tehuacán, México earthquake (Mw = 7.0): Source characteristics and aftershocks. *SSA spring meeting*.

Pardo, M., and G. Suárez (1995). Shape of the subducted Rivera and Cocos plates in southern México: Seismic and tectonic implications. *J. Geophys. Res.*, **100**, 12357-12373.

Perez-Rocha, L. E., M. Ordaz and E. Angulo (1997). Escenarios de alto riesgo sísmico en la ciudad de México. Sociedad Mexicana de Ingeniería Sísmica. *Memorias del XI congreso nacional*. Veracruz Ver.

Phillips, W. S., and W. H. K. Lee (1988). Spatial variation of crustal coda Q in California. *Pure Appl. Geophys.*, **128**, 251-260.

Raoof, M., R. B. Herrmann, and L. Malagnini (1999). Attenuation and excitation of three component ground motion in Southern California. *Bull. Seism. Soc. Am.*, **89**, 888-902

Rice, S. (1954). *Mathematical Analysis of random noise. Selected papers on noise and stochastic Processes*. Dover Publications N.Y.

Rodríguez, M., J. Lermo, F. Chávez and R. Castro. (1984). El temblor del 7 de Febrero de 1984 en Juchitepec México. *Internal Report. Engineering Institute UNAM*. Proyect 4707.

Rosenbleuth E., and D. Resendiz (1988). Disposiciones reglamentarias de 1987 para tener en cuenta interaccion dinamica suelo estructura. *Series del Instituto de Ingenieria, UNAM*. No 509.

Ruiz, S.E. and L. Esteva (1981) Probabilistic response of multi-support structures on non-uniform soil conditions. *Int. Conf. on Recent Advances in Geotech. Earth. Eng. and Soil Dynamics, St. Louis Missouri*, 1981, **1**, 351-354.

Samiezadé-Yazd, M., R. B. Herrmann, L. Malagnini and W. Liu A regional comparison of vertical ground motion in North America. *Final report. Saint Louis University* USGS grant 1434-94-G2403.

Sanchez-Sesma, F. J. (1987). Site effects on strong ground motion. *Soil and Earth. Engi.,* **6**, 124-131.

Sanchez-Sesma, F. J. and F. Luzon (1996). Can horizontal P waves be trapped and resonate in a shallow sedimentary basin?. *Geophys J. Int,* **124**, 209-214.

Sanchez-Sesma, F. J., S. Chavez-Perez, M. Suarez, M. Bravo and L. E. Perez-Rocha (1988) The México earthquake of September 19, 1985 - on the seismic response of the Valley of México. *Earthq. Spectra,* **4**, 569-589.

Seed, H. B., and I. M. Idriss (1969). Influence of soil conditions on ground motion during earthquakes, *Proc. ASCE*, **95(SM1)**, 99-137.

Shapiro N. M., M. Campillo, A. Paul, S. K. Singh, D. Jongmans and F. J. Sánchez Sésma (1997). Surface wave propagation across the Mexican Volcanic Belt and the origin of the long-period seismic wave amplification in the Valley of México. *Geophys. J. Int.*, **128**, 151-166.

Singh, S. K., E. Mena, and R. Castro (1988). Some aspects of source characteristics of the 19 September 1985 Michoacan earthquake and ground motion amplification in and near Mexico City from strong motion data. *Bull. Seism. Soc. Am.*, **78**, 451-477.

Singh, S. K. and M. Ordaz (1993). On the origin of long coda observedin the lake-bed strong-motion records of México City. *Bull. Seism. Soc. Am.*, **83**, 1298-1306.

Singh, S. K., R. Quass, F. Mooser, D. Almora, M. Torres, and R. Vázquez (1995). Is there truly a hard rock site in the Valley of México? *Geophys. Res. Lett.*, **22**, 481-484.

Singh, S. K., M. Ordaz, J. F. Pacheco, R. Quaas, L. Alcántara, S. Alcocer, C. Gutierrez, R. Meli and E. Ovando (1999). A Preliminary report on the Tehuacán, México Earthquake of June 15, 1999. *Seism. Res. Lett.*, **70**, 489-504.

Singh, S. K., M. Ordaz, L. Alcántara, N. Shapiro, V. Kostoglodov, J. F. Pacheco, S. Alcocer, C. Gutierrez, R. Quaas, T. Mikumo and E. Ovando (2000). The Oaxaca earthquake of 30 September 1999 (Mw=7.5): A Normal faulting event in the subducted Cocos Plate. *Seism. Res. Lett.*, **71**, 67-78.

Somerville, P. G., N. F. Smith, R. W. Graves, A. Abrahamson (1997) Modification of empirical ground motion attenuation relations to include the amplitude and duration effects of rupture directivity. *Seism. Res. Lett.*, **68**, 199-222.

Suter, M., O. Quintero and C. A. Johnson (1992). Active faults and state of stress in the central part of the Trans Mexican Volcanic Belt. 1- The Venta Bravo Fault. *J. Geophys. Res.* **97**, 11983-11993.

Trifunac, M. D., and A. G. Brady (1976). Correlation of peak acceleration, velocity and displacement with earthquake magnitude, distance and site conditions. *Earthquake Eng. Struct. Dynamics*, **4**, 455-471.

Trifunac, M. D., and D. E. Hudson (1971) Analysis of the Pacomia Dam accelerogram San Fernando California earthquake of 1971. *Bull. Seism. Soc. Am.*, **61**, 1393-1411.

Urbina, F., and H. Camacho (1913). La zona magasísmica de Acambay-Tixmadejé Estado de México, conmovida el 19 de Noviembre de 1912. *Bol. Inst. Geol. Mex*, **32**, 125.

Vazquez, E. and R. Jaimes (1989). Geologia de la Cuenca de México. *Geofis. Intr.* **28**, 2, 133-183.

Yamamoto, J. and R. Mota (1988). La secuencia de temblores del Valle de Toluca, México, de agosto 1980. *Geofis. Intl.* , **27**, 279-298.

Yamamoto, J. and R. Mota (1991). Reporte del monitoreo sísmico realizado en la región de Maravatío-Acambay durante el período de marzo de 1989 y agosto-septiembre de 1990. Serie Investigación No 137. Instituto de Geofísica, UNAM.

Yamamoto, J., L. Quintanar, R. B. Herrmann and C. Fuentes (1997). Lateral Variations of Lg Coda Q in Southern México. *Pure appl. geopys.*, **148**, 575-599.

Ziagos, J. P., D. D. Blackwell and F. Mooser (1985). Heat Flow in Southern México and the Therm Effects of Subduction. *J. Geophys. Res.*, **90**, 5410-5420.

Zuñiga, R., G. Suarez, M. Ordaz and V. García-Acosta (1998). Seismic Hazard in Latin America and the Caribbean. *Chapter 2 México*, Instituto Panamericano de Geografia e Historia. Centro Internacional para la Investigacion y el desarrollo. Final Report. Proy. 89-0190.

Vita Auctoris

Roberto Ortega was born in México City on August 5, 1966. He studied geophysical engineering at the "Universidad Nacional Autonoma de México, UNAM" where he graduated on May 1991. He received a master's degree in Computer Sciences at the "Instituto Tecnologico de Monterrey, ITESM" in 1993. He expected that a master's in computer sciences would give him the opportunity to move to fields far from geophysics, but after trying his luck as a computer programmer and system administrator he finally realized that seismology was much more fun. He decided to enroll in the Doctor of Philosophy program in Geophysics at St. Louis University in the fall of 1996.

When he is not behind a computer, Ortega usually can be found playing his harp. He started playing this unusual instrument at about 8 years old. Over the years he has played in many different places. He was scheduled to perform one of his last concerts a few hours after his oral defense as a Geophysics Engineer. The day of his graduation in geophysics he closed the first Harp Students Festival playing Debussy's First Arabesque. That was the last time he performed in public.

Besides his scientific and artistic interests, Ortega likes to dance to Latin music, bake all type of breads and pastries, and swim with the conditioning swimming team. He has learned many lessons in life but he learned the most important lesson from his parents the day he said goodbye and left his country for the United States. His father was recovering from major eye surgery so his mother became his eyes, patiently guiding him as

they turned to go home. This vision of trust and love has remained with Ortega as his greatest lesson in life.